Stress distribution under crawler crane timber mats

by

Rémi Avoine

A thesis submitted in partial fulfillment of the requirements for the degree of

Master of Science

In

Structural Engineering

Department of Civil and Environmental Engineering

University of Alberta

Abstract

In the construction industry, it is common practice to use timber mats beneath crawler cranes to redistribute heavy loads over large surfaces and allow the stresses on the soil to fall within allowable design limits. The distribution of stresses beneath the mats is generally assumed to be uniform, which implies that the crawler and mats are regarded rigid. This can lead to non-conservative designs for the soil. A 3D elastic finite element model was developed in Abaqus in order to question that assumption. Ten different crawlers were tested on four distinct soils: Sand Fill, Native Sand, Clay Till and Sand & Gravel. In particular, a specific model of crawler, constructed by Liebherr, and used by our industrial partner PCL, was examined. It was found that considering the crawler as a rigid body can lead to significant underestimated stresses, with a relative error from 10% to 50% depending on the crawler's size and soil type. When stress distributions obtained with Abaqus were compared with the stress distributions calculated by our industrial partner, it was found that they underestimated the stresses by about 37%. It was also determined that the typical assumption made in beam theory that an I-beam's rigidity is the only parameter to play a role in loads' redistribution, was acceptable if its dimensions were comprised within a finite range.

Acknowledgements

Table des matières

List of tables

Table of figures

1. Introduction

1.1. Point of this thesis

1.1.1. Contextual setting

It is common industry practice to use timber mats under mobile crawler cranes to redistribute heavy loads over larger surfaces to ensure that stresses fall within allowable design limits. The design of the mats generally assumes uniform distributed stresses beneath the mats (Duerr, 2012), which can lead to overly or non-conservative designs depending on the value calculated in offices by engineers.

The accuracy of the calculations made by the manufacturers are of prime importance as mobile cranes consist of very large devices that are meant to lift and carry around significant loads. This study focuses on a specific type of mobile crane manufactured by Liebherr: Liebherr LR 1750 (Fig. 1-1). Based on the documentation provided by the manufacturer, at maximum service load, each crawler that supports the crane can carry up to 500 t, which is equivalent to more than a million pound or 3 empty Boeing 747 ("Boeing 747", 2018). One or two layers of timber mats wedged between the crawlers and the soil are meant to spread the loads and reduce the stresses experienced by the soils. Typically, the installations of heavy materials on soils are always preceded by geotechnical studies. The analysis of soil samples collected *in situ* are supposed to accurately measure the quality of soils and in particular their bearing capacities, provided the uniformity of a soil over large areas. In practice, soils are most often heterogeneous, thus sampling can lead to non-conservative predictions of soils' quality. In some cases, this can lead to soils mechanical ruptures associated with ground collapses (Fig. 1-2).

Fig. 1-1: Liebherr LR-1750 (W-equipment, 2018)

Fig. 1-2: Soil collapses under crane load

1.1.2. Objective of the thesis

In that extent, accurately predicting the stress distribution generated by mobile cranes becomes critical to avoid non desirable economical and human catastrophes. Finite Element Analysis was performed in order to predict the actual stress distribution beneath one or several layers of timber mats. The newly acquired knowledge of these stress distributions will be used to develop a spreadsheet that will, eventually, be used by PCL in their daily routine in lieu of the current methods which are too conservative and costly.

1.1.3. Plan of the thesis

The thesis is composed of five chapters. The first chapter is made of the introduction.

The second chapter consists of a brief, condensed, illustrated and clear literature review which will familiarize the reader with the problematics of stress distributions in soils and the use of timber mats in coupling with crawler cranes.

The third chapter describes the development and use of a finite element model in the investigation of the stress distributions beneath the timber mat. It consists of the bulk of the work that was done in this thesis. It outlines the results that were obtained through simulations on Abaqus.

The fourth chapter compares numerical results derived in Chapter 2 with analytical stress distributions acquired via different assumptions on the system. In particular, the assumptions that are broadly made in the construction industry will be challenged.

The fifth chapter retraces my work during my internship at PCL. It provides a new method which outputs essential physical quantities that are sought for by engineers in offices before setting up mats and cranes on the field.

2. Literature review

2.1. Immediate stress distributions in soils

Stresses in soils greatly depend on their nature: sandy loam, loose sand, dense sand, gravel, silt, granular, cohesive, etc… This section will cover the stress distributions observed experimentally in a variety of soils. It does not intend to be comprehensive, as the studies on the topic are limited and the diversity of soils is important.

Most experimental studies show that stresses in soils tend to be parabolic. These experiments typically use strain gauges at different depths and use experimental curves to compute the according stresses. Abramov et al. (1968) measured the stresses exerted by a circular plate on a homogeneous sandy soil and a heterogeneous system of stone layers and sandy loam. They found that both systems showed similar stress behaviors (Fig. 2-1 and Fig. 2-2**Fig. 2-2**). The load is applied on a rigid plate with a hydraulic jack. Both figures only show one side of the stress distributions, for symmetry reasons.
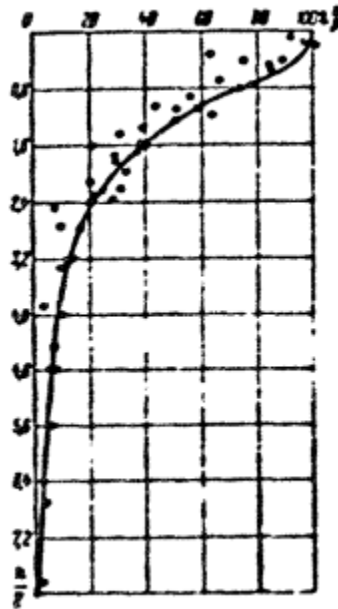
Fig. 2-1: Stress distribution in homogeneous soil halfspace:1) theoretical curve (plain line), 2) experimental results (points) (x-axis: stress; y-axis:depth)

Similar parabolic patterns were obtained for dry compact sand using a finite element method by J.V. Perumpral et al. (1971) on Fig. 2-3 and Fig. 2-4. These stress curves are the result of a circular contact (2D analysis) between the load source (a tractor wheel) and the soil, and are also symmetric with respect to the vertical axis of the circular contact's center.
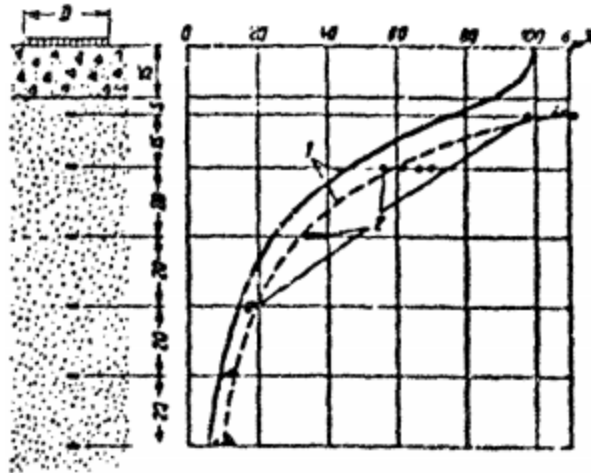
Fig. 2-2: 1) theoretical stress distribution for homogeneous soil (plain line), 2) theoretical stress distribution for sandy loam under a layer of crushed limestone, 3) experimental results (points)
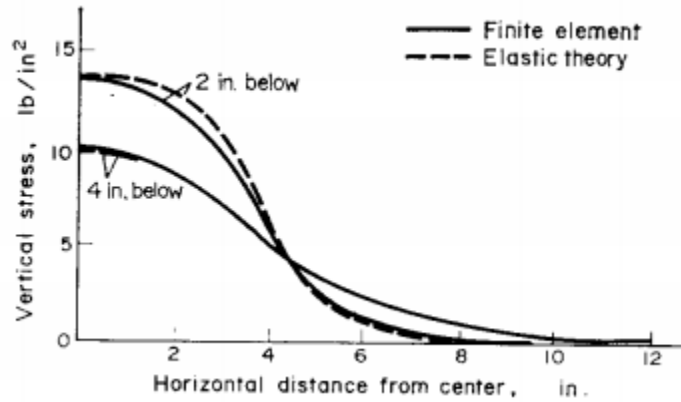
Fig. 2-3: Vertical stress distribution on horizontal planes below the surface
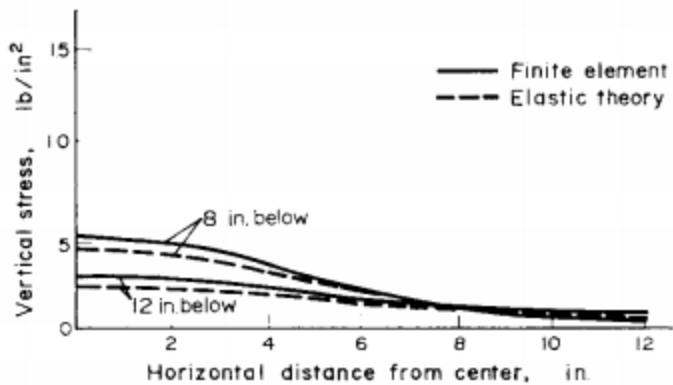
Fig. 2-4: Vertical stress distribution on horizontal planes below the surface

These parabolic stress distributions are recurrent amongst different types of soils. Stress distributions on silt loam were measured under lugged tires by K. Hammel (1994). Stress data were collected with cylindrical pressure cells used at different depths; they are shown on Fig. 2-5.
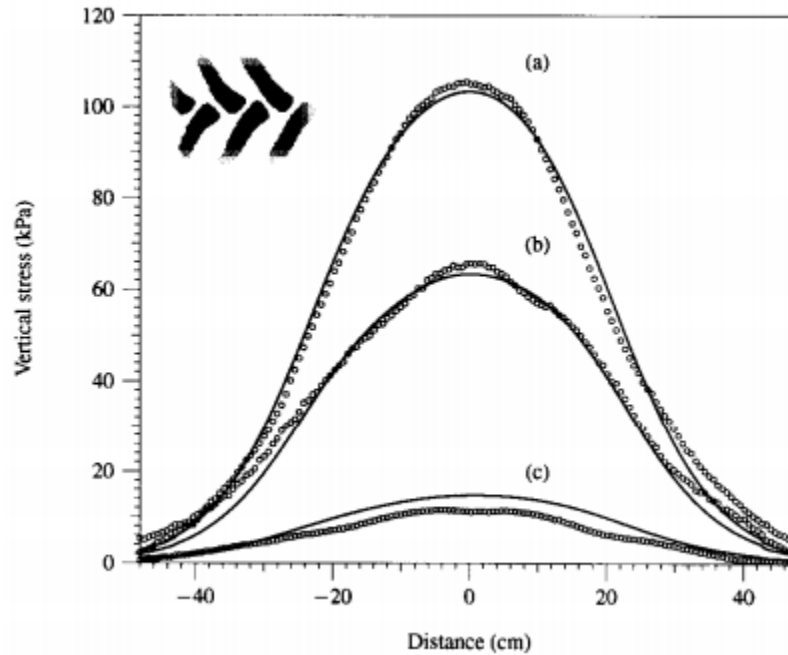
Fig. 2-5: Measured (solid lines) and calculated (symbols) vertical stress in the track center (a) at a distance of 15 cm (b) and 30 cm (c). The contour plot in the upper left corner indicates the surface load distribution. The black color refers to a weighting factor of 1, which decreased linearly towards the boundary of the contact area. The weighting factor at the boundary was 0.2.

2.2. Stress distributions in soils with an intermediate

If a direct contact between load areas and soils tend to lead to parabolic stress distributions in the soil, the use of an intermediate like a beam seems to depend on the latter's physical properties. Cui and Zhou (2009) used a finite element method to investigate the stress distribution underneath a circular beam subjected to a uniform stress all over its surface, and tested the case of a flexible beam (flexural rigidity close to zero) and a rigid beam (high flexural rigidity), with two different soils: a clay soil and a sandy soil. The use of a flexible beam means that vertical stresses were virtually applied on the soil's surface; the numerical results show that stress distributions with such a beam are uniform for both soil types (the stress is uniform). The use of a rigid beam,

however, lead to non-uniform-stress distributions that greatly depend on the soil type, as shown in Fig. 2-6.

(a) Clay soil
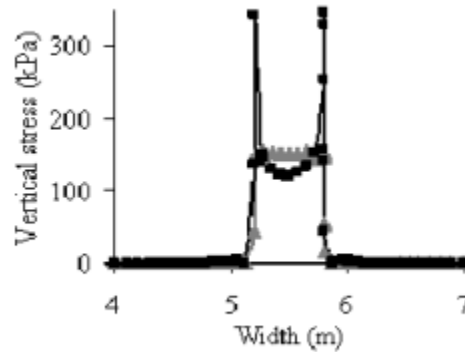
(b) Sandy soil
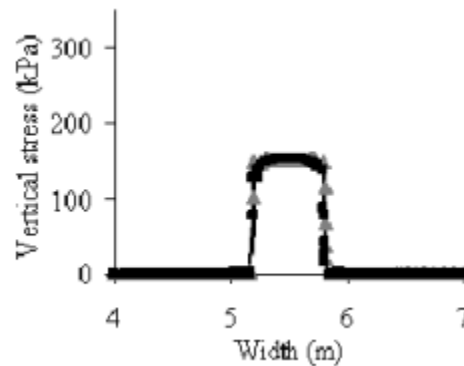
Fig. 2-6: Calculated vertical stress distributions on the soils surface with a very soft circular plate (i.e. EI = 0.01 kN.m^2) (grey triangles) or a very rigid circular plate (i.e. EI = 8500 kN.m^2) (black squares) on (a) a clay soil, (b) a sandy soil

Fig. 2-6 highlights that stress distributions in soils depend on the relative stiffness of the beam and the soils. This characteristic will be greatly discussed in this thesis.

The effect of a rigid plate between the load and the soil was also investigated by Corey and Han (2011). Their study is interesting, for it builds the grounds of a part of the work that has been done in this thesis. They investigated the stress distribution at the surface of two different soils, made of dense and loose sands, in reaction to a point load applied at the center of a concrete footing considered rigid (Fig. 2-7). The stress distributions obtained are shown on Fig. 2-8 and Fig. 2-9.

6

Fig. 2-8 and Fig. 2-9 illustrate that the shape of the stress distributions depends on the magnitude of the point load and the rigidity of soils. The dense soil exhibits the same plateau type response to every load; the magnitude of the plateau increases with the load, but its extent within the footing's width is a constant. The loose soil, however, shows stress distributions which present a plateau for small loads, and become parabolic as the load increases. In other words, the rigid soil seems to redistribute the load more efficiently than the soft soil, but most importantly, the use of an intermediate solid between the load and the soils tend to harmonize the stress distributions in the soils, at least to some extent.
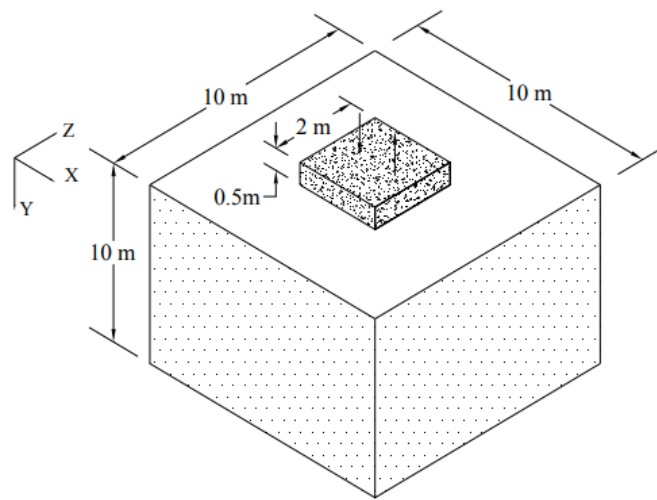
Fig. 2-7: Model description
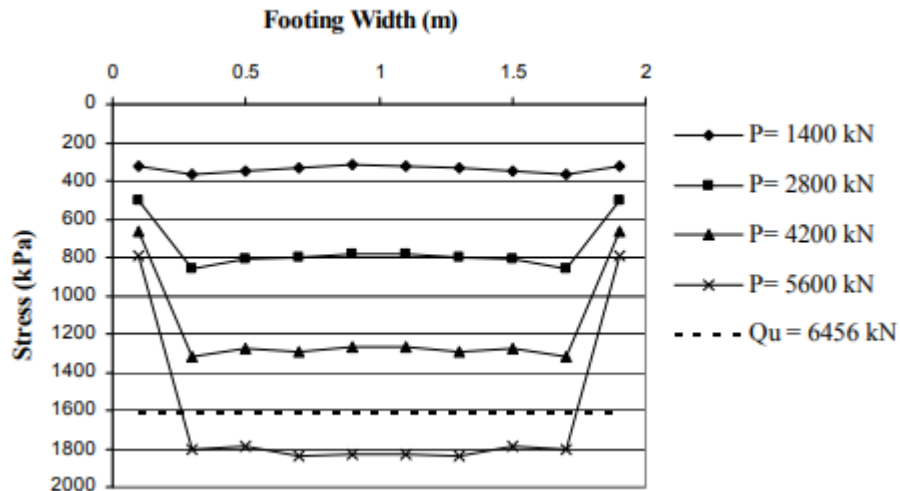
Fig. 2-8: Soil stress from concentric load P on dense sand
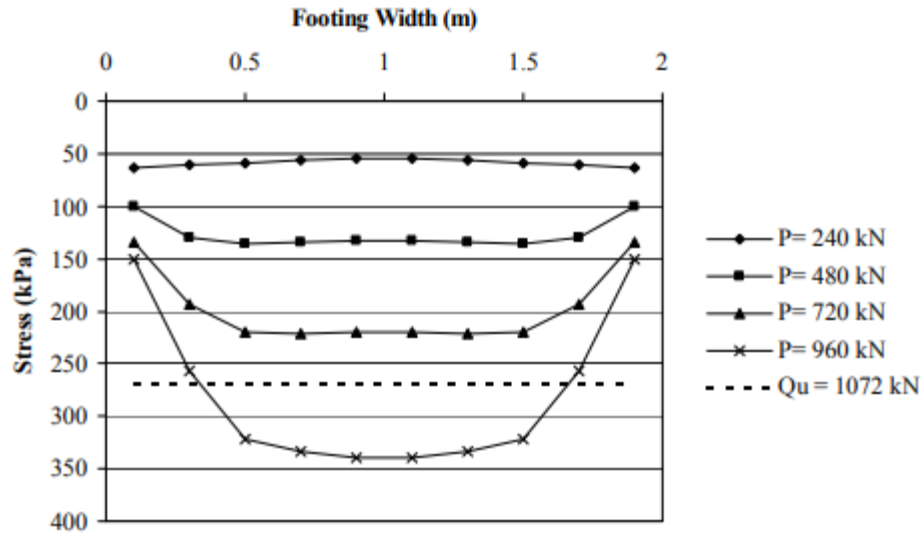
Fig. 2-9: Soil stress from concentric load P on loose sand

The overview of all the studies that precede makes one understand the incentive behind the use of mats under crawler cranes. These engines can have a track pressure up to 500 t or 5 MPa. A direct contact between large crawler cranes and soils would lead to an extremum in the stress distribution parabolas in the grounds that would exceed most soils' bearing capacities. Timber mats are then used as an intermediate to spread loads on wider surfaces and allow the stresses to fall within allowable design limits.

2.3. Use of crawler crane mats in the industry

The setting up of timber mats is made such that they can be considered solidary with one another. Indeed, the presence of mats on the side of each mat (except those on the outermost) prevents them from rotating about two main axes. The rotation is also kept small by the weight of the crane on the mats. As a result, the differential settlement between two neighboring mats can be considered negligible. It is customary to model one mat by a shallow foundation of depth equal to zero.

Classically in the industry, stresses beneath the mats are assumed to be uniform and equally distributed (Duerr, 2012). This assumption, however, depends on many factors such as the mats thickness (Liu, 2005), the relative stiffness of mats and soils (Cui and Zhou, 2009), the intensity

of loads (Corey and Han, 2011). Predicting the spreading of the stresses in the mat is of prime importance in order to accurately predict the stress distribution on the soil.

Shapiro (1999) derived an equation from computer simulations to estimate the width of the equivalent footing beneath the mat:

$$B' = B + 2d(\frac{E_m}{E_s})^{0.29}$$

Where E_m = Young's modulus of Mat

E_s = Young's modulus of Soil

d = mat thickness

and B and B' are the crawler width and the equivalent footing, illustrated on Fig. 2-10.
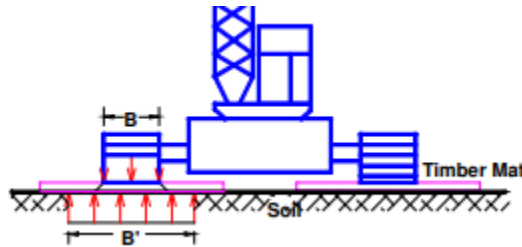
Fig. 2-10: Crane track pressure distribution through timber mats (modified from Shapiro 1999)

Meng et al. (2017) and Duong and al. (2018) investigated the stress distribution under rough terrain crane's outrigger supports and crawler crane mats. In the first study, Meng et al. tested three boom's positions and three working radii. Each outrigger support was set on a circular plywood mat in order to spread the loads over larger areas. They measured the ground bearing pressure (GBP) with two pressure cells buried in the soil at 4" and 10" depths at a specific position, and compared the data obtained with the GBP beneath the plywood mats derived from two analytical methods: the 2:1 approximation and the Boussinesq equation, which respectively assume a concentrated load and a uniformly distributed load from the outrigger to the mats; and two finite element analysis, assuming the same loading distribution as the analytical methods.

They plotted three slews of data, for the three radii and the least favorable boom's position. The three plots being very similar in shape, only one will be displayed here (Fig. 2-11). Fig. 2-11 shows that the methods assuming a concentrated load and uniformly distribution loads show similar trends pairwise; therefore, the vertical stress distributions do depend on the loading

9

distribution over the ground surface. It also demonstrates that the values of GBP measured from tests are roughly comprised between the two FEA sets of data. It implies that, in reality, the loading distribution between the outriggers and the mat is uniform, as opposed to concentrated, but that the area considered is less than the contact area.

Duong and al. (2018) worked on the same system as the present study, but in two dimensions, i.e. they tested the same four soils with one or two layers of timber mats. They showed, in a 2D finite element analysis, that using a uniformly distributed pressure assumption for granular
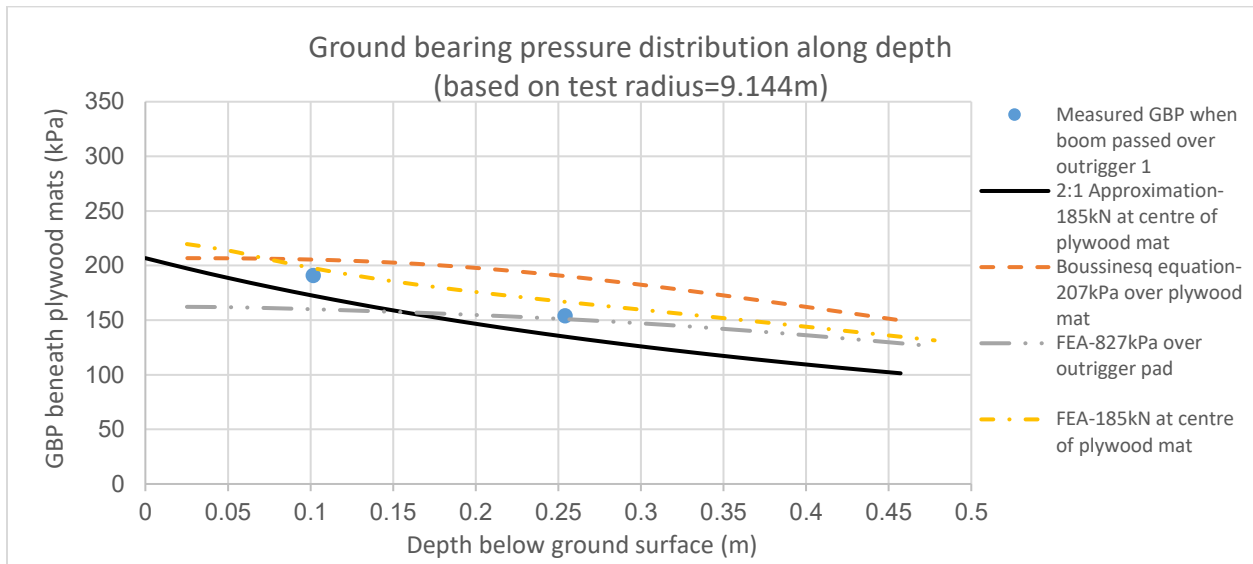
Fig. 2-11: Comparison of GBP distribution (boom's angle $\alpha = 135°$) along the depth obtained from various methods corresponding to test radius of 9.144 m

soils, whose vertical stress profile underneath the mat are comparable to parabolas, may be conservative for the design of the mat but may be non-conservative for the system as a whole.

Lastly, the team that issued Meng et al. (2017) paper collected experimental stress data in a soil, with the crawler crane introduced on Fig. 1-1, in partnership with PCL. These data are the reason why the rigid body assumption of the crane was questioned in the first place (Fig. 1-14).
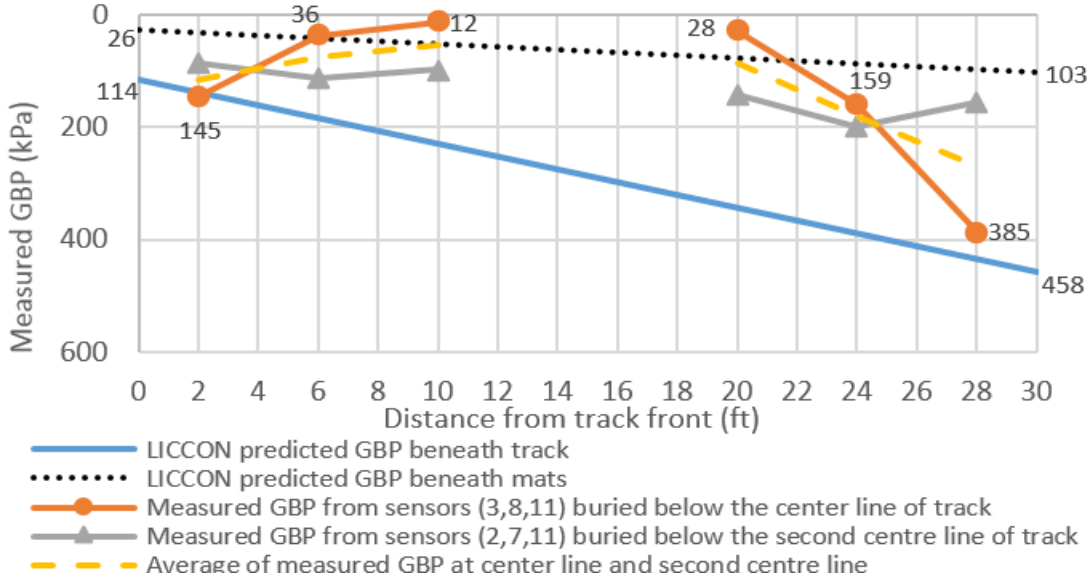
Fig. 2-12: Stress distribution when crane's boom passed over front corner

The crane software provided by Liebherr, called Liccon, predicts either triangular or trapezoidal diagram under the crane's tracks based on the rigid body assumption. Fig. 1-14 shows that the experimental data measured at the tracks' corners, however, are higher than those predicted values. This contradicts current design methods which treat the crawler frame and carbody as rigid objects. The experimental data also support the statement that the crane load is largely distributed to four corners, i.e. each crawler's two ends.

The present study aims at investigating that contradiction between the theory and the experimental data. A finite element model was developed for this purpose, in Abaqus 6.14 (2014), to investigate the stress distribution under crawler crane timber mats.

3. Development of a Finite Element Model with ABAQUS

3.1. Objectives

Insofar as this thesis does not contain any test experiment, the Finite Element Analysis model shapes the bulk of it. This chapter was motivated by three objectives: investigating the effects of crawler's stiffness on the stress distribution beneath the timber mats, in the directions parallel and perpendicular to the crawler's length; investigating the effects of soil type on the same stress distributions, along the same directions; and finally investigating the effects of an I-beam's dimensions on the stress distribution beneath timber mats.

1. Model description

The model was developed in Abaqus 6.14 (2014). It is composed of three parts: an I-beam primarily modeled according to Liebherr crawler's dimensions (Fig. 3-1), H=1846mm, B=1500mm, h=142mm, b=355mm, L=11900mm. In order to enhance the efficiency of simulations, the crawler was also modeled as a shell with a height of 2130 mm and similar width and length; the crane mats (Fig. 3-2), 304.8 mm thick, 1219.2 mm wide, 6096 mm long, and the soil (Fig. 3-3), 10 m wide, 18 m long and 8 m deep.

A compromise to a reasonable soil's size was done in order to alleviate edge effects without radically increasing the computational time of the model. Fig. 3-4 and Fig. 3-5 show two soil's cuts along its width; the scales highlight that stresses remain at the bottom of the soil (Fig. 3-5), which
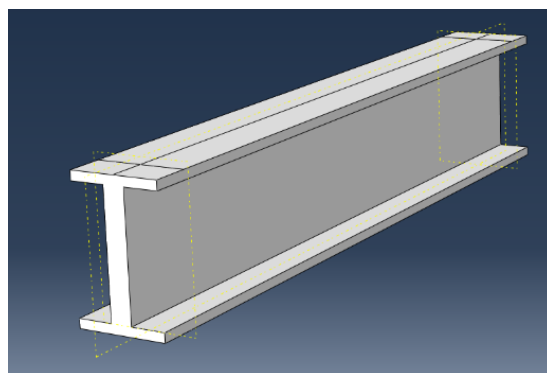
Fig. 3-1: I-beam according to Liebherr crawler's dimensions
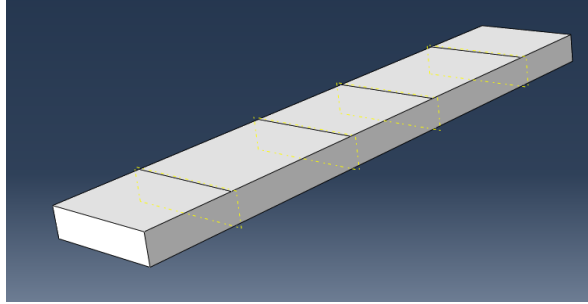
Fig. 3-2: Board of timber mat
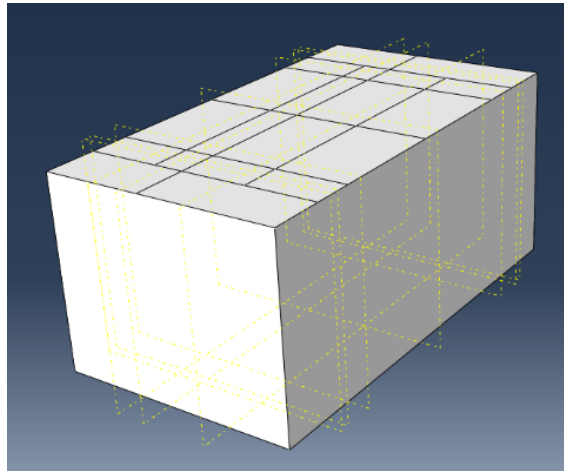
Fig. 3-3: Soil

are around 50 times less than the highest stresses experienced by the soil, about 4 m away horizontally from point loads. Table 3-1 to Table **3-3** outline the materials' properties used in the study.

The load case consists of two point loads going downwards, located 637 mm from the beam's ends, and at the middle of its width. Their magnitude of 2500 kN is based on the crane's service load (Liebherr documentation). Fig. 3-6 shows a 3D view of the system.
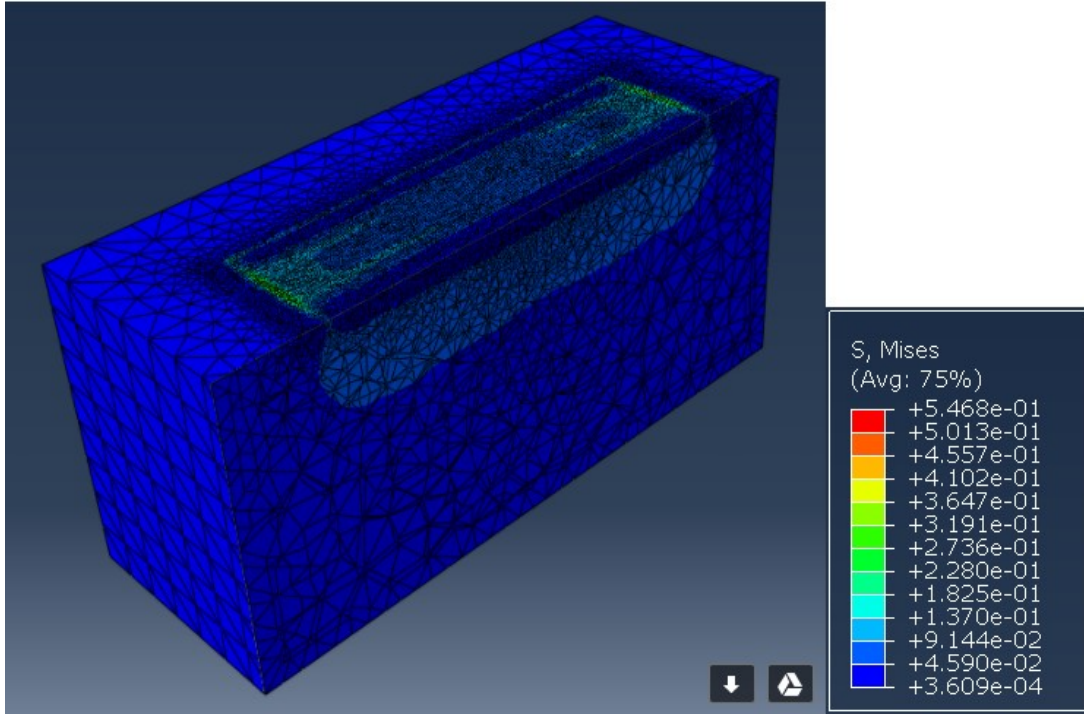
Fig. 3-4: Soil cut along its width, about a third from its base
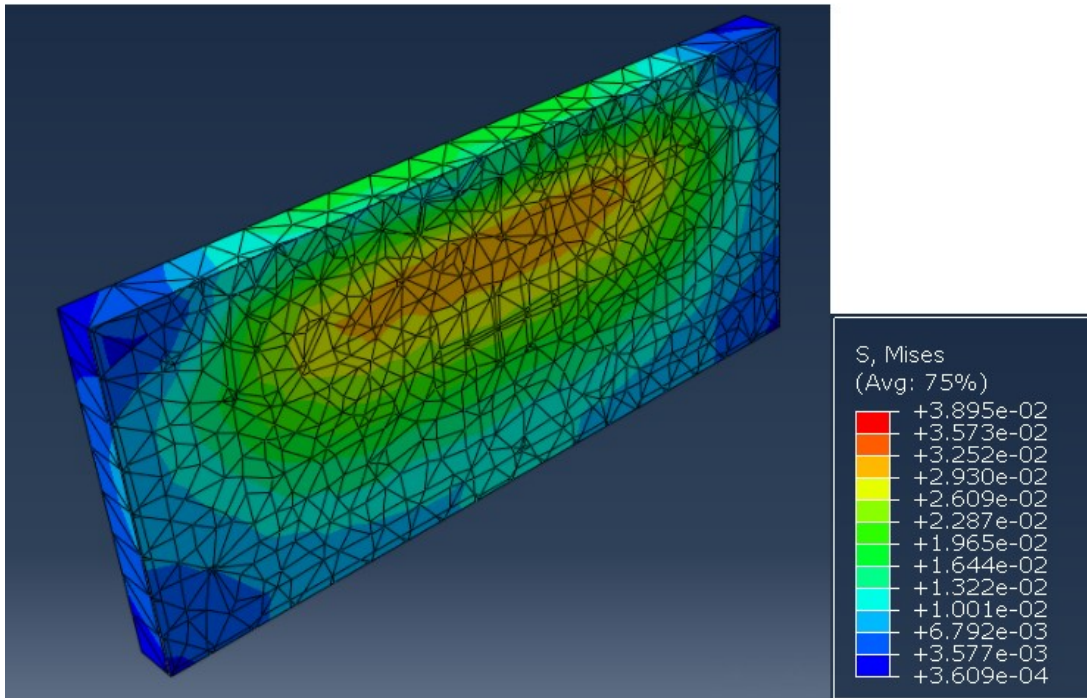
Fig. 3-5: Soil cut along its width, almost completely

Table 3-1: Model parameters – Crawler

			Crawler
Part	Modelling Space		3D
	Type		Deformable, Solid
	Geometry[1]		2.130 m H x 1.5 m W x 11.9 m (L) Web: 0.355 m; Flanges: 0.142 m
	Mesh Controls	Element Shape Technique	Hex Sweep
	Seed	Approx. Size	0.075 m
	Element Type	Family Geometric Order Other	Plain Strain Linear Reduced integration
Materials	Type		Isotropic Elastic
	Provided Parameters[1]		E = 200 000 MPa (Bestech, 2018); ν = 0.3
	Model Input		Elastic E = 200 000 MPa; ν = 0.3 Density 7800 kg/m^3
	Plastic Flow Rule		N/A
Sections	Category Type		Solid Homogenous
Interaction	Type		Surface-to-surface
	Definition		Crawler to Mat: Master - Bottom of crawler, Slave - Top of Mat
	Interaction		Tangential Behaviour: Friction Coefficient = 0.3 Normal Behaviour: Pressure-Overclosure "Hard" Contact
Boundary Conditions	Point load		Fixed sideways (U1=U2=0)

[1] Provided parameters taken from Liu (Liu, 2005) and the Wood Hand Book (Forestry Products Laboratory, 2010)

Table 3-2: Model parameters – Crane mat

			Crane mat
Part	Modelling Space		3D
	Type		Deformable, Solid
	Geometry[1]		0.3048 m (1 ft) H x 3.048 m (10 ft) W x 6.096 m (L)
	Mesh Controls	Element Shape Technique	Hex Structured
	Seed	Approx. Size	0.075 m
	Element Type	Family Geometric Order Other	Plain Strain Linear Reduced integration
Materials	Type		Transversely Isotropic Elastic
	Provided Parameters[1]		EL=11 GPa, ET=ER=647 MPa, νTL=νRL=0.04, νTR=νRT=0.38, GLR=GLT=779 MPa, GRT=76.8 MPa (Liu, 2005, pg.136)
	Model Input		<u>Elastic</u> E1=11 GPa, E2=E3=647 MPa, ν12=ν13=0.68 (by orthotropic relationship), ν23=0.38, G12=G13=779 MPa, G23=76.8 MPa <u>Density</u> 540 kg/m^3
	Plastic Flow Rule		N/A
Sections	Category Type		Solid Homogenous
Interaction	Type		Surface-to-surface
	Definition		Crawler to Mat: Master - Bottom of crawler, Slave - Top of Mat; Mat to Soil: Master - Bottom of Mat, Slave - Top of Soil
	Interaction		Tangential Behaviour: Friction Coefficient = 0.3 Normal Behaviour: Pressure-Overclosure "Hard" Contact
Boundary Conditions	Sides		Fixed sideways (U1=U2=0)
	Bottom		-

[1] Provided parameters taken from Liu (Liu, 2005) and the Wood Hand Book (Forestry Products Laboratory, 2010)

Table 3-3: Model parameters - Soil

		Soil			
Part	Modelling Space	3D			
	Type	Deformable, Solid			
	Geometry[1]	8 m H x 10 m W x 18 m L			
	Mesh Controls — Element Shape	Tet			
	Technique	Free			
	Seed — Approx. Size	0.075 m			
	Element Type — Family	Plain Strain			
	Geometric Order	Linear			
	Other	-			
Materials	Type	Elastic, Mohr Coulomb Plasticity			
	Provided Parameters[1]	Sand Fill (Fort McMurray) E=33 MPa, v=0.3, Friction angle=36°, cohesion c=0.01 kPa, γ= 17.3 kN/m³ (Liu, 2005, pg. 158)	Clay Till (Fort McMurray) E=120 MPa, v=0.49, Friction angle=0°, cohesion c=240 kPa, γ= 21 kN/m³ (Liu, 2005, pg. 158)	Native Sand (Fort McMurray) E=55 MPa, v=0.3, Friction angle=36°, cohesion c=0 kPa, γ= 18 kN/m³ (Liu, 2005, pg. 158)	Sand and Gravel Fill (Fort McMurray) E=150 MPa, v=0.15, Friction angle=48°, cohesion c=0 kPa, from other γ= 22.5 kN/m³ (Liu, 2005, pg. 158)
	Model Input	Elastic E=33 MPa, v=0.3 Density 1763.5 kg/m³ Mohr Coulomb Plasticity Friction Angle=36°, Cohesion = 0.1 kPa, Dilation Angle=6°, Abs Plastic Strain=0	Elastic E=120 MPa, v=0.49 Density 2140.7 kg/m³ Mohr Coulomb Plasticity Friction Angle=0°, Cohesion = 240 kPa, Dilation Angle=0°, Abs Plastic Strain=0	Elastic E=55 MPa, v=0.3 Density 1834.9 kg/m³ Mohr Coulomb Plasticity Friction Angle=36°, Cohesion = 0.1 kPa, Dilation Angle=6°, Abs Plastic Strain=0	Elastic E=150 MPa, v=0.15 Density 2293.6 kg/m³ Mohr Coulomb Plasticity Friction Angle=48°, Cohesion = 0.1 kPa, Dilation Angle=15°, Abs Plastic Strain=0
	Plastic Flow Rule	Non-Associated Flow Rule	Associated Flow Rule	Non-Associated Flow Rule	Non-Associated Flow Rule
Sections	Category	Solid			
	Type	Homogenous			
Interaction	Type	Surface-to-surface			
	Definition	Mat to Soil: Master - Bottom of Mat, Slave - Top of Soil			
	Interaction	Tangential Behaviour: Friction Coefficient = 0.3 Normal Behaviour: Pressure-Overclosure "Hard" Contact			
Boundary Conditions	Sides	Fixed (U1=U2=U3=0)			
	Bottom	Fixed (U1=U2=U3=0)			

[1] Provided parameters taken from Liu (Liu, 2005) and the Wood Hand Book (Forestry Products Laboratory, 2010)

Fig. 3-6: System {crawler + timber mats + soil}

The results of a total of forty-five models were compiled in this study, ten models with increasing shell thicknesses for each of the four soils, and five more models meant to investigate the effect of the I-beam's dimensions on stress distributions. The four soil types were taken from a previous crane mat study conducted at the University of Alberta by Liu (2005). They include Sand Fill, Native Sand, Clay Till and Sand & Gravel.

The crawler was modelled as an elastic material defined by a Young's modulus and a Poisson's ratio. The crane mat was modelled as a transversely isotropic material defined by a Young's modulus, a Poisson' ratio and a Shear modulus in each direction. The soils were modelled as elastic materials defined by Young's modulus and Poisson's ratio. While soils are usually modelled elasto-plastically, the large amount of models that had to be run did not allow the soils to be modelled plastically, as it would have impractically lengthened the time required for the simulations. As it will be discussed later in the study, however, this alternative did not affect the results significantly such that the stress values obtained are still valid.

3.2. Shape of the stress distribution beneath the timber mats and peak stresses

This section will present the typical distribution of stress beneath the timber mats and the associated peak stresses.

3.2.1. Contour plots on ABAQUS

Fig. 3-7 is a view of the whole system from above, showing successively the crawler, the layer of timber mats and the soil.
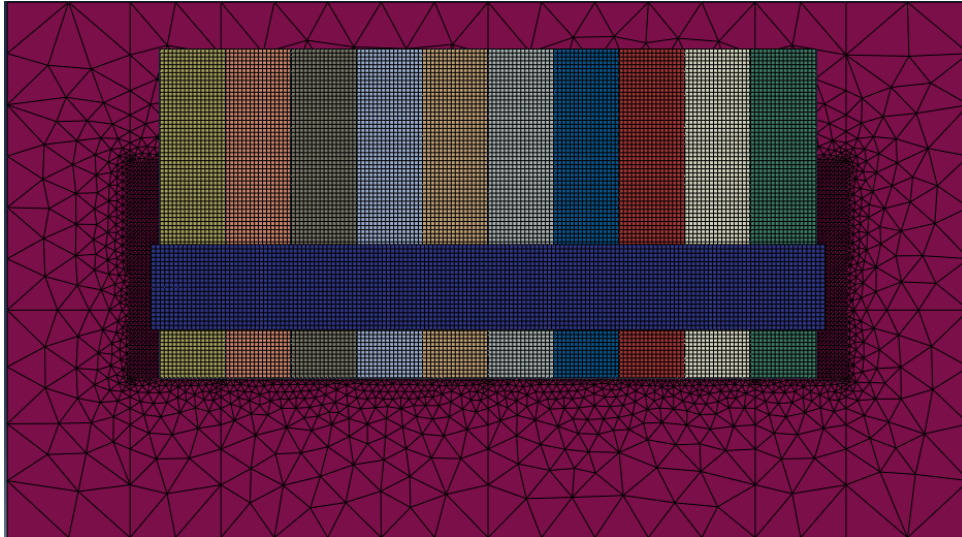
Fig. 3-7: System {crawler + timber mats + soil} from above

Once the crawler is removed, the normal stress contour plots can be observed on the mats on Fig. 3-8. Stress distributions beneath the mats can equally be observed when the latter are taken away (Fig. 3-9).
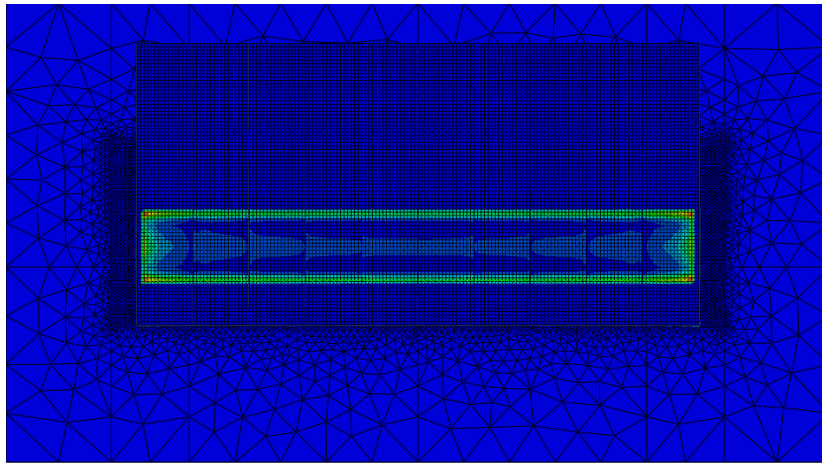
Fig. 3-8: Normal stress contour plot between crawler and timber mat
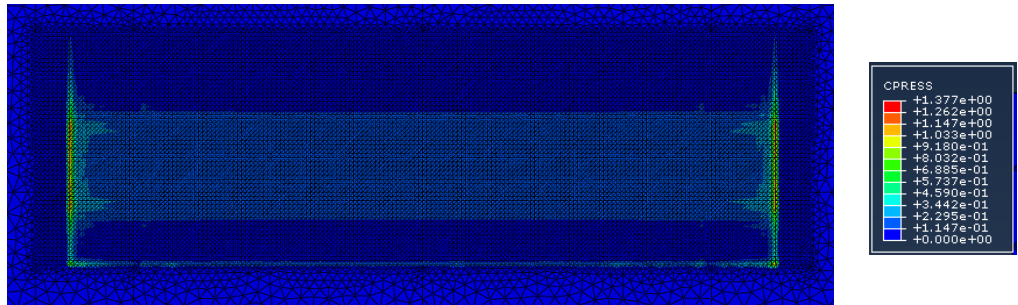
Fig. 3-9: Normal stress contour plot beneath timber mat

Fig. 3-8 shows the normal stress contour plot on the timber mat. High stress values are located beneath the crawler's edges. Similarly on Fig. 3-9, high stress values are located beneath the mats' edges on either side of the figure and at its bottom, underneath the mat's end. These high stress values beneath solids' ends were not expected; they were called "peak stresses" in the frame of this study. These peak stresses impeding a proper visulization of stress distributions, they were trimmed off in the section that follows.

3.2.1.1. Contour plots with peak stresses trimmed off

Fig. 3-8 and Fig. 3-9 displayed contour plots on and beneath the mat, highlighting the presence of peak stresses below the crawler's and the mat's ends. Fig. 3-10 and Fig. 3-11 show the same contour plots, but with carefully chosen scales which enable to appreciate the stress distributions between peak stresses.
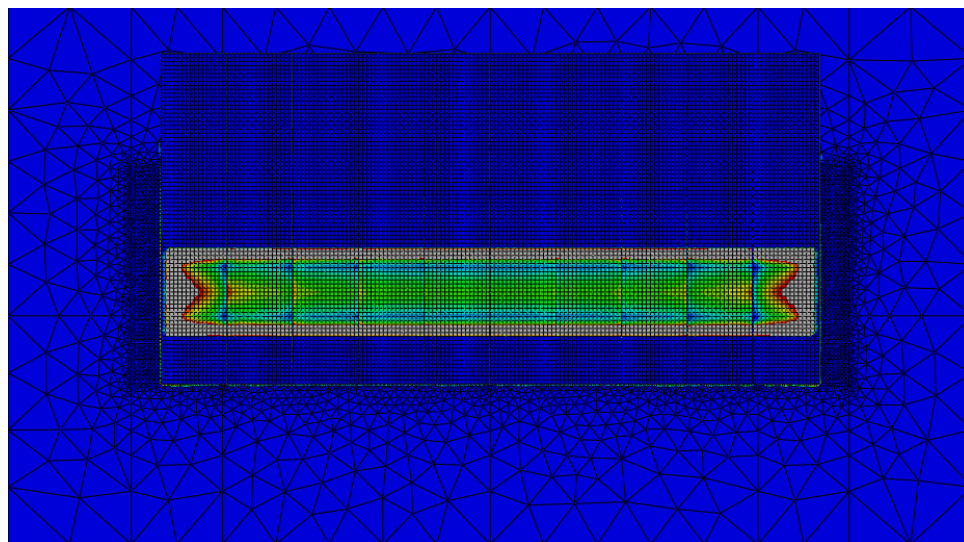
Fig. 3-10: Normal stress contour plot between crawler and timber mat after high values are skimmed off
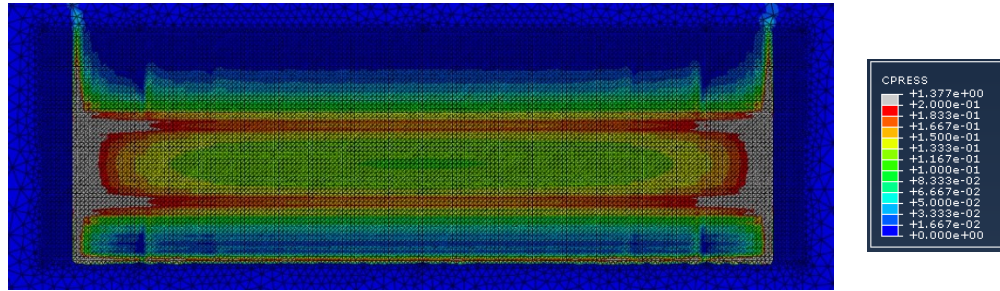
Fig. 3-11: Normal stress contour plot beneath timber mat after high values are trimmed off

The contour plots shown in Fig. 3-10 and Fig. 3-11 indicate that stress distributions are not uniform, be it between the mat and the crawler or beneath the layer of mat. The red color on Fig. 3-11 are high stress values, located in the area directly beneath the crawler. In the field, the high stress area colored in red and its inside correspond to the crawler's tracks pictured in Fig. 3-12.

In order to have a better visualization of the behaviors of the soil and peak stresses to the loads, stress data were collected from Abaqus and surface plots were coded on Matlab.

Fig. 3-12: Crawler crane track

3.2.2. Surface plots on Matlab

Fig. 3-13 depicts surface plots obtained with soil's stress data using Matlab. The areas in yellow correspond to the peak stresses mentioned earlier; the dominance of peak stresses over the stress distribution in the inner area is graphically blatant. By zooming in the area in the center, which is the area beneath the crawler, Fig. 3-14 is obtained.
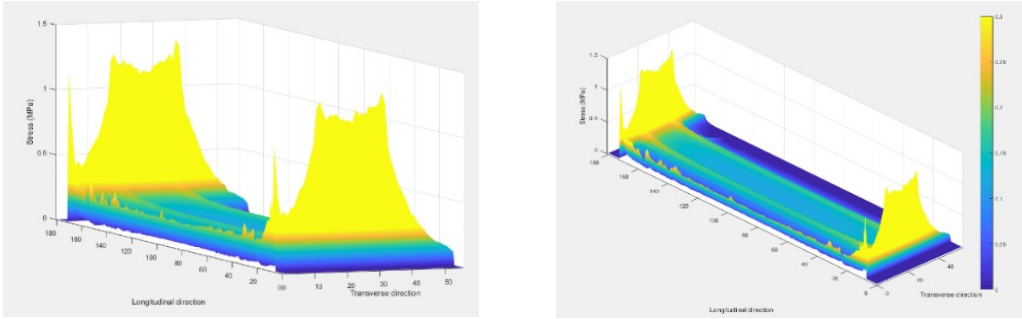
Fig. 3-13: Stress distribution surface plot beneath the timber mats
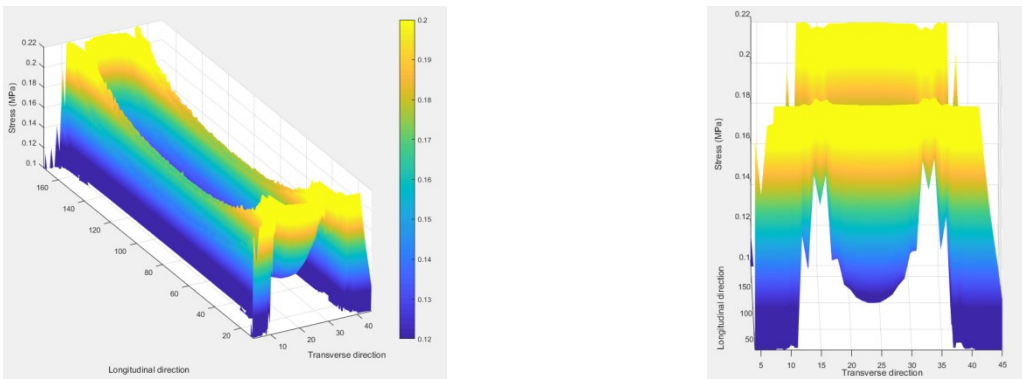
Fig. 3-14: Stress distribution surface plot beneath the timber mats after skimming off of peak stresses

The shape on the left hand plot in Fig. 3-14 is typical and characteristic of all the stress distributions that will be shown and studied in this thesis. The contour of the long bowled shape is the area underneath the crawler's ends. It surrounds a stretched hollow groove where stresses are much lower than the contour and is surrounded towards the edges by slopes where stresses fade out as we get further off the bowl. As it will be shown in *3.3. Analysis of stress distributions beneath the timber mats*, the depth and flatness of the bottom of the bowl is function of the crawler's stiffness and soil type.

At first sight, the peak stresses beneath the mat's ends could be thought to be the result of an anomaly generated by Abaqus. The next part is an in-depth study of these peak stresses and of their behavior.

3.2.3. Analysis of peak stresses beneath the timber mats

3.2.3.1. Adapted model description

The specific study of the stresses beneath the mat's ends needed the model to be adapted to make it more relevant. Fig. 3-15 is a snapshot of that model.
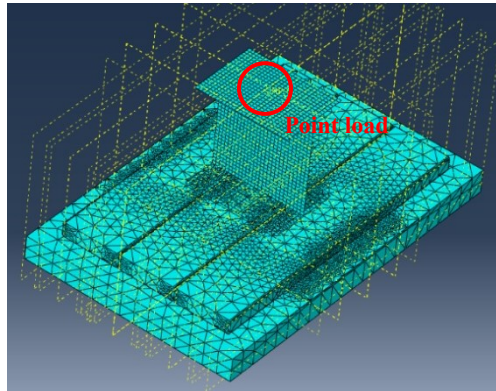
Fig. 3-15: Model adapted to the analysis
of peak stresses

The load case consists of a single point load directed downwards at the center of the small crawler shell. Its magnitude was taken high enough to generate significant stresses on the soil beneath the layer comprised of three mats.

The crawler was modeled as a shell rigid body.

These mats are identical to the mats defined before with the exception that their edges are fileted in order to simulate the layer of timber mat's ends of the previous section (Fig. 3-16**).** The objective here was to study the stress distributions around the mats' edges; their mesh was therefore taken coarse far from the edges, fine around them with 30 mm tet elements. This is the smallest element size that could be tested; Abaqus would only run the model with a mesh of that size or coarser, for computing power reasons. Besides, three boards of timber mats were estimated to be sufficient to study the edge effects. Using only one would have alleviated the flexibility in the results' interpretation.

The peak stresses' occurrence was considered to be independent on the soil's depth; it was shortened to 500 mm thick. The mesh size on the soil was taken identical to the mats'.
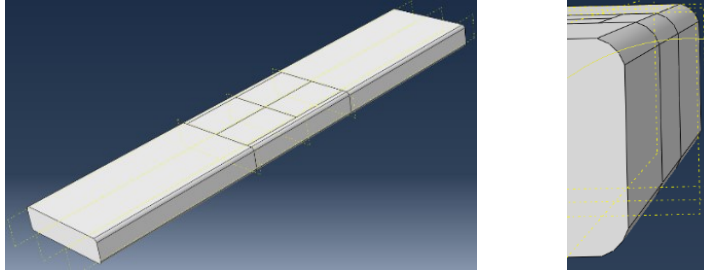
Fig. 3-16: Timber mat with fileted edges

3.2.3.2. Results

3.2.3.2.1. Localization of peak stresses
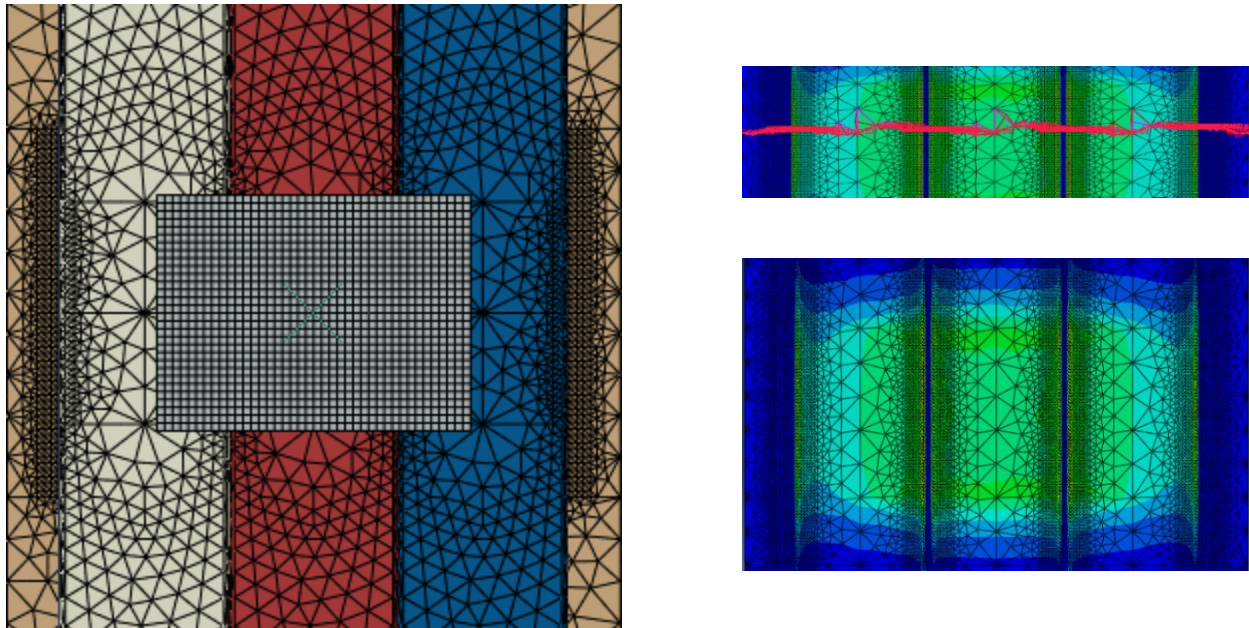
Fig. 3-17: Left: system viewed from above; Right: normal stress contour plot beneath the timber mat, path in red

Fig. 3-17 shows the normal stress contour plot beneath the mats. Three distinct areas are observed; each one corresponds to the stresses transmitted by the timber mat that lays above. Zero stress strips separate these areas, owing to the filets on the mats which transmit no loads. The stress distribution collected along the path drawn in red in Fig. 3-17 is displayed in Fig. 3-18.
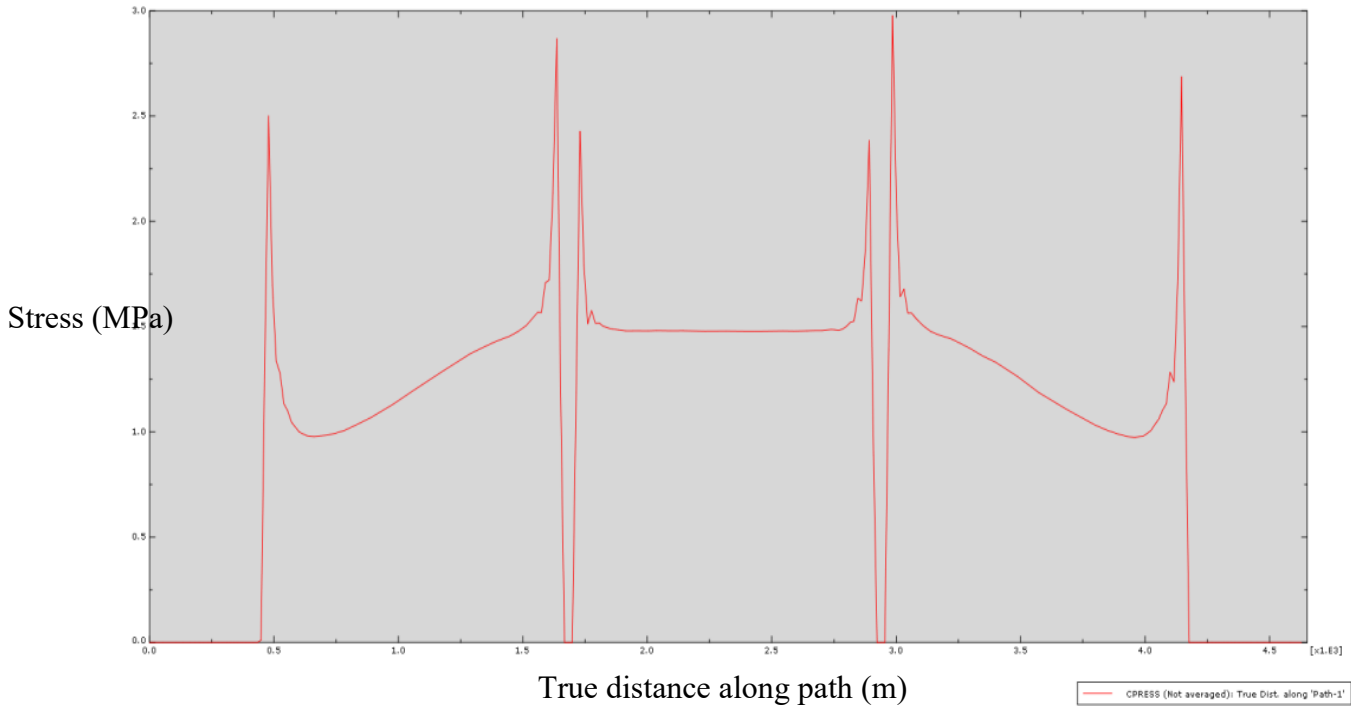
Fig. 3-18: Stress distribution along a path transverse to the mats

Fig. 3-18 depicts three regions coinciding the three areas of Fig. 3-17. The two regions on the left and right are symmetric and show an increase and decrease of stresses; the region in the center displays a plateau level of stress which asserts the rigid body property of the crawler: The plot also shows that the peak stresses, which are located at the points of discontinuity between the mats at either side of the zero strips, subsist even with a very fine mesh. This result confirms what was observed on the stress distribution obtained on the original model: peak stresses appear on areas where solids that lay above end.'

In order to have a better idea as to how these peak stresses act, the same analysis was conducted on two random paths for three mesh sizes: 30 mm, 50 mm and 75 mm elements (Fig. 3-19 and Fig. 3-21); normal stresses were then plotted on Fig. 3-20 and Fig. 3-22.

Two conclusions can be drawn from Fig. 3-20 and Fig. 3-22. The locations of peak stresses do not depend on the mesh's accuracy, and they always occur at the points of discontinuity between mats. Also, the finer the mesh, the higher the peak stresses, which goes in the sense of the actual existence of these high localized stress values. It can even be conjectured, without the possibility to verify it, that the peak values would diverge as the mesh would get more refined.
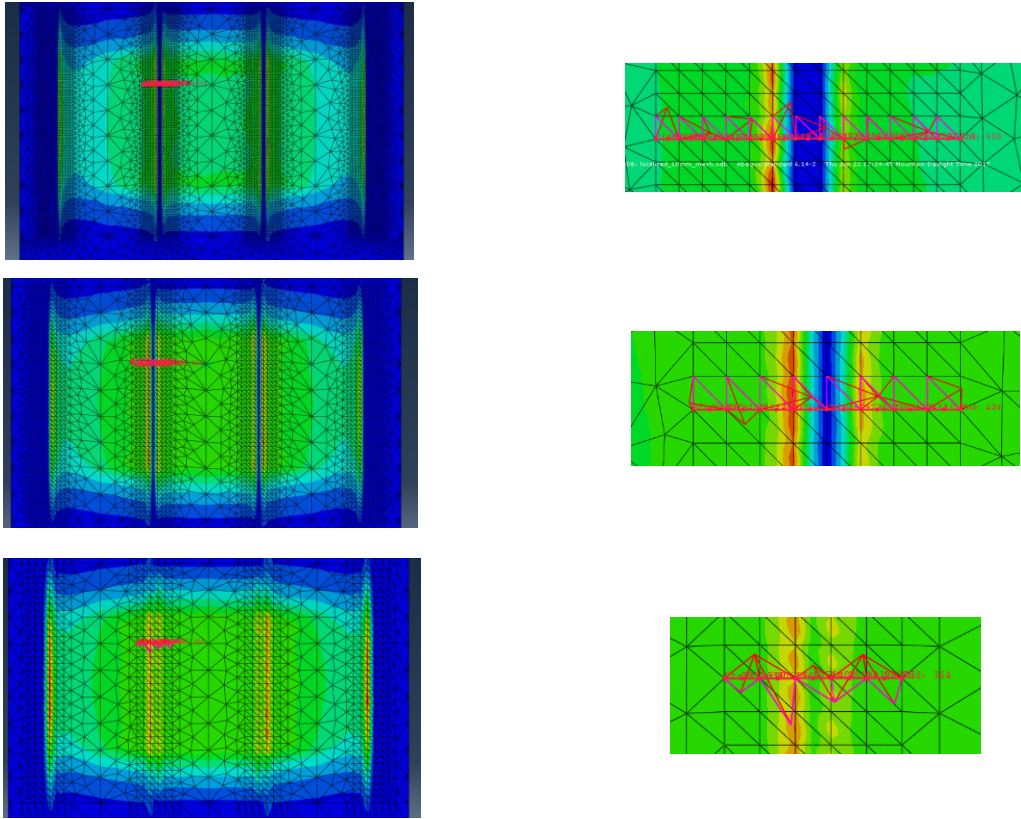
Fig. 3-19: Up to down: 30mm, 50mm and 75mm meshes. Left to right: contour plot viewed from above and zoom on the paths
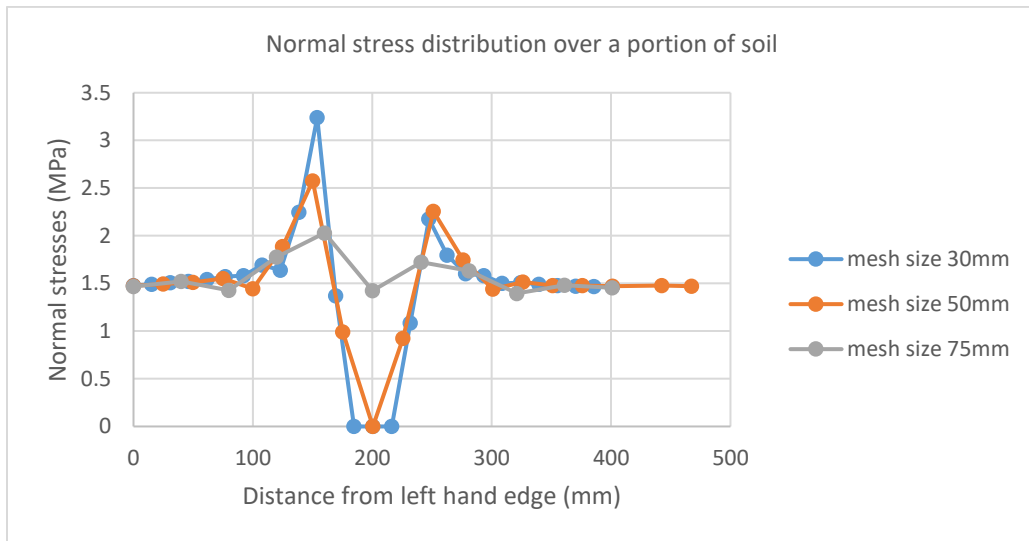
Fig. 3-20: Stress distributions along the paths
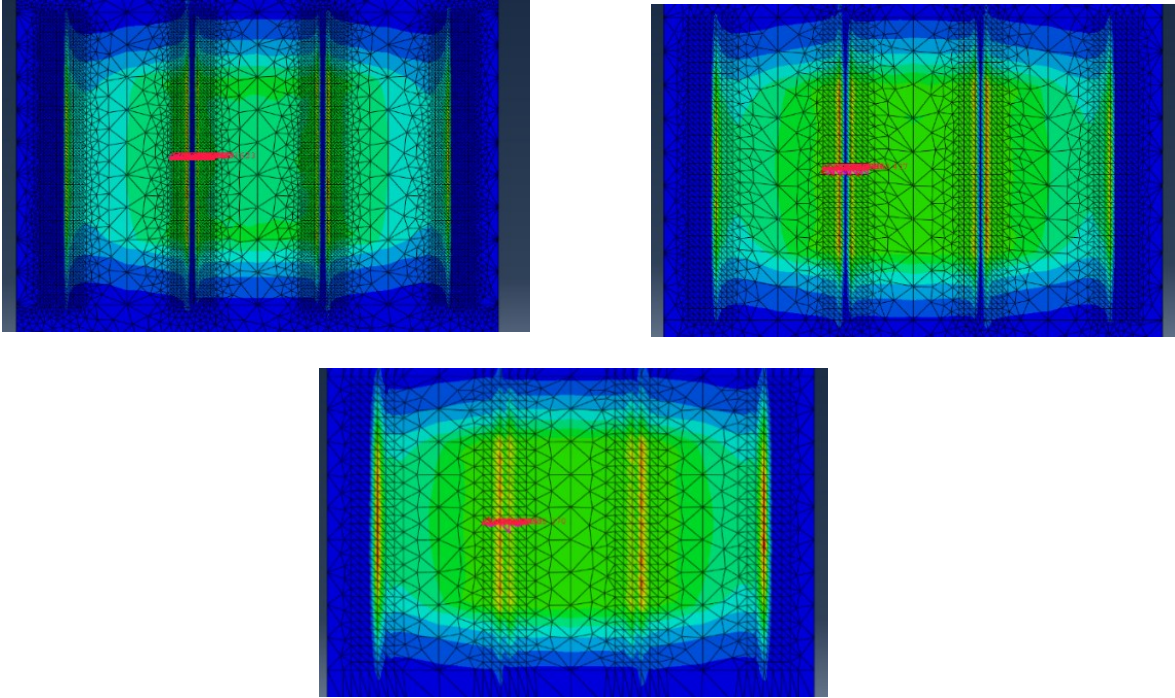
Fig. 3-21: From left to right, up to bottom: 30 mm, 50 mm and 75 mm meshes.
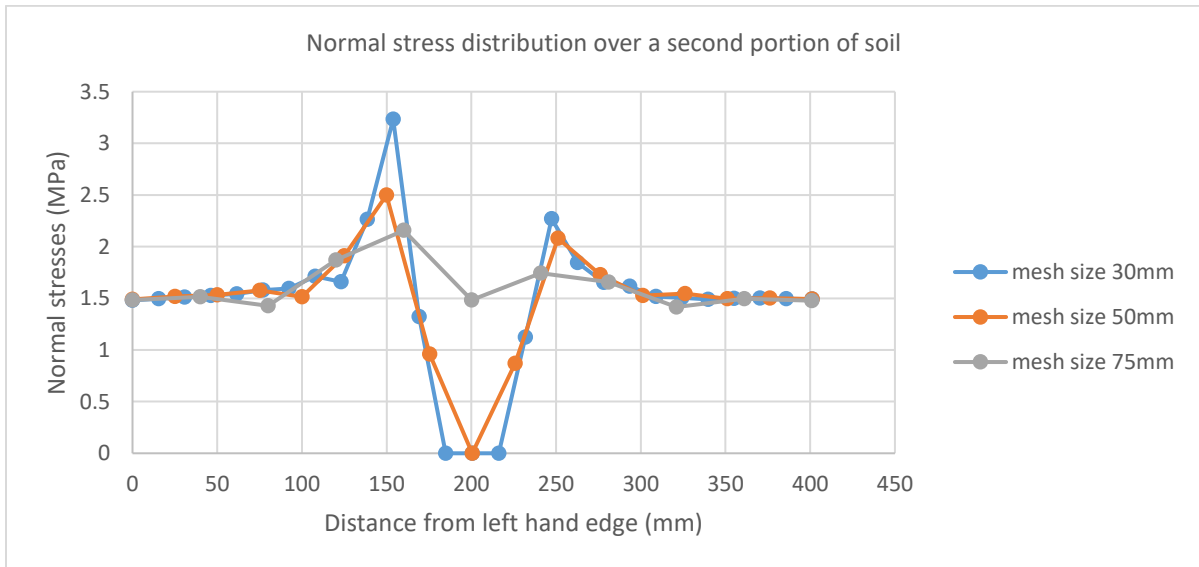
Fig. 3-22: Stress distributions along second paths

3.2.3.2.2. Peak stresses with an elasto-plastic soil

It was found that running models with a soil modeled elastically was time wise unpractical, unless the crawler and mat were considered as rigid bodies. The latter configuration was tested once: a Mohr-Coulomb plasticity assumption was included in the model, according to Sand Fill

soil's physical properties reported in Table 3-3. This was done to decide whether peak stresses could have been the product of a simplistic modeling of the soil. The normal stress and surface contour plot in Fig. 3-23 were obtained.
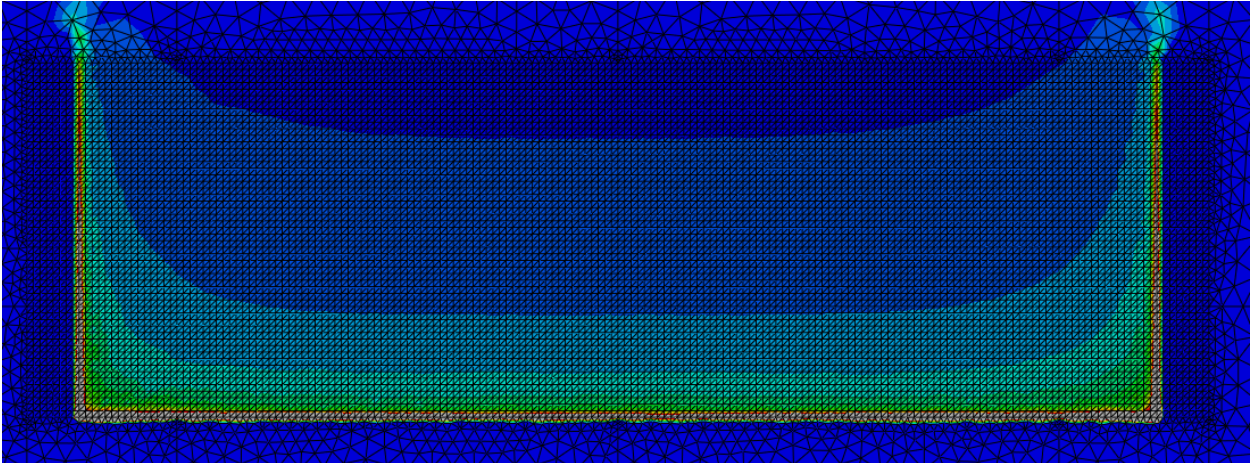
Fig. 3-23: Normal stress contour plot with soil modeled elasto-plastically, {crawler + mat} = rigid body
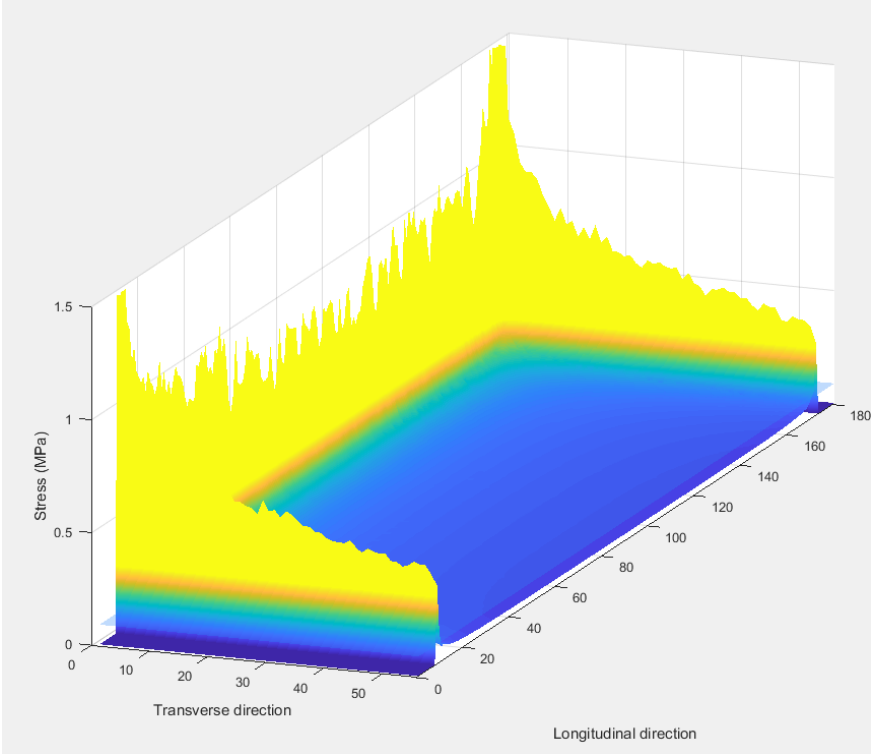
Fig. 3-24: Surface plot on Matlab with soil modeled elasto-plastically, {crawler + mat} = rigid body

The job report showed that plasticity was reached early in the analysis. The presence of peak stresses on Fig. 3-23 thereby reinforces the idea of the existence of peak stresses. In the rest of the study, however, soils will be modeled elastically only, for jobs' running speed purposes.

3.2.3.2.3. Investigation on the appropriate mesh size to use

Now that it is known that peak stresses are not an anomaly generated by Abaqus algorithms, the focus is made on the stress distribution between these peak stresses. In particular, the relevance of the mesh size is to be discussed.

In order to determine the impact of the mesh size on stress distributions, a full path along one side of the mat was taken for each mesh's size -30 mm, 50 mm and 75 mm- and localized paths were considered for a different mesh size so as to compare the slopes of the latter with the slope of the full path (Fig. 3-25). Stress distributions were plotted along the paths and superimposed. This maneuver was carried out between the mesh sizes of 30 mm and 50 mm on the one hand, and 50 mm and 75 mm on the other hand (Fig. 3-26 and Fig. 3-27). One detail needs to be clarified: the elements' sizes differ between different meshes, and given that paths are taken along the elements, and that the points considered by Abaqus for the paths are located at these elements' corners, plotted points of different meshes will not have the same abscissa. This did not matter for the analysis since what was analyzed was the shape of stress curves.
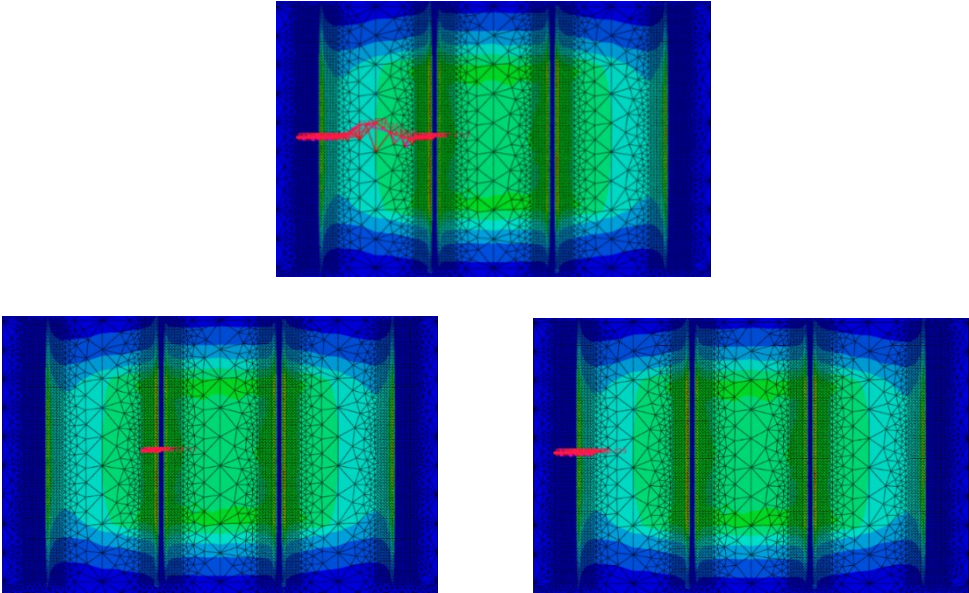
Fig. 3-25: Up: path along one full side of the 30mm mesh. Bottom, from left to right: path at the same level, on the right hand and left hand sides respectively, of the 50mm mesh

Fig. 3-26 shows curves overlapping. Apart from the areas at the immediate neighborhoods of peak stresses which are known to differ from one mesh to another (Fig. 3-20), the onsets of slopes on the left and right sides of a first mesh are perfectly superimposed with the slopes of the
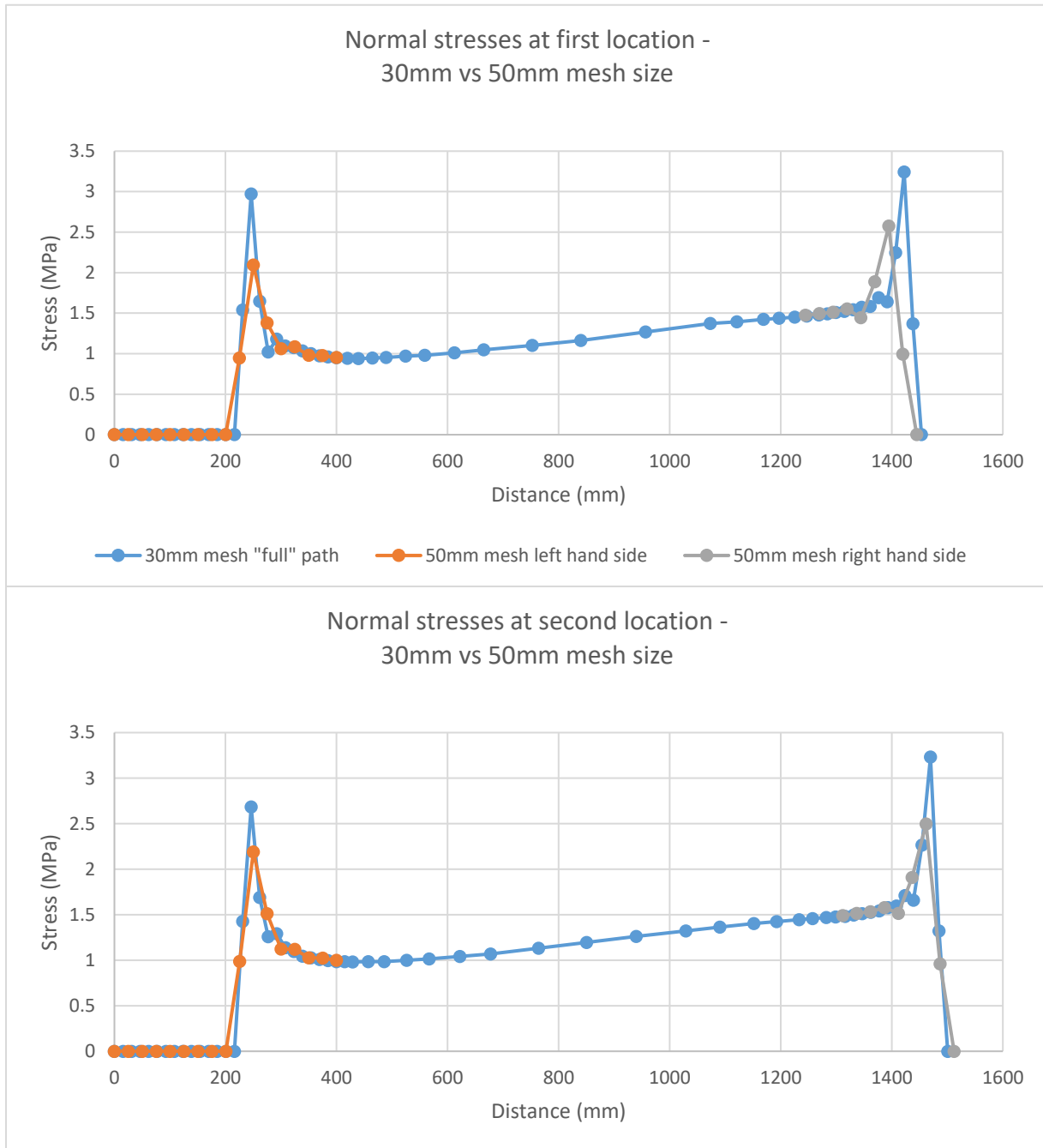
Fig. 3-26: From top to bottom: superimposed stress distributions on first and second paths between 30 mm and 50 mm elements meshes

full path of the second mesh. It means that it is unnecessary to refine the mesh from 50 mm to 30 mm elements to improve the results significantly. On the areas very close to peak stresses though, a refined mesh seems to be necessary to obtain values as close to actual values as possible. Fig. 3-27 shows slopes that do not perfectly superimpose, because of the meshes' coarseness. The overlapping will nonetheless be assumed sufficiently accurate, which is proved right on Fig. 3-32, and insofar as peak stresses cannot be suppressed with finer meshes (Fig. 3-20), they will be neglected of the study. To optimize computing time, a mesh of 75 mm elements will therefore be considered in the rest of this thesis.
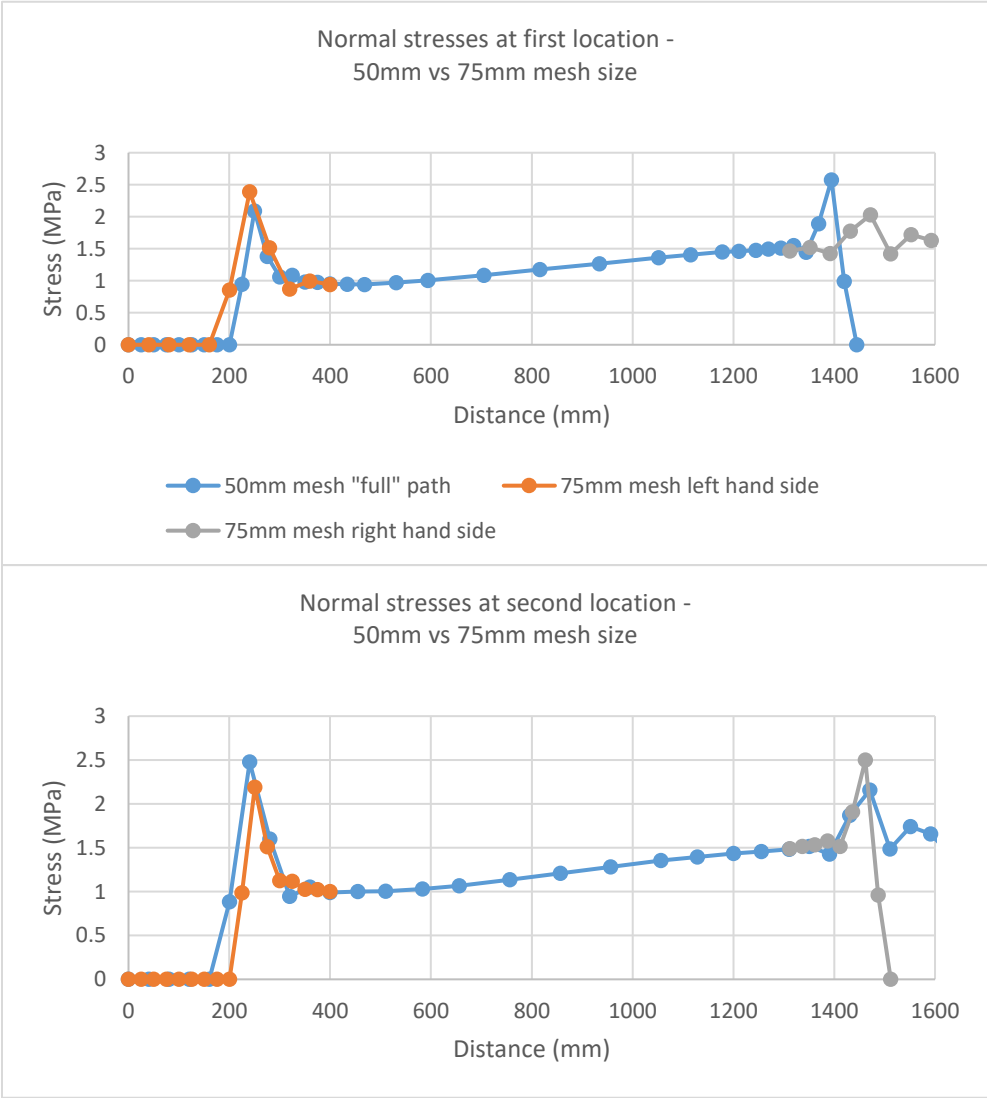
Fig. 3-27: From top to bottom: superimposition of stress distributions on first and second paths between 50 mm and 75 mm element meshes

3.3. Analysis of stress distributions beneath the timber mats

3.3.1. Effects of crawler stiffness on stress distributions

The objective of this part is to gauge the validity of the crawler's rigid body assumption by inspecting the stress distribution beneath the timber mats. In particular, the stress distributions resulting from ten different crawler stiffness values were tested and compared with one another.

3.3.1.1. Method

What was looked for was a law of evolution of the stress distributions as a function of the crawler's rigidity. Such a law could then be used in the opposite sense to deduce, by interpolation, the stress distribution created by any crawler provided its stiffness is granted. It is known that the rigidity of the beam can be related to its geometric dimensions; the following steps were carried out to investigate the relationship between the rigidity of the crawler and the stress distribution: 1) carrying out several simulations of the model with the changing parameter set as the crawler's shell thickness, i.e. the crawler's geometric dimensions, 2) collecting the normal stress data beneath the soil for each simulation, and 3) comparing the stress distributions with the stress distribution generated by a crawler whose stiffness is assumed to be unattainable in practice.

Ten shell thicknesses were tested in total, on Sand Fill soil. It is unnecessary to have a closer focus on the soil type yet as what is to be shown here is essentially the shape of stress distributions. Table 3-4 relates these shell thicknesses to the crawler's rigidity:

Table 3-4: Rigidities calculated from corresponding crawler's dimensions

Shell thickness (m)	Ixx: Area moment of inertia (m^4)	Rigidity: EI (N.m^2.10^{11})	Shell thickness (m)	Ixx: Area moment of inertia (m^4)	Rigidity: EI (N.m^2. 10^{11})
0.075	0.31	0.650	0.19	0.76	1.60
0.1	0.41	0.861	0.22	0.88	1.85
0.125	0.51	1.07	0.25	0.99	2.09
0.15	0.608	1.28	0.375	1.46	3.06
0.17	0.69	1.44	0.5	1.91	4.02

In Abaqus, the definition of the shell thickness in the way the shell beam was constructed exactly corresponds to the crawler's web and flanges' thicknesses. As Table 3-4 displays it, shell thicknesses ranged from 75 mm to 500 mm. A 500 mm thick shell is an unrealistic thickness, and

will therefore be taken as a reference, for I-beams with flanges and webs of 0.5 m are too wide to be built in the scope of this study, or even in the industry.

Despite different dimensions, Liebherr's crawler (Fig. 3-1) has a rigidity very close to a 0.15 m shell thickness'. The role played by rigidity in stress distributions will be discussed in *3.4. Effects of I-beam's dimensions on stress distribution.*

3.3.1.2. In the direction along the crawler's length

A path exactly parallel to the crawler's length was drawn to collect the normal stress data on the soil (

Fig. *3-28*). The same path was used for every shell thickness.
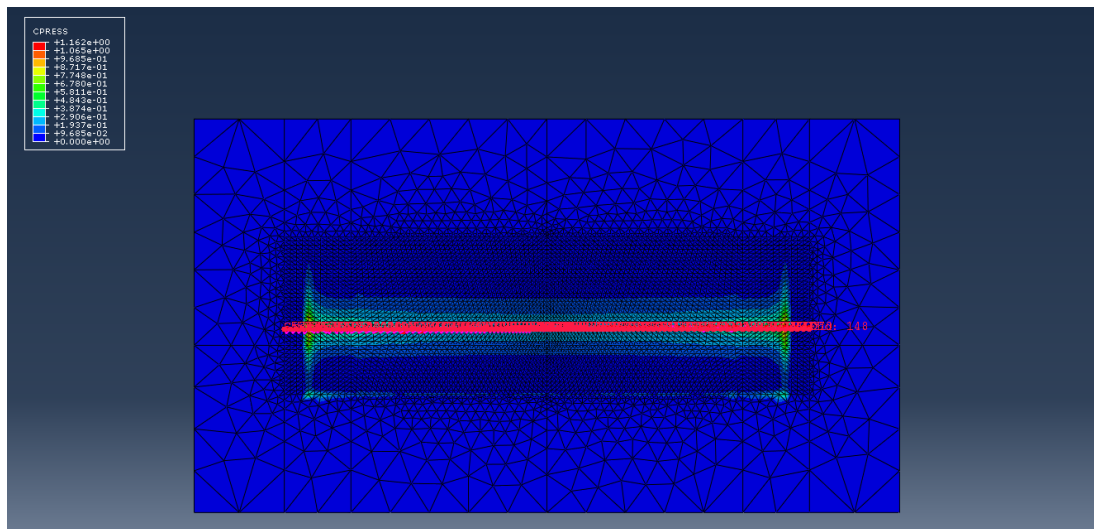
Fig. 3-28: Normal stress contour plot beneath the mats with longitudinal path in red

Fig. 3-29 displays the stress distributions along that path, for three different shell thicknesses. It shows that the curves' shape is similar for each shell thickness; the magnitude of stresses and the curves' flatness are the parameters that change. The more rigid the crawler, the more it redistributes the loads in the direction parallel to the crawler's length, thus the smaller the stresses experienced beneath the mats. Five points are highlighted in order to have a clearer viewing to which sections of the crawler this curve refers to: the transition between the absence of mat and the first mat, characterized by peak stresses as seen in *3.2.3. Analysis of peak stresses beneath the timber mats*; the projections of point loads on the soil, which are highlighted by a jump

33

in stress; and the transitions between the first four mats, also observable by small bumps in stress. The further the transitions from point loads, the smaller the bumps.
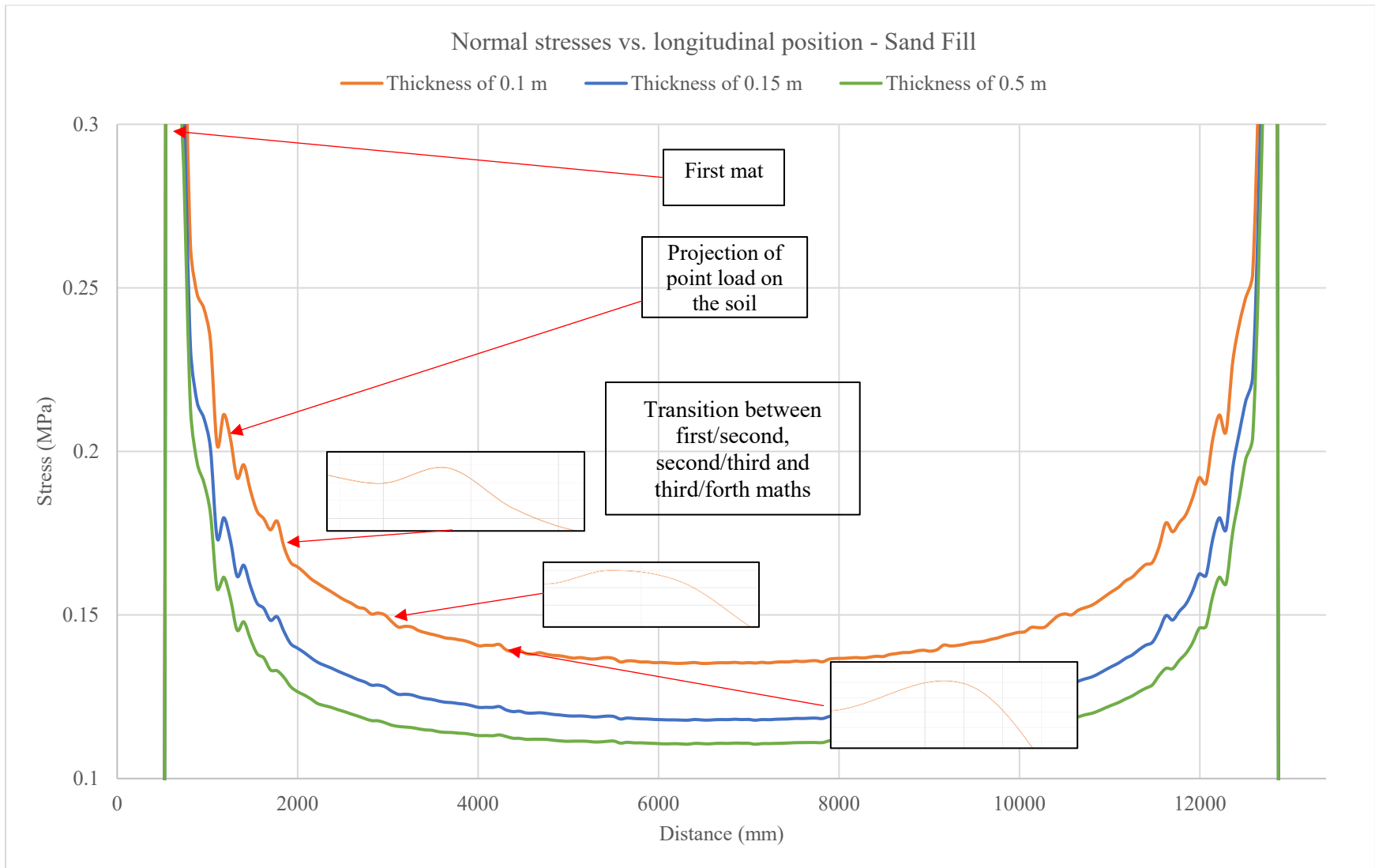
Fig. 3-29: Normal stresses vs. longitudinal position for different shell thicknesses – Sand Fill

3.3.1.3.   In the direction along crawler's width

A path perpendicular to the crawler's length was drawn (Fig. 3-30), and normal stresses were collected along it for every shell thickness, and the stress distributions of the three same shell thicknesses as in Fig. 3-29 were plotted (Fig. 3-31).
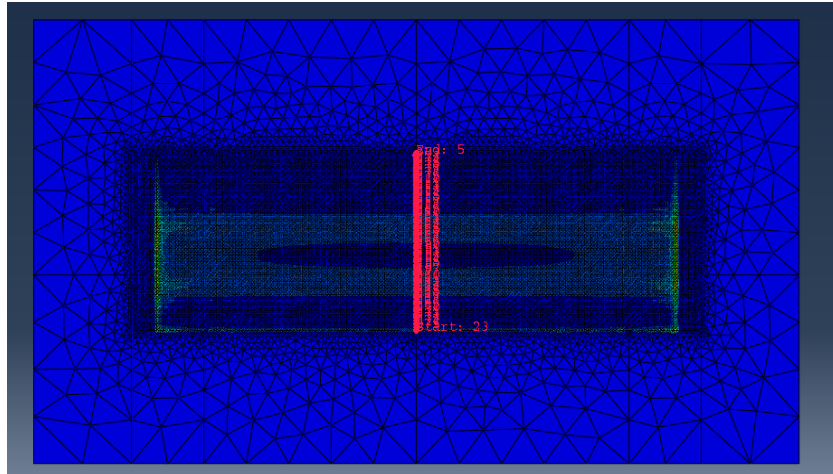
Fig. 3-30: Normal stress contour plot with transverse path in red
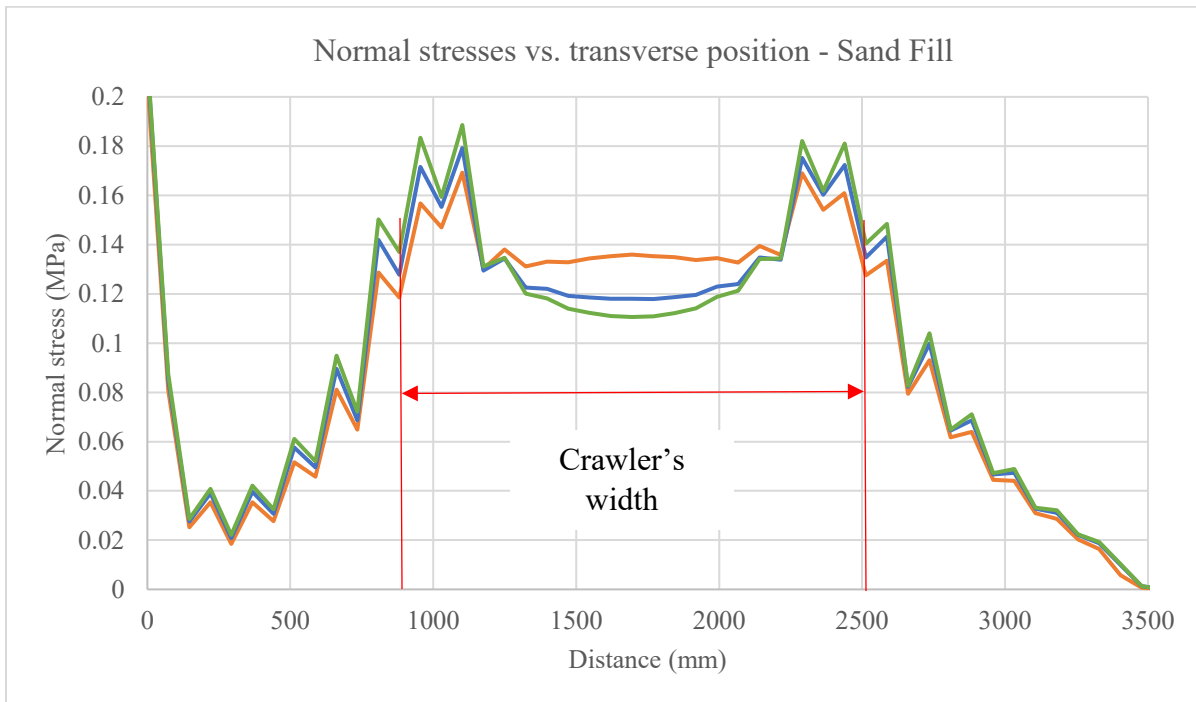
Fig. 3-31: Normal stresses vs. transverse position for different shell thicknesses – Sand Fill

The distributions on Fig. 3-31 ought to be compared to the crawler's width. The higher the crawler's stiffness, the more stresses are redistributed towards its edges. In the same manner peak stresses were observed underneath the layer of mats' ends, high stress values are noted on the areas at the location of the crawler's edges. Since a higher stiffness leads to a more significant stress propagation sideways, the increase in the stiffness leads to higher peak stresses at the edges and lower stresses in the middle area beneath the crawler. Cui and Zhou (Fig. 2-6) observed similar peak stresses on the stress distribution obtained with a rigid plate, on a clay soil (E = 0.784 MPa, v=0.33); for a reason that has not been found, peak stresses were not observed on a sandy soil (E = 13 MPa, v = 0.3), despite its properties being closer to those of the soils studied in this thesis.

The analysis of the transverse curves also needs to be coupled with the analysis of the longitudinal curves. The gain in stress uniformity in the zone right beneath the crawler as its stiffness increases leads to an increase of stresses under the edges. The high stress values, however, are located on narrower portions of soil than where the gain in uniformity takes place. These punctual peak stresses may therefore lead to a greater local subsidence of the soil but is not likely to endanger the system as a whole.

3.3.2. Effects of soil type on stress distribution

As a recall, the soils were assumed to be homogeneous and to have a linear elastic behavior. Therefore, they were only defined by their Young's modulus E and Poisson's ratio v, which are displayed in Table 3-5:

Table 3-5: Four soils' elastic properties

	E (MPa)	v
Sand Fill	33	0.3
Native Sand	55	0.3
Clay Till	120	0.49
Sand and Gravel Fill	150	0.15

Simulations on the ten shell thicknesses were carried out for the four soil types: Sand Fill, Native Sand, Clay Till and Sand & Gravel, which add up to forty different simulations. Fig. 3-32 illustrates how the mesh's coarsification (from 50 mm to 75 mm elements) affects the results'

37

accuracy. It displays the stress distributions of the 0.1 m and 0.5 m shell thicknesses on Native Sand's soil for the fine mesh (50 mm elements), and the coarse mesh (75 mm elements, as advocated in *3.2.3.2.2. Peak stresses with an elasto-plastic soil*).
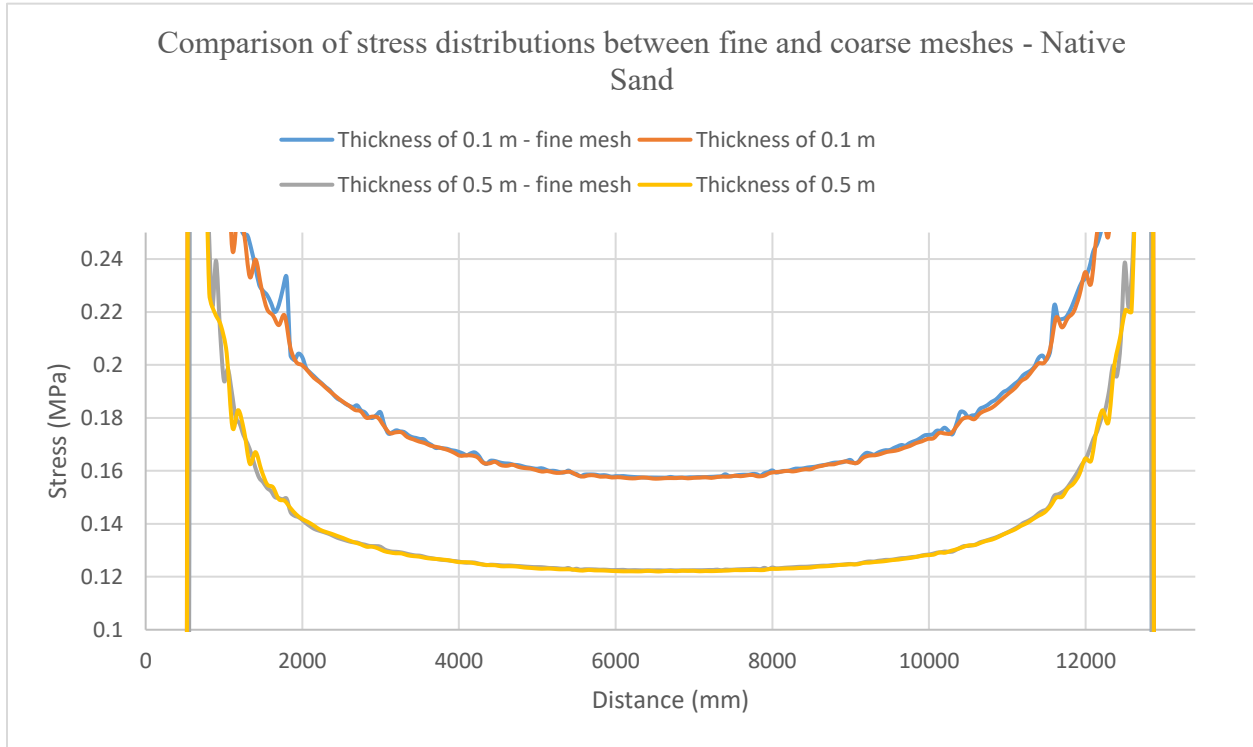
Fig. 3-32: Comparison of longitudinal stress distributions between fine and coarse meshes – Native Sand

Fig. 3-32 shows fairly well that the stress deviation between the fine and coarse meshes, for a given shell thickness, is negligible. Table 3-6 summarizes the average relative stress error between the coarse and fine meshes for Liebherr's crawler and the 0.5 m shell thickness, for every soil type:

Table 3-6: Average relative stress error between a fine and coarse mesh

	Average relative error Liebherr's crawler (%)	Average relative error 0.5m thickness (%)
Sand Fill	1.8	0.8
Clay Till	1.7	5.1
Native Sand	1.7	1.5
Sand and Gravel Fill	1.7	1.5

This chart shows that the average differences in stress for both these shell thicknesses are small, with the exception of Clay Till for a 0.5 m thick crawler, which can be accountable to the important oscillations of stress distributions on Clay Till soil between each point, as it will be discussed later in more detail. In the rest of the study, the relative error made by using a coarse mesh in order to optimize the simulations' running time will be considered insignificant.

Fig. 3-33 and Fig. 3-34 show plots of stress distributions on the four soil types, for different crawler's stiffness. The scales were adapted and kept the same on Fig. 3-33 and Fig. 3-34 separately so as to highlight the evolution of soils' behavior between one another. The two next sections comment these figures.
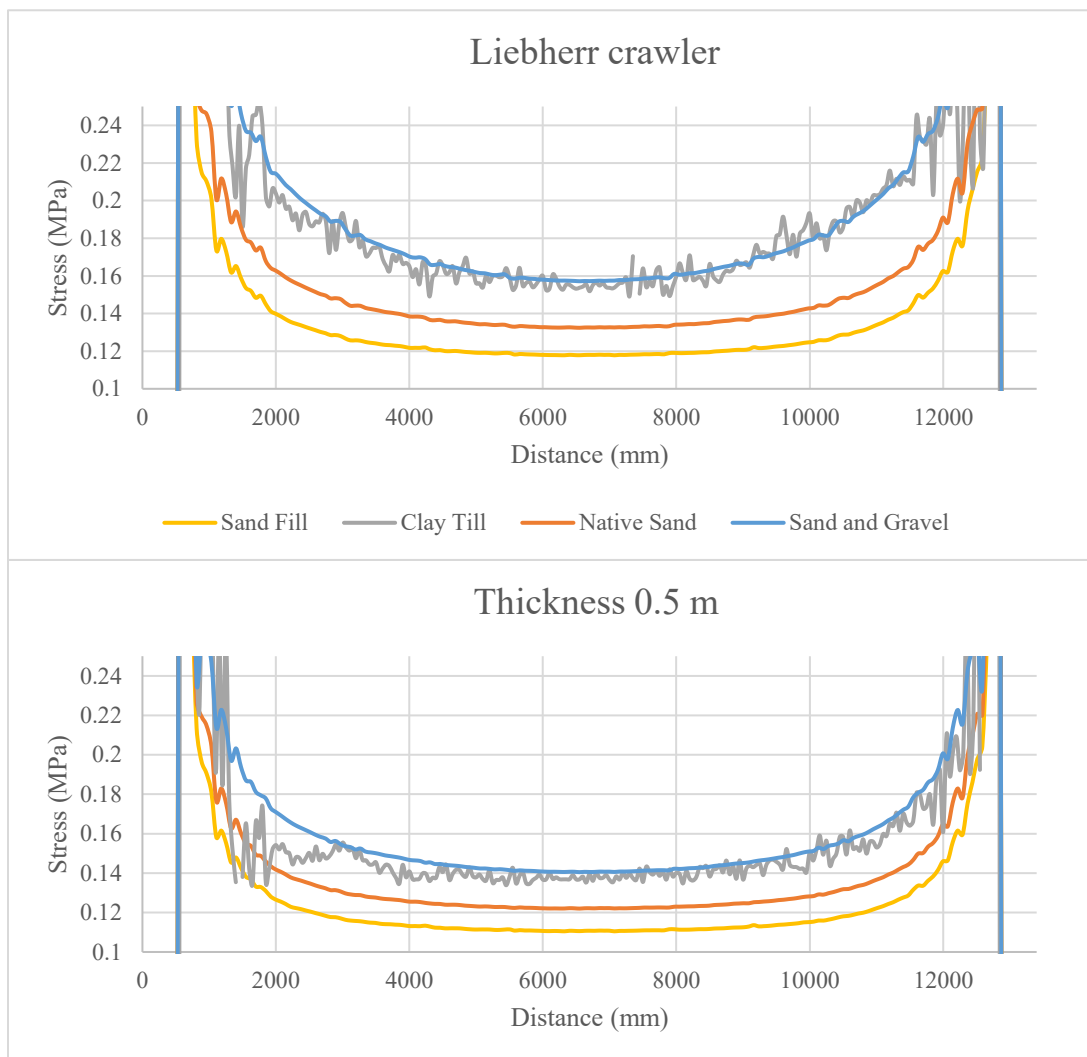
Fig. 3-33: Longitudinal stress distributions of the four soil types, two shell thicknesses
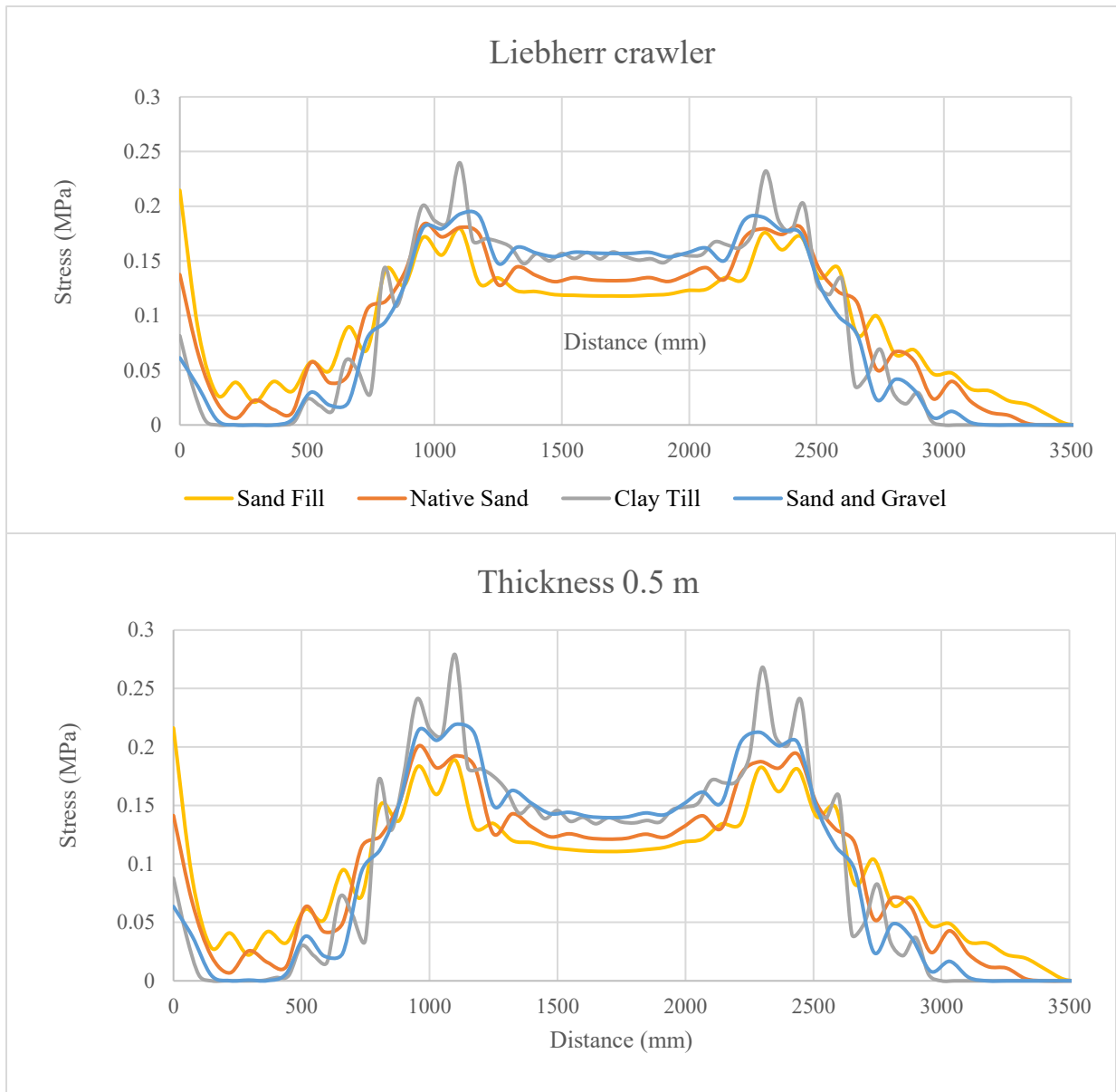
Fig. 3-34: Transverse stress distributions of the four soil types, two shell thicknesses

3.3.2.1.   Effect of Young's modulus

Fig. 3-33 and Fig. 3-34 show that for equal values of crawler's dimensions, i.e. equal stiffness, stress distributions on the soil are significantly dissimilar from a soil type to another. As per Table 3-5, two groups of soils may be regarded separately: Sand Fill and Native Sand on the one hand, which have the same Poisson's ratio and neighbor Young's modulus; Clay Till and Sand & Gravel on the other hand, with neighbor Young's modulus despite different Poisson' ratio.

When comparing Sand Fill and Native Sand, which have equal Poisson's ratio, it is seen that a bigger Young's modulus leads to less uniformly distributed stresses, and as a result increases the stress distributions. The less rigid soil can be regarded as a damper compared to the stiffer soil, thus stresses are more uniform. This result had already been observed by Cui and Zhou (Fig. 2-6): the stress distribution obtained with a rigid plate (black squares) is lower on the clay soil (E = 0.785 MPa) than that obtained on the sandy soil (E = 13 MPa). On the other hand, Corey and Han (Fig. 2-8 and Fig. 2-9) found that a dense soil redistributed their concentrated load more uniformly than the loose soil. It has to be underlined that the elastic properties of the dense soil (E = 40 MPa; v = 0.35) and the soft soil (E = 20 MPa; v = 0.3) are quite close though, and that they included plasticity in their model. In particular, the dense soil's friction angle is higher than the soft soil's (40° against 30°). Further work would be needed to understand the influence of Mohr-Coulomb model on the stress distributions.

3.3.2.2. Effect of Poisson's ratio

Even though stress distributions vary between soils (Fig. 3-33 and Fig. 3-34), they all behave similarly, with the exception of Clay Till, whose joint difference with the three other soils is to have a high Poisson's ratio, close to 0.5. According to the conclusion made by the analysis of Sand Fill and Native Sand, Clay Till should display stresses lower than Sand & Gravel; the opposite is observed, stresses on Clay Till are about as high as on Sand & Gravel, and higher on the Liebherr's crawler graph (Fig. 3-33). Clay Till's physical parameters account for that, its high Poisson's ratio leads to a significantly high bulk modulus, thus making it behave as an incompressible material. A consequence of this peculiarity is to locally exhibit turbulences, the way a rubber would do, and to lift up stress distributions to make them less uniform.

3.3.3. Quantification of the variations of stress distributions as a function of soil type and crawler stiffness

It is commonly assumed in the industry that stress distribution beneath cranes' timber mats are uniform. It presupposes that the mats and crawler are fully rigid, so that they redistribute the loads throughout their entire surface. This section questions this assumption.

3.3.3.1. Method

Stress distributions generated by every shell thickness, i.e. every crawler stiffness, on every soil, were compared to the 0.5 m thick shell of reference to quantify the variations of stress distributions as a function of soil type and crawler stiffness. The 0.5 m thick shell was assumed to be a rigid body. A second assumption is that the beam's rigidity is the only parameter to play a role in the loads' redistribution. As *3.4. Effects of I-beam's dimensions on stress distribution* shows it, that assumption tends to be true when beams have realistic dimensions.

3.3.3.2. Quantification of the uniformity of the transmission of loads to the soil as a function of soil type and crawler stiffness

The concept of "plateau" was defined in this study in order to quantify the uniformity of stress distributions beneath the mats. On the longitudinal stress distribution shown in Fig. 3-35 is highlighted a "plateau" in orange; it corresponds to the area where stresses are comprised within 10% of the minimum value.
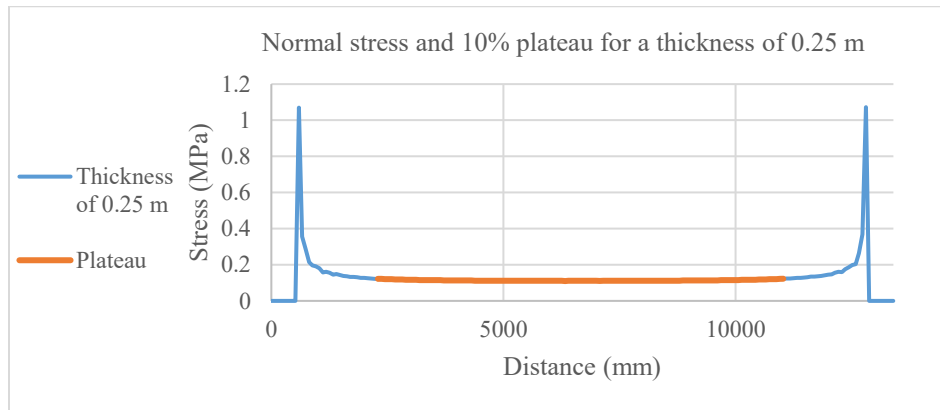
Fig. 3-35: Stress distribution with a 0.25 m shell thickness with highlighted plateau

The value of 10% was chosen arbitrarily, for a relative error of 10% or less is generally admitted in Structures and Geotechnical because of the numerous approximations and margins of errors that the fields require.

The length of the plateau characterizes the uniformity of stresses. The wider the plateau, the closer are stresses to the minimum, and therefore the more uniformly distributed are the stresses. As a result, in order to study the uniformity of stresses as a function of soil type and

crawler's stiffness, the ratio of plateaus' length over the crawler's length was plotted for the ten shell thicknesses and the four soils in Fig. 3-36.

The curves on Fig. 3-36 measure the extent of plateaus within the crawler. It can be noted that the order with which different soils are encountered, from top to bottom, is the opposite of the order observed on the longitudinal and transverse stress distributions (Fig. 3-33 and Fig. 3-34). It was expected given that lower stress values on stress distributions imply a better redistribution of loads, and therefore a wider plateau.

Fig. 3-36 confirms that stresses are more uniformly distributed as the crawler's stiffness increases, although the widest plateau is the one on Sand Fill for a shell thickness of 0.5 m, which
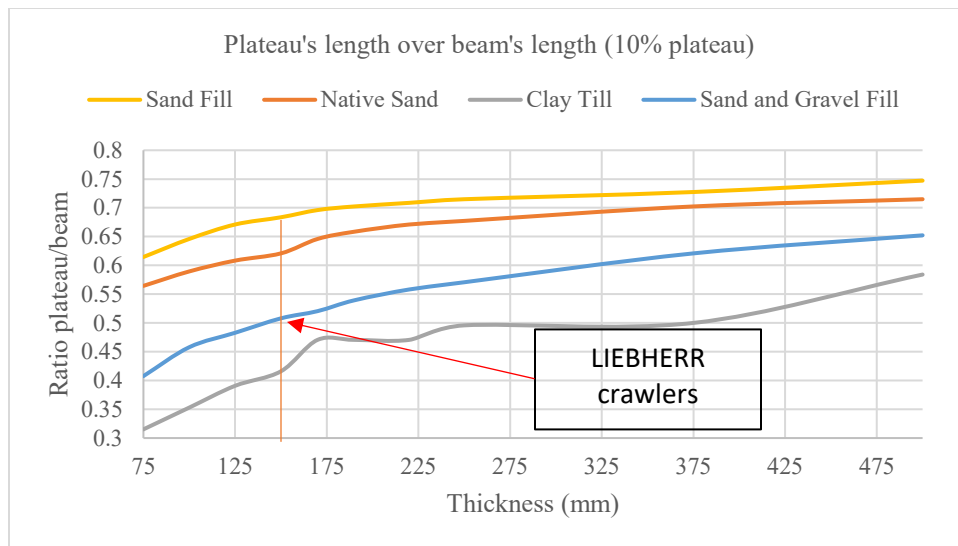
Fig. 3-36: Evolution of the 10 % plateau vs. shell thickness

is only 75% of the beam's length. These results could be said biased due to the presence of peak stresses, which physically require a smooth transition from these peaks to the minimum stress value on the soil; nonetheless, the goal here is to investigate what affects the uniformity of stress distributions. Even though the peak stresses may affect the plateaus' length, the conclusion that the crawler's rigidity influences it holds true.

Fig. 3-36 also attests that a high Poisson's ratio is not in favor of a good load redistribution. Based on Young's modulus values, Clay Till's curve would be expected to be above Sand & Gravel's; this is not observed.

3.3.3.3. Quantification of the increase or decrease of stresses as a function of soil type and crawler stiffness

The quantification of the rate of decrease of stresses as the crawler's dimensions increase was done by computing the stress deviation between each point of every stiffness and the points of the 0.5 m shell thickness (assumed to be rigid). The stress deviation was then averaged and plotted against the shell thickness for every soil (Fig. 3-37).

Since all the stress values on Fig. 3-37 are compared with those obtained with a 0.5 m shell thickness, all the curves tend to zero, as a stress distribution is exactly equal to itself.
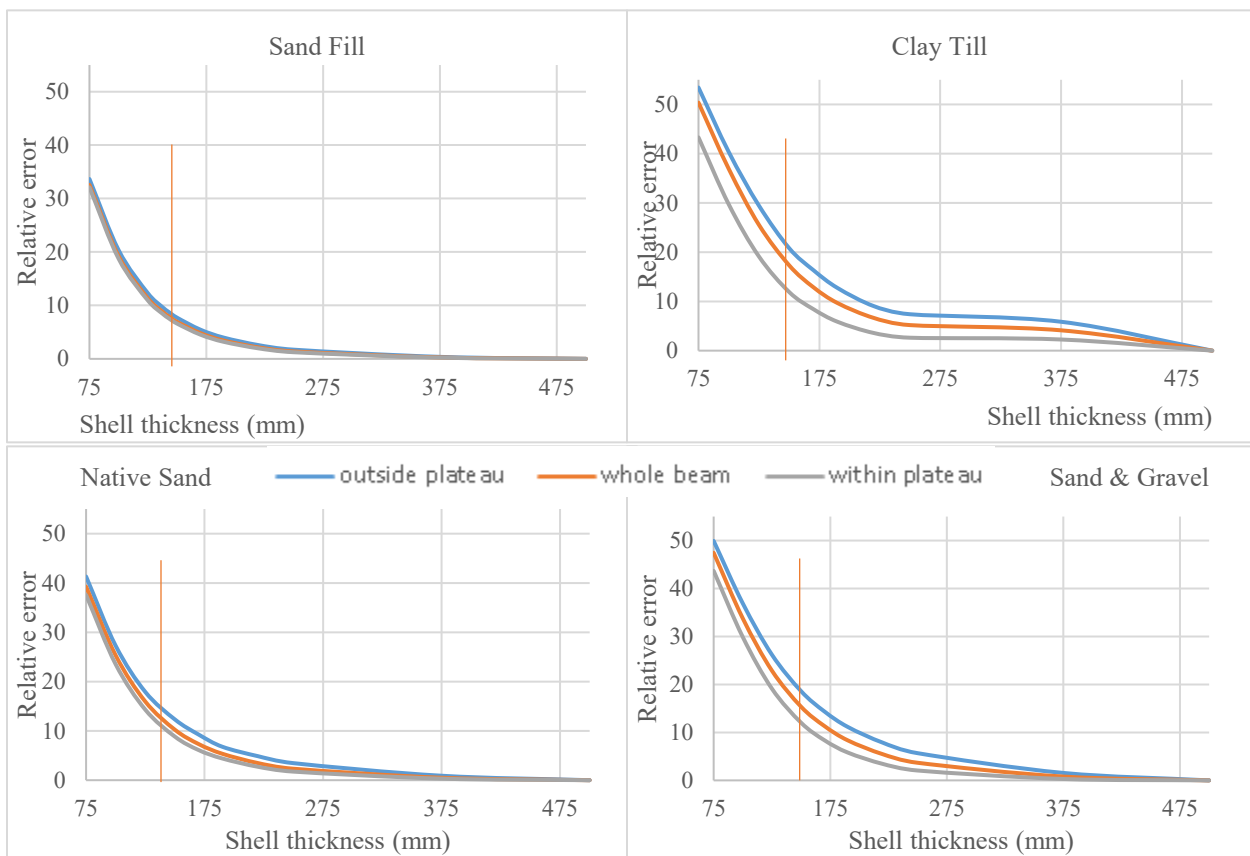
Fig. 3-37: Relative error in stress with 0.5 m shell thickness vs. shell thickness, for the four soils and three areas in the beam

These curves essentially quantify how much higher the stresses would actually be, with respect to what is expected with a rigid crawler. The lines in red are landmarks for Liebherr crawlers, which behave like a 0.15 m thick shell crawler.

44

The stress deviations were calculated in three areas: on the whole beam, outside the plateaus and within the plateaus; every soil has a bundle of three curves. The curves of the first group of soils, Sand Fill and Native Sand, do not differ significantly within a bundle, as opposed to Clay Till and Sand & Gravel for which stress deviations outside the plateau can be up to 10% higher than within the plateau. This suggests that longitudinal stress curves of rigid soils have a higher curvature than soft soils close to the crawlers' ends.

All the curves also display the same bilinear evolution: a first zone (Zone 1) with a steep negative slope followed by a second zone (Zone 2) with a smaller negative slope. The error made by assuming a rigid crawler is therefore bigger when the beam is smaller.

The maximum stress deviation within the plateau and the averaged stress deviation outside the plateau were plotted on Fig. 3-38 and Fig. 3-39 in order to clarify the curves of Fig. 3-37.
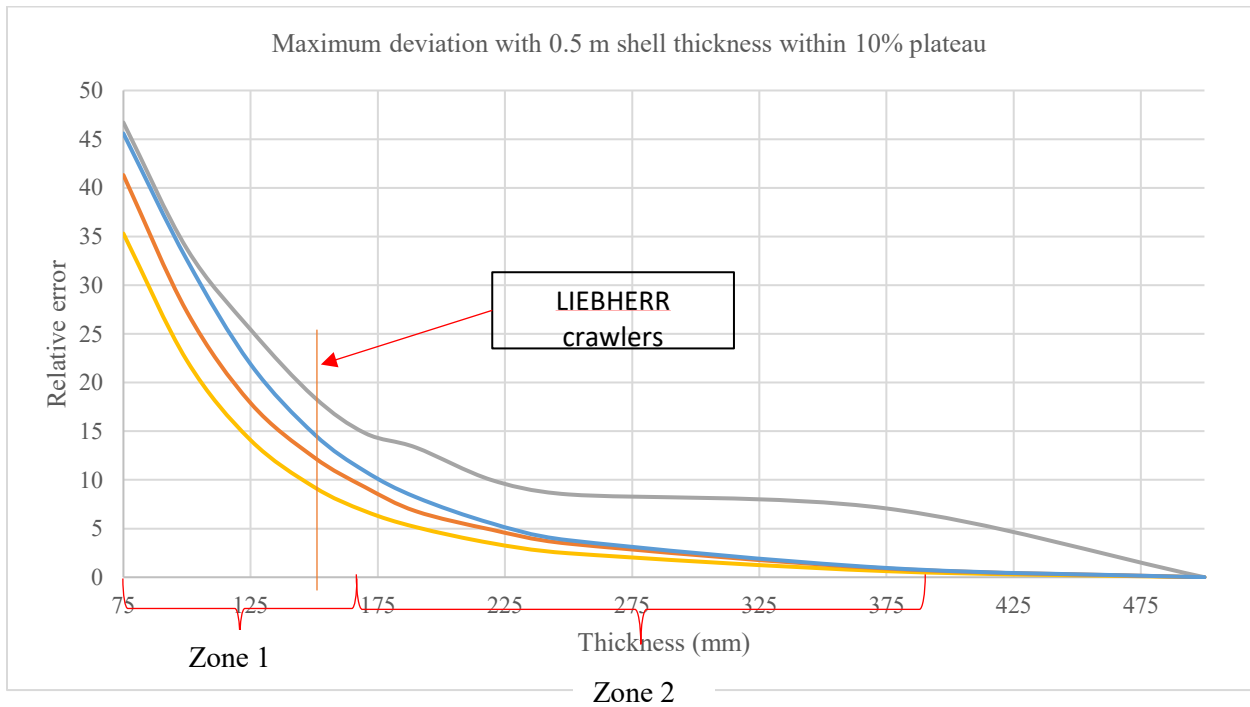
Fig. 3-38: Maximum relative error with 0.5 m shell thickness vs. shell thickness

An important observation on Figs. Fig. *3-38* and Fig. *3-39* is that stress deviations for shell thicknesses higher than 275 mm are smaller than 5%, except for Clay Till. It shows that for Sand Fill, for Native Sand and for Sand & Gravel, it is true, with a relative error of less than 5%, to assume that a 0.5 m thick shell beam is rigid. Concerning Clay Till, the relative error is less than 10%.

45
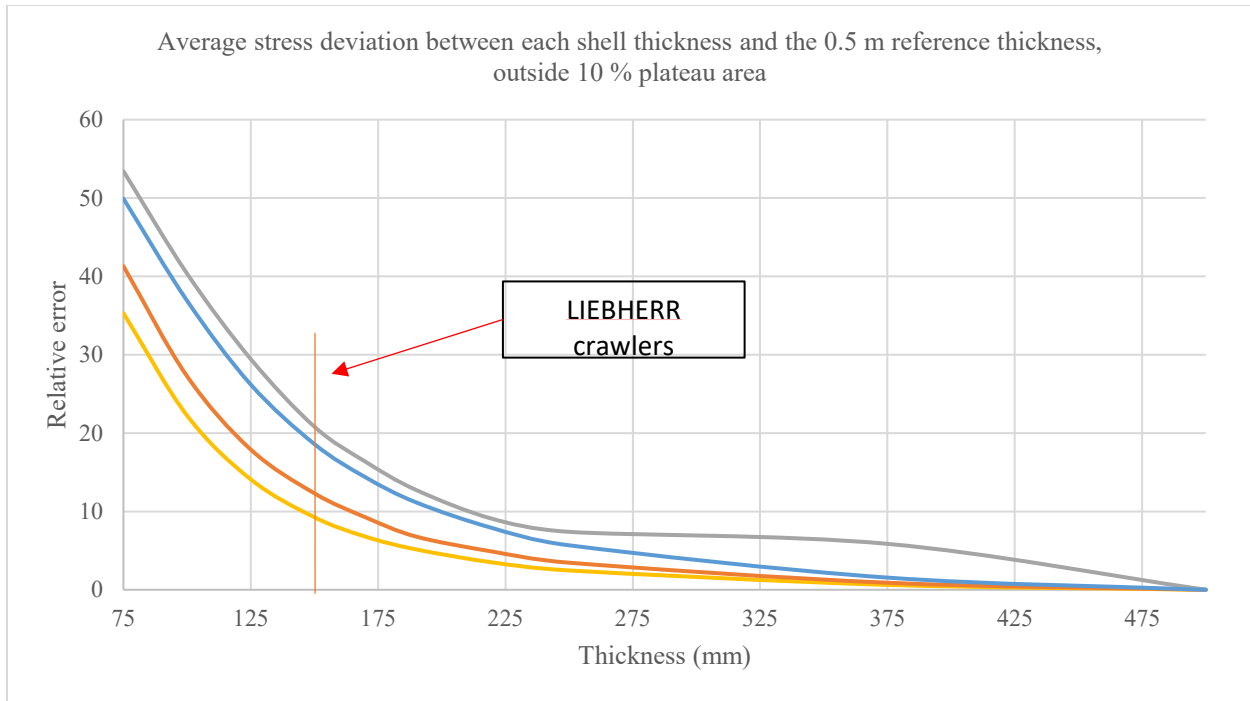
Fig. 3-39: Average relative error with 0.5 m shell thickness vs. shell thickness

A closer focus at Liebherr crawler shows that, be it for the maximum deviation with the 0.5 m shell thickness (Fig. 3-38), or the average stress deviation outside the plateau (Fig. 3-39), the assumption of crawler rigid body is not valid. Depending on the soil type, the stresses actually experienced by the soils are comprised between 10% and 20% higher than what is obtained with a 0.5 m thick shell. Given that the latter is not completely rigid, that interval is in fact a bottom bracket of the actual deviations. Therefore, even though in practice, safety factors are included in designs, a relative error of 10% to 20% is high enough to be taken a closer look at.

It has been shown in this section how stress distributions were behaving as functions of soil types and crawler stiffness. It was assumed throughout the study that the crawler's rigidity was the only factor playing a role in how uniformly stresses were transmitted to the soil; that assumption is widely accepted in beam's theory. The crawler's shell thickness was therefore the only parameter altered between each simulation. As a result, the web's and flanges' thicknesses were modified with the same magnitude and at the same time, making it impossible to know which of the two prevailed over the other in the redistribution of stresses. This raised the question of the

relevance of the results, since the web and flanges were not treated separately and that they rarely have the same dimensions in practice. That question was investigated in the section that follows.

3.4. Effects of I-beam's dimensions on stress distribution

3.4.1. Method

In a first step, Liebherr's crawler was compared with an I-beam with equal rigidity and flange width but having a uniform shell thickness of 150 mm, in order to investigate the impact of the web's thickness on stress distributions. The dimensions and stiffness of these two beams are shown in

Table *3-7*. According to beam's theory, they should redistribute loads almost identically and similar stress distributions should be observed on the soil.

Then in a second step, three different beams with different dimensions and equal stiffness were tested in the same manner. Fig. 3-41 shows these beams' dimensions.

Table 3-7: Rigidities of 0.15 m thick shell beam and Liebherr crawler

	H (mm)	B (mm)	h (mm)	b (mm)	Rigidity: EI (10^{11} N.m^2)
0.15 m shell thickness	1980	1500	150	150	1.277
Libherr crawler	1846	1500	142	355	1.276

3.4.2. Results

3.4.2.1. Significance of the flanges' thickness to efficiently redistribute stresses

In a first step, stresses generated by both beams were collected on several longitudinal paths beneath the timber mats and plotted on the same graph (Fig. 3-40).

Each position "pos" corresponds to a path on the soil. "Pos 24" is the main longitudinal path described before in the study. The paths are further from that main path when their number is higher.

Each couple of curves, i.e. curves matching the 0.15 m shell thickness and Liebherr's crawler, of a given "pos", are almost superimposed, for all positions. The maximum relative error in stress between the two beams is less than 3%. The structure in bowl (Fig. 3-14) can also be

observed on Fig. 3-40: "pos 24" corresponds to its bottom, then the curves are lifted up as stresses increase on the bowl's sides, to finally fade out away from the middle.

Table 3-7 shows that the beams' webs are quite different; Liebherr crawler's web is more than twice as thick as a 0.15 m thick shell's. Their flanges' width is similar, however, which infers that the importance of flanges prevails over the web's.

In a second step, stresses were collected along the same paths as in Fig. 3-40, for the trio of different beams that have equal stiffness (Fig. 3-41). They were plotted on the same graph, Fig. 3-42. That figure shows that stress distributions of a trio of curves are not as close as were couples on Fig. 3-40. For a given trio, the differences are clear for pos 24, pos 31 and pos 35, which correspond to longitudinal paths collected inside the structure in bowl (Fig. 3-14): the thick flanged beam redistribute the loads more uniformly than Liebherr crawler, itself doing a better job than the thinner flanged beam. The relative error in stress between the thick and thin beams are comprised between 8 and 10%.

The analysis of the stress distributions of the 0.15 m thick shell beam and Liebherr crawler allows to conclude that beams with equal flanges and stiffness lead to stress distributions almost superimposable. It can also be concluded that very different beams with equal rigidities may lead to different stress distributions and that thicker flanges seem to lead to better loads redistribution.

The section that follows tests the predominance of flanges over the web by testing two beams with equal rigidities and radically different dimensions, and compare the stress distributions they create beneath the mats.
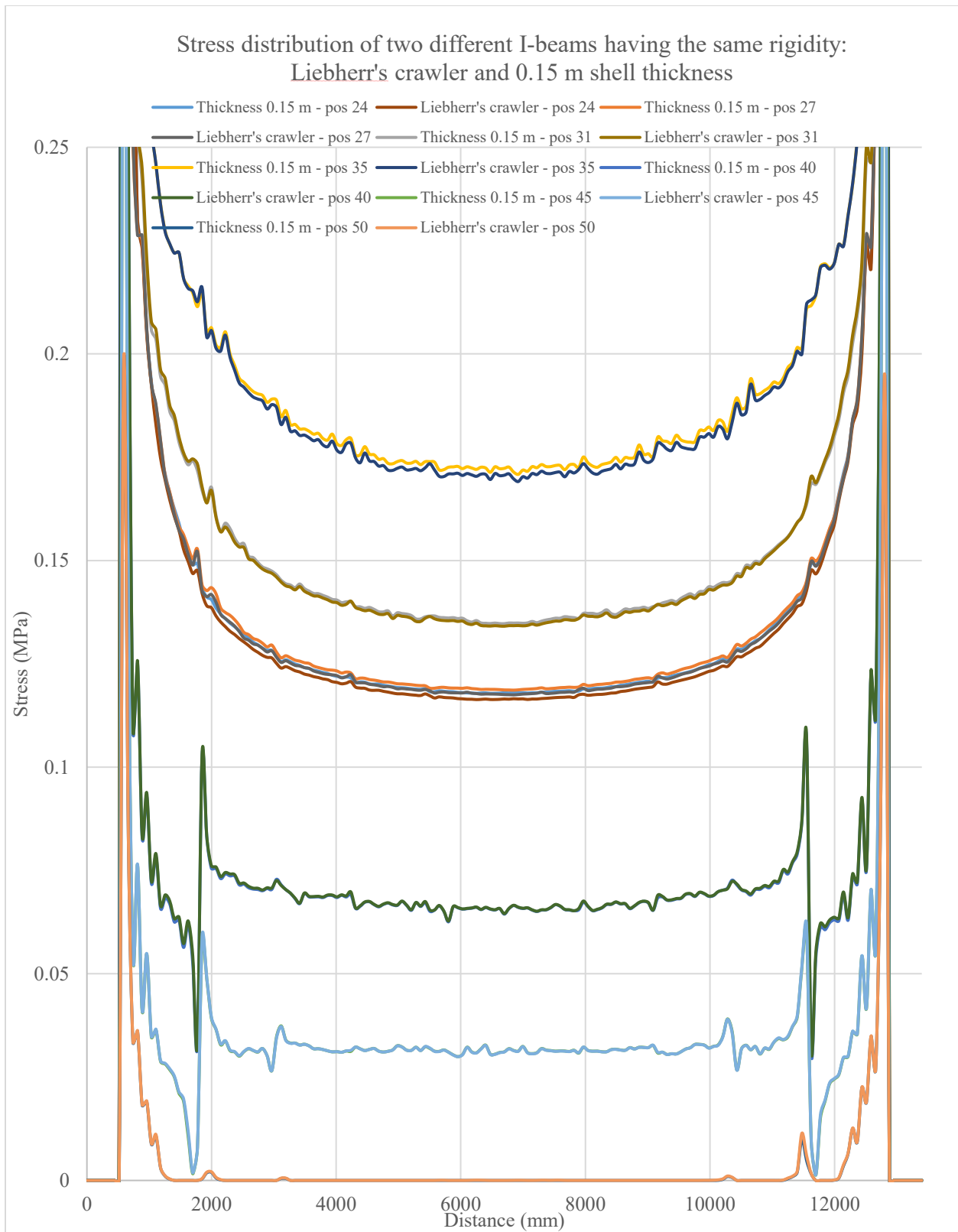
Fig. 3-40: Stress distributions beneath mat generated by 0.15 m thick shell beam and Liebherr crawler
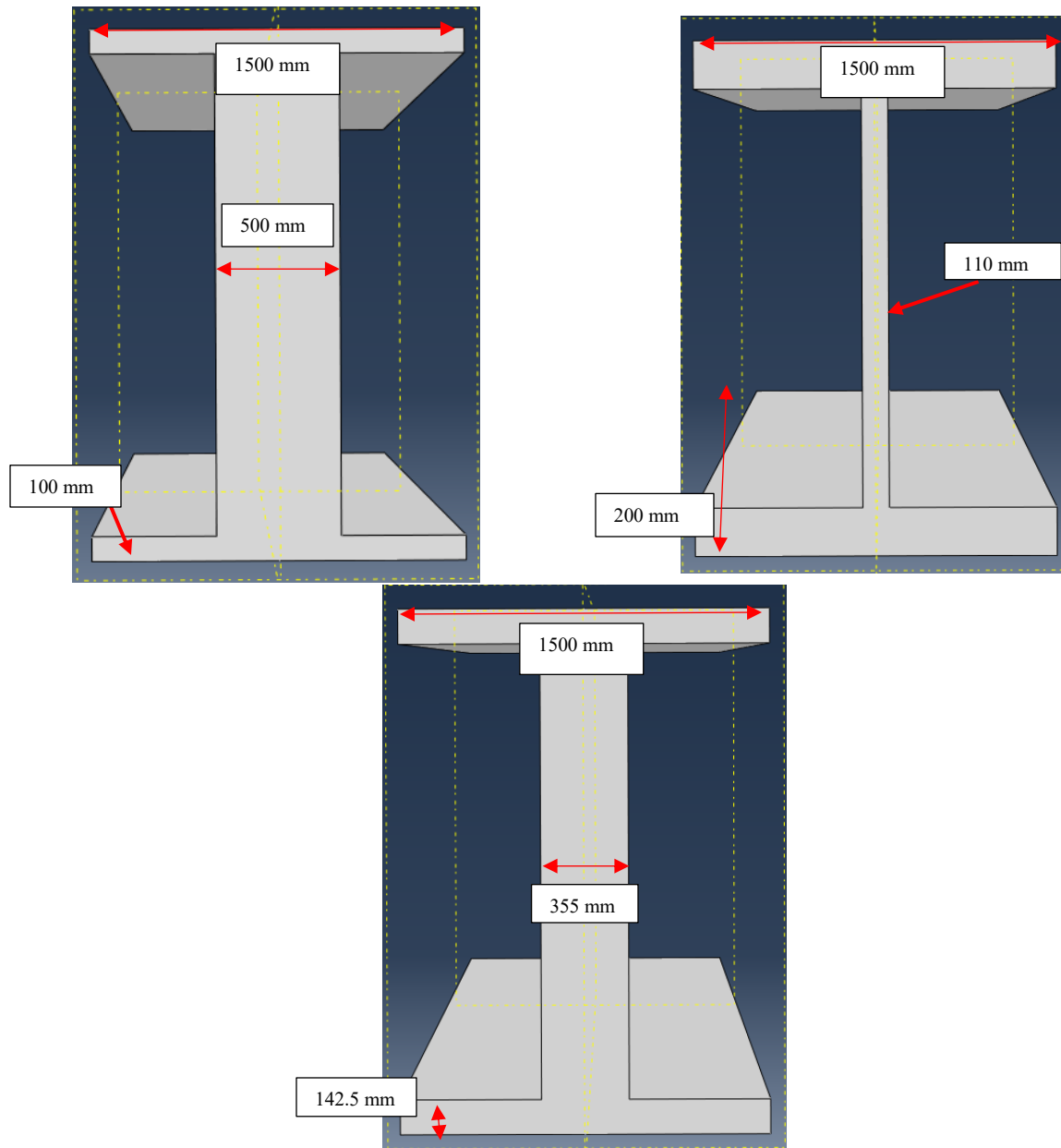
Fig. 3-41: From left to right, top to bottom: wide beam (wide web, thin flanges), thin beam (thin web, wide flanges), Liebherr crawler
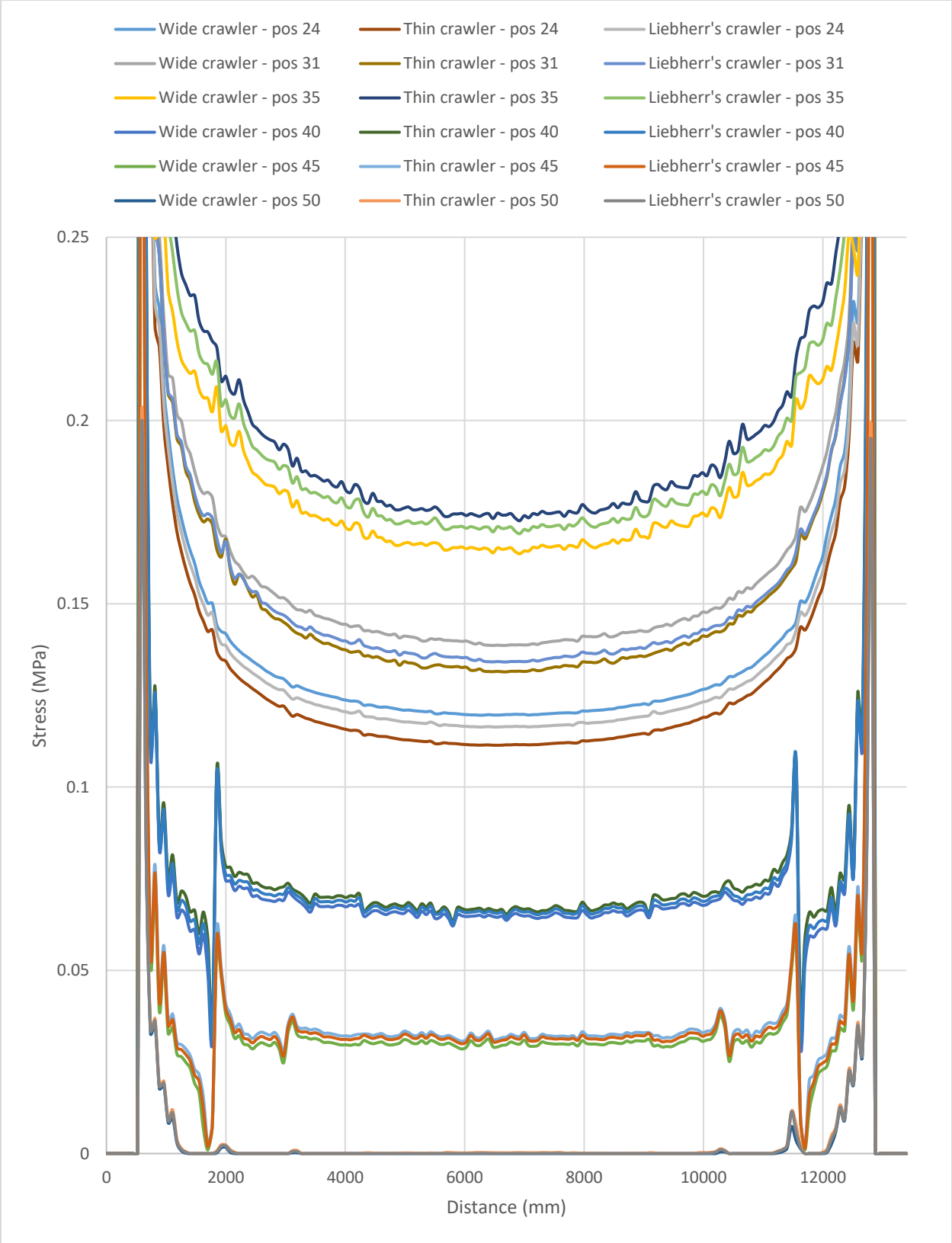
Fig. 3-42: Stress distributions beneath mat generated by wide beam, thin beam and Liebherr crawler

3.4.2.2. Limits of beam theory

It was concluded that beam theory, which predicts that an I-beam's stiffness is the only parameter to play a role in the redistribution of loads, was valid for beams with realistic dimensions. The objective here is to test this theory with beams having extreme dimensions. Two beams with extreme opposite dimensions but equal stiffness were tested (Fig. 3-43), and the stress distributions beneath the timber mats were plotted on Matlab. Their rigidity can be read in Table 3-8.

Table 3-8: Rigidities of fat and skinny beams compared with Liebherr crawler

Shell thickness (m)	Ixx: Area moment of inertia (m^4)	Rigidity: EI (N.m^2.10^{11})
Fat crawler	0.8490	1.7829
Skinny crawler	0.8497	1.7844
Liebherr crawler	0.6077	1.2762
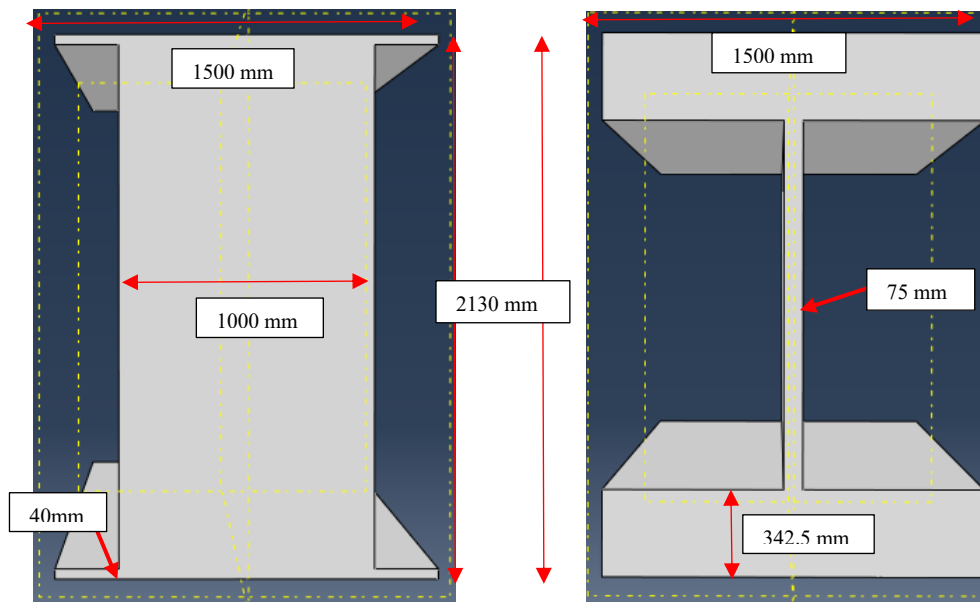
Fig. 3-43: From left to right: fat beam (fat web, skinny flanges), skinny beam (skinny web, fat flanges)
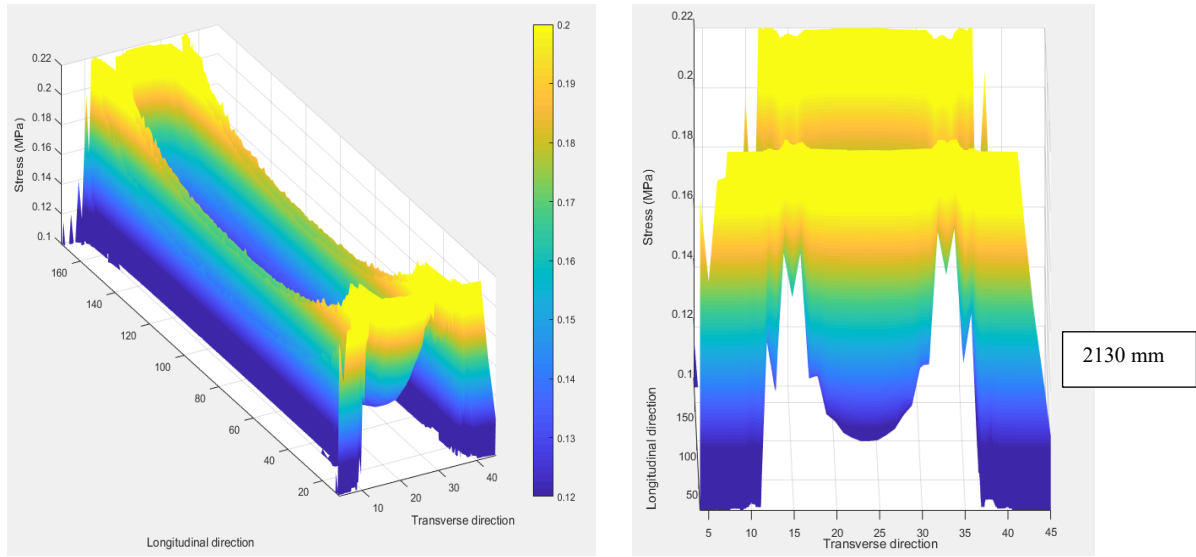
Fig. 3-44: Stress distribution generated by skinny beam, 3D and front views
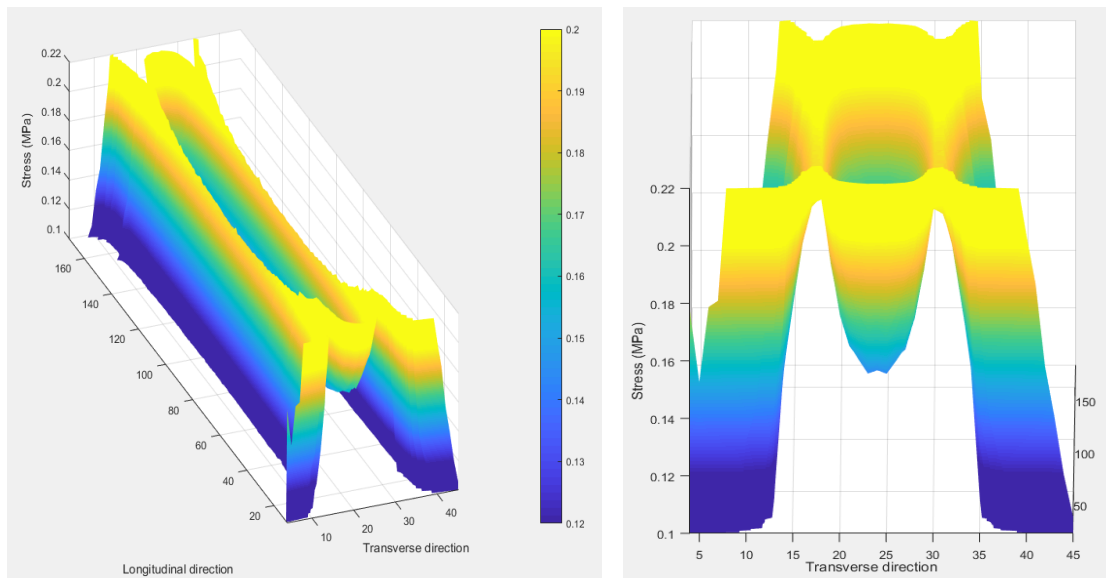
Fig. 3-45: Stress distribution generated by fat beam, 3D and front views

Fig. 3-44 and Fig. 3-45 clearly exhibit that thick flanges lead to a better stress redistribution. Indeed, the thick flanged beam leads to a plateau value of 0.11 MPa, as opposed to 0.13 MPa for the skinny flanged. Also, peak stresses on the transverse stress distributions are more distant on the first beam than on the second, implying a wider plateau, i.e. better loads redistribution. Therefore, even though their dimensions are unrealistic in practice, it can nevertheless be

concluded that Euler-Bernoulli beam theory has its limits and that its validity holds in a finite range of beams.

Still, *3.4.2.1. Significance of the flanges' thickness to efficiently redistribute stresses* showed that the assumption held true with a relative error less than 10%, for beams whose dimensions are in the order of magnitude of Liebherr crawler. Amongst the beams that have been tested in this study, wide beams with a shell thickness over 350 mm might be considered extreme. Therefore, the better load redistribution observed with these beams could be accounted for their wide flanges rather than for their thick webs or high stiffness, but the frame of this study does not provide enough material to conclude. Further work is required to determine the importance of flanges over stiffness and at which point one starts to be significantly prevailing over the other.

4. Comparison of numerical results with analytical predictions

4.1. Objectives, method and assumptions' overview

The entirety of what the study has exposed so far was modeled in Abaqus. The comparison of all the beams with changing shell thicknesses, with the close to rigid 0.5 m thick shell beam, were also carried out in Abaqus. In the end, they remain comparisons of simulations with simulations that were all done with the same model. Even though the results are interesting and relevant, it is hard in these conditions to extrapolate the work done out of this study and to extract out concrete results.

Again, it is classically assumed in the industry that stress distributions beneath the timber mats are uniform. This presumes that the crawler and mats are rigid. In this chapter, stress distributions that were simulated numerically with Abaqus will be compared with stress distributions obtained analytically by means of three assumptions: 1) rigid crawler and flexible mat, 2) rigid crawler and rigid mat, which is close to the assumption made by our industry collaborator PCL, and 3) rigid crawler and "semi-flexible" mat, which will be explained in due time. The crawler is assumed to be rigid in all cases. Even though it is idealistic and that the reality might say otherwise, *3.3.3.3.Quantification of the increase or decrease of stresses as a function of soil type and crawler stiffness* showed that such an assumption did not lead to dramatically different stress distributions, and that the relative error for a crawler like Liebherr's was comprised between 10 and 20% depending on the soil type.

This section aims to show the following. If the results obtained with Abaqus are valid, then the two first assumptions are too and not conservative. The remaining assumption gives good results and based on its realism, it supports the numerical results' validity obtained with Abaqus.

The stress distribution between the mats and the crawler was also discussed; it was shown that the assumption of crawler rigid body is conservative for the mat, and that the latter does not pose any problems regarding the system's integrity.

As stated above, each of the three assumptions was challenged with the stress distributions derived from Abaqus. In other words, the numerical simulations, and nothing else, will judge their workability.

4.2. Results

4.2.1. Stress distribution beneath the timber mats

4.2.1.1. Flexible mat assumption, description and results

The first assumption consists of considering that the loads are transmitted straight down from the crawler to the soil. The area taken into consideration in the stresses calculation is the area of contact between the mat and the crawler, i.e. 1.5 m x 11.9 m (Fig. 4-1).
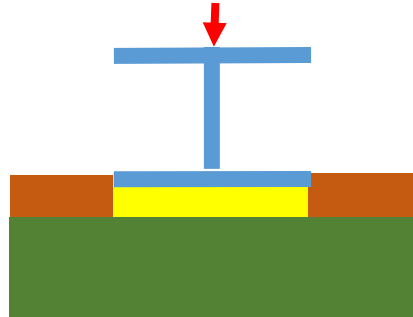
Fig. 4-1: Width of mat considered in the flexible mat assumption (yellow)

Everything happens as if the mat were absent. As a result, the stresses beneath the mat are calculated as follows:

$$\sigma_{flexible\ mats} = \frac{(2*2.5\ (load)+1\ (crawler)+0.18\ (mats))e6}{A_{crawler}} = 0.34\ \text{MPa}$$

The load carried by the soil is the sum of the two point loads on the crawler, of the crawler's mass and of the timber mat's mass. Fig. 4-2 puts the value obtained in perspective with the highest stress distribution obtained in the forty simulations done through the establishment of Chapter 3, i.e. the configuration of soil and crawler thickness which redistributes loads with the least efficiency: Sand & Gravel (most rigid soil) with a 75 mm thick shell beam (smallest beam).

Fig. 4-2 ignores peak stresses. It shows that the assumption of flexible mat leads to a uniform stress distribution that is much higher than the stress distribution obtained numerically. Again, the stress distribution displayed in Fig. 4-2 is the least favorable of all, and a shell thickness of 75 mm is not achieved in practice for such big load cases. Comparatively, the plateau value with the use of Liebherr crawler is as low as 0.16 MPa (Fig. 3-33), which is less than half the analytical value. The conclusion was predictable from the outset; the assumption of flexible mat is conservative and not realistic.

Fig. 4-2: Superimposition of a uniform stress distribution of 0.34 MPa
and the stress distribution generated by a 75 mm thick shell beam on
Sand & Gravel soil

4.2.1.2. Rigid mat assumption – made by the manufacturer, description and results

The second assumption looks at the mat as a rigid body. Everything happens as if the stresses coming from the crawler were entirely and uniformly diffused in the volume of the mat. As a result, the area of mat taken into account in the calculation of the stress distribution is the area of contact between the layer of timber mats and the soil, i.e. 6.096 m x 12.192 m.
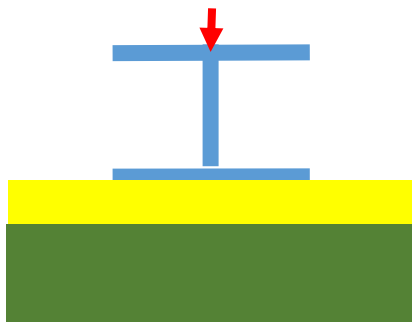
Fig. 4-3: Area of mat considered in the rigid mat assumption (yellow)

$$\sigma_{rigid\ mats} = \frac{(2*2.5\ (load)+1\ (crawler)+0.18\ (mats))e6}{A_{mat}} = 0.083\ \text{MPa}$$

57

A stress value about four times less than the previous assumption's is obtained; the method that our industry collaborator PCL uses in the calculation of the uniformly distributed stress leads to a value of 0.087 MPa, ever so slightly higher, which implies that their model regards the mats as rigid.

Fig. 4-5 demonstrates the non-conservativeness of that assumption. It superimposes the uniformly distributed stress of 0.087 MPa calculated by our industry collaborator PCL, with the lowest stress distribution derived numerically with Abaqus, i.e. the configuration of soil and crawler's stiffness which redistributes loads the most efficiently: Sand Fill (softest soil) with a 0.5 m thick shell beam (biggest beam).

It shows that the uniform stress predicts a lower stress distribution than that obtained with an unrealistically big I-beam. It means that the forty configurations that were tested in Chapter 3 lead to stress distributions that are all above the uniformly distributed stress plotted here. The assumption that the mats and crawler and rigid, therefore not only fails to predict accurately the stress distribution beneath the mats, but is also utterly non-conservative.

In particular, it might be interesting to take a closer look at the stress distribution generated by Liebherr crawler. Fig. 4-6 is a plot of the stresses collected along the main longitudinal path as described in Chapter 2 (Fig. 4-4) for Liebherr crawler, and the uniform stress distribution calculated with the second assumption, on Sand Fill soil.
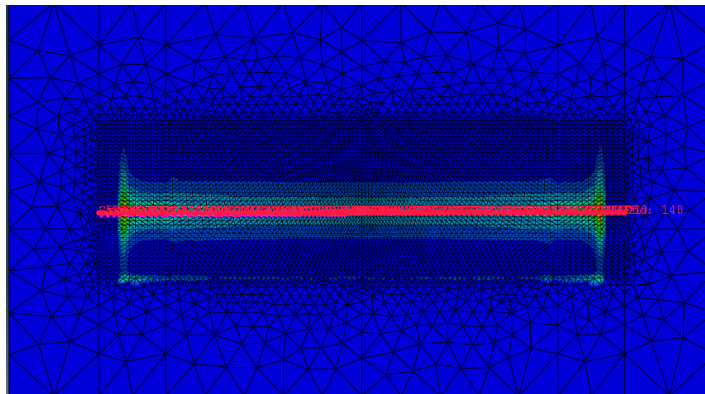
Fig. 4-4: Normal stress contour plots beneath the mats and
main longitudinal path in red
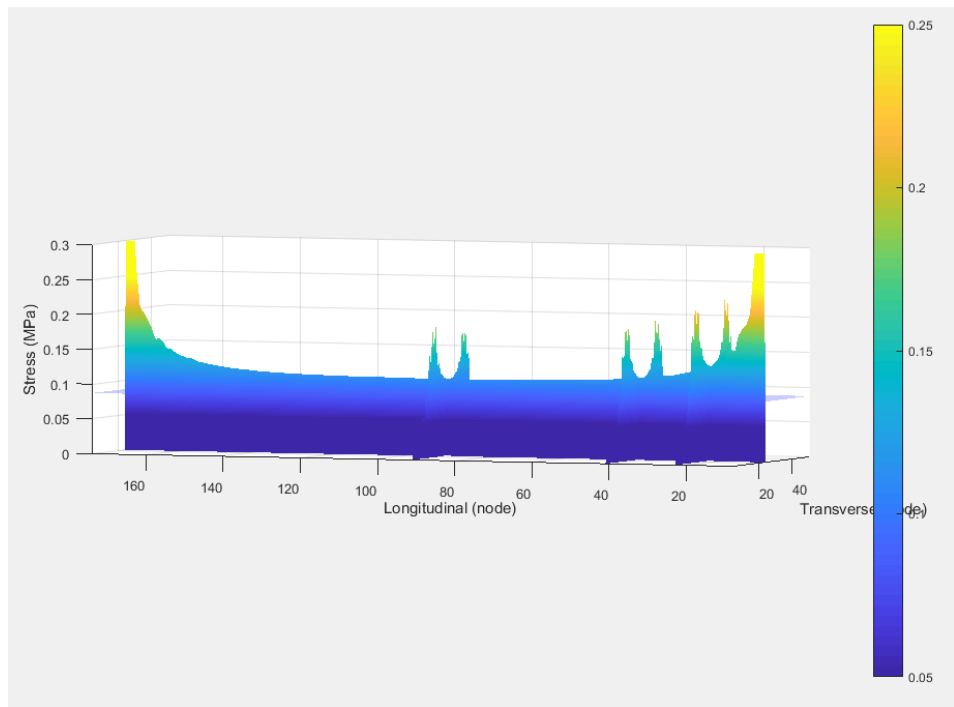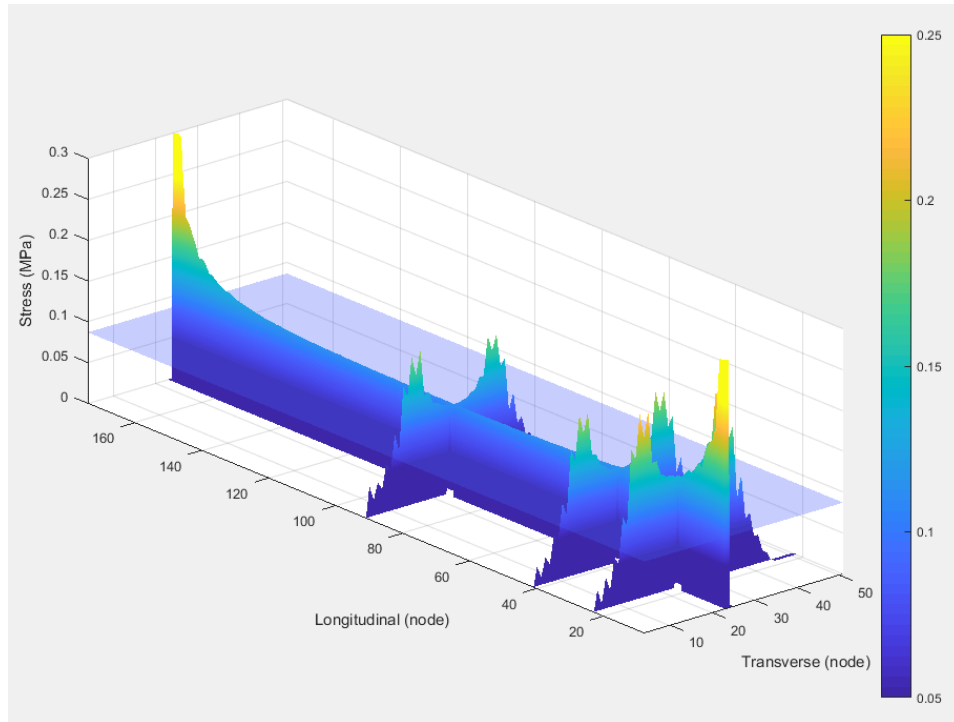
Fig. 4-5: Superimposition of a uniform stress of 0.087 MPa and the stress distribution generated by a 0.5 m thick shell beam on Sand Fill soil
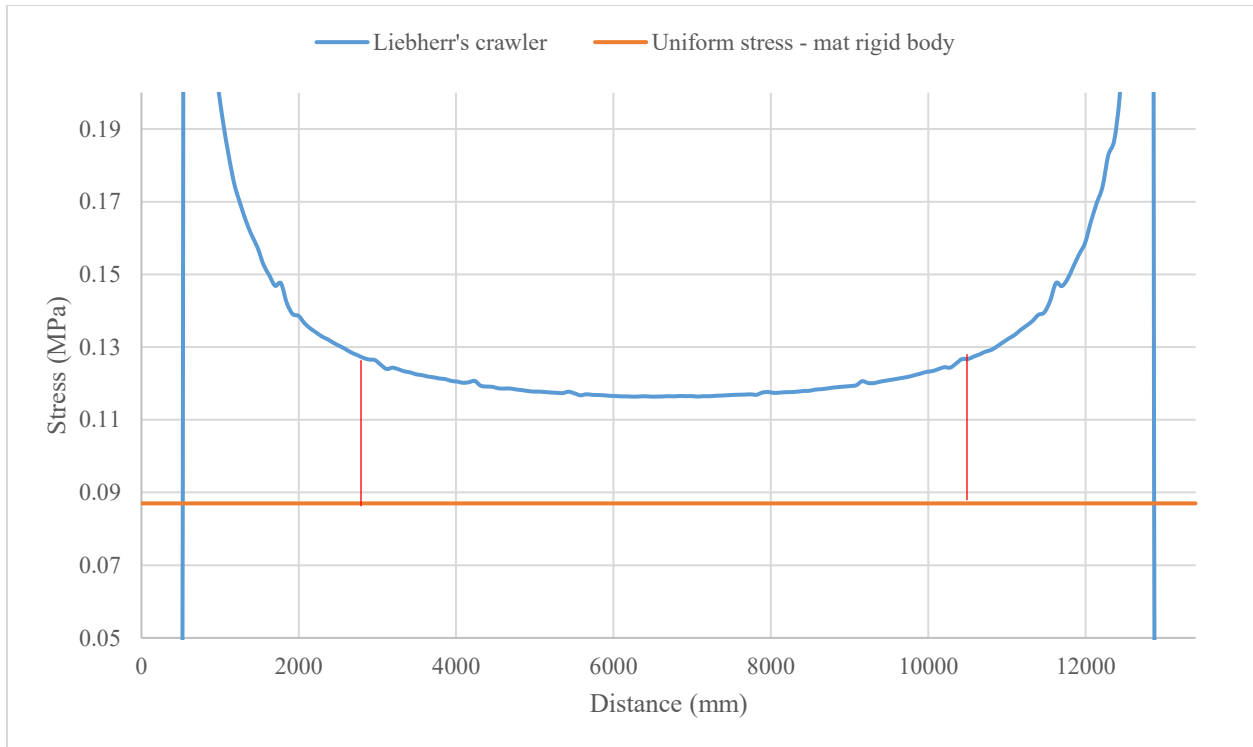
Fig. 4-6: Uniform stress of 0.087 MPa and stress distribution generated by Liebherr crawler on Sand Fill soil

The averaged relative error in stress between the two distributions was calculated in the plateau area, which was thought to be more relevant than the locations close to peak stresses:

$$\varepsilon_{relative} = 37\%$$

This error means that viewing the mat as a rigid body underestimates the stresses experienced by the soil by 37% on average on the main longitudinal path. Besides, that path corresponds to the minimum reached by the bowl; the error would therefore be higher away from the main path, i.e. towards the crawler's edges. As a result, an error of 37% is a bottom bracket of the actual relative error that would be computed on the whole area beneath the mat.

Fig. 4-7 is a plot on Matlab that shows the superposition of the stress distributions beneath the mat obtained with Abaqus when 1) the mat and crawler are modeled as rigid bodies, on Sand Fill, and 2) the configuration used in Fig. 4-5, i.e. a 0.5 m thick shell, non-rigid mat, on Sand Fill. Although the yellow peaks on three edges were expected, it can be noted that there's no peak stress on the side that is far from the crawler (northern edge on Fig. 3-7), most likely because the mat is lifted off due the applied bending.

60
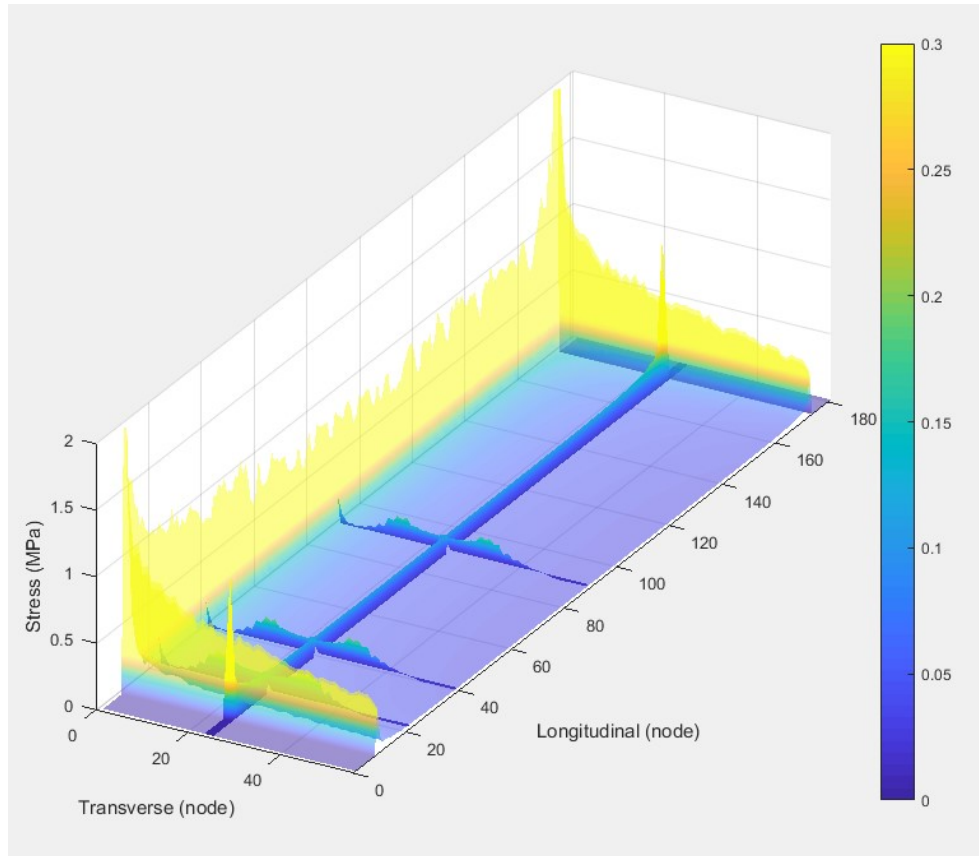
Fig. 4-7: Superimposition on Matlab of the stress distributions beneath the mat with 1) {mat + crawler} = rigid body on Sand Fill (transparent), and 2) a 0.5 m thick shell beam, non-rigid mat, on Sand Fill (the flattest stress distribution obtained in the study).

Fig. 4-8 represents a zoom in the blue area in Fig. 4-7. It conspicuously demonstrates that the assumption of uniformly distributed load is not correct directly underneath the mat, even for rigid surfaces. Furthermore, given that a 0.5 m thick shell can be considered rigid, based on Fig. 3-39, the sole different between the two distributions is the assumption on the mat, and thereby Fig. 4-8 also shows that the mats are not rigid.
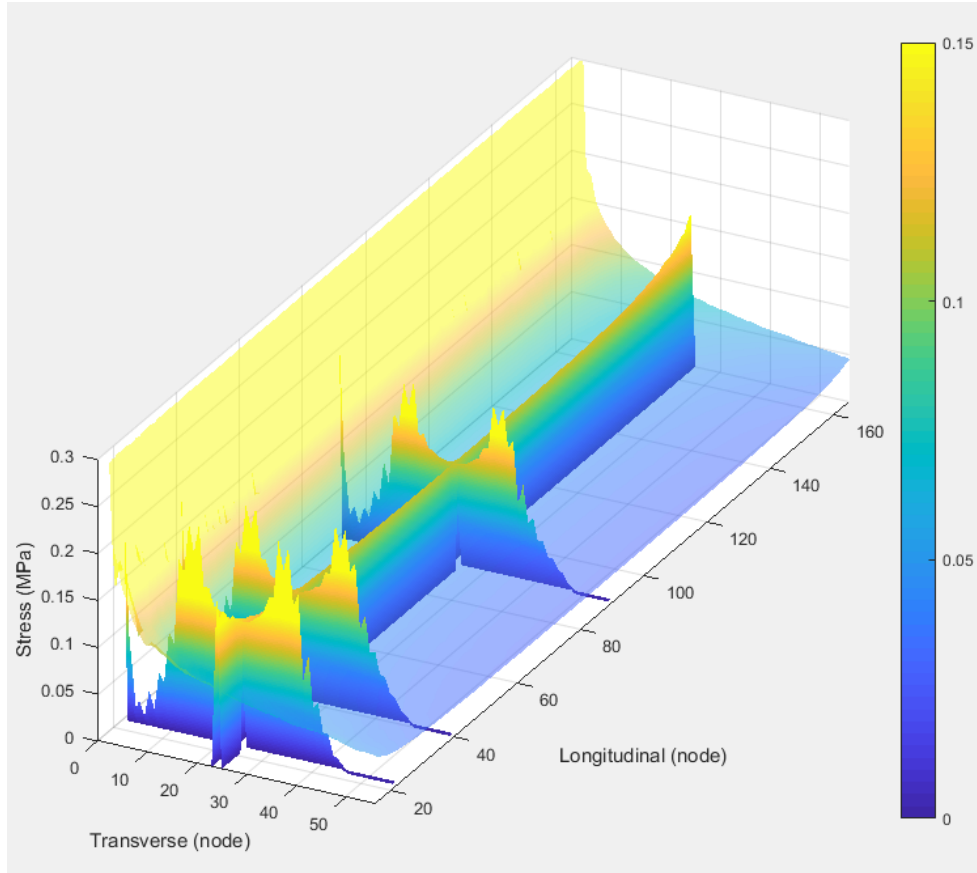
Fig. 4-8: Zoom-in of Fig. 4-7

4.2.1.3. Semi-flexible assumption, description and results

The two preceding assumptions both lead to unacceptable stress values, either too high and too conservative, or too low and non-conservative. This section addresses the third assumption, which was thought during the study of the two first assumptions. It takes root in a realistic idea and conducts to good predictions, leading to a uniform stress that matches the numerical stress distributions. It reposes on the idea that stresses make their way through the mat with an angle of 45°, as pictured in Fig. 4-9.

This configuration widens the contact area's width taken into account in the calculation of stresses beneath the mat:

$$\sigma_{45°} = \frac{(2*2.5\ (load)+1\ (crawler)+0.18\ (mats))e6}{A_{45°}} = 0.24 \text{ MPa}$$
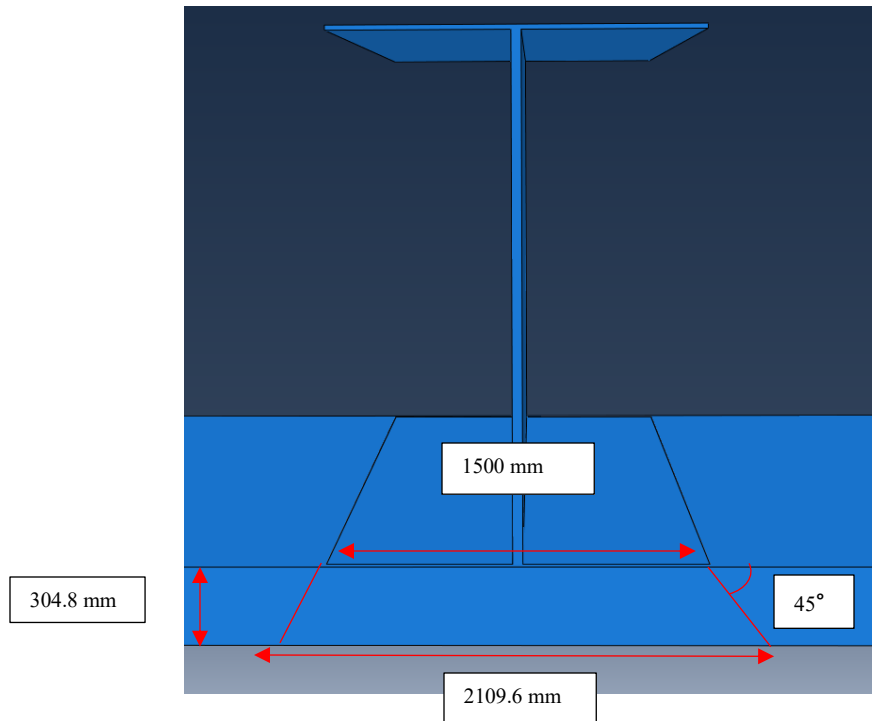
Fig. 4-9: Third assumption pictured with the 45°angle and the width of
mat considered in the calculation of stresses

Fig. 4-11 shows Matlab plots of a uniform stress distribution of 0.24 MPa, along with the
stress distribution obtained with Liebherr's crawler, for the four soil types.

These plots demonstrate that the assumption that lead to a uniform stress of 0.24 MPa is
reasonably conservative in the case of the use of Liebherr's crawler, although plasticity has to be
taken into account, in which case peak stresses might be chopped off, conducing to an overall
increase in the stress distributions. Still, however, it is thought that they would remain below the
analytical stress distribution.

As seen in *3.3.1. Effects of crawler stiffness on stress distributions*, stresses are less
uniformly distributed when the crawler's stiffness is low. In particular, the stress distributions of
a 0.1 m thick shell beam are illustrated in Fig. 4-12, superimposed with the uniform stress of 0.24
MPa. Fig. 4-12 shows that the stiffest soils Clay Till and Sand & Gravel are about the same level
as the uniform stresses, which makes the assumption non-conservative for these soils. Thinner
beams in general are prone to fail to correctly redistribute loads on the mat and therefore should
be avoided when dealing with significant loads.

These plots point out a detail of prime importance. It has been explicitly exhibited throughout the numerical simulations that stress distributions were greatly affected in shapes and intensities by the soils' elastic parameters. The methods used to calculate the stress distributions beneath the mat in the industry, however, and in particular the method used by PCL, do not take into account the nature of soils.

4.2.2. Stress distribution between the crawler and timber mats

This study has hardly tackled the stress distributions between the mat and the crawler. It has mainly focused on the situation beneath the mat, as the soil is, comparatively to the mat, much more eager to be an issue for the system as a whole given its ductility and non-uniformity, and therefore lead to local and global failures. Like 3.2.1, in this section are to be compared the stress distributions obtained with Abaqus with analytical calculations. The analysis was rather short and superficial as the stresses experienced by the mats are not likely to threaten the system's integrity.

4.2.2.1. Assumption made by the manufacturer

The construction industry classically assumes that stresses between the mat and the crawler are uniform. This study specifically tested Liebherr crawler, which was considered sufficiently telling not to have to carry out further investigations. Fig. 4-10 shows the normal contour plot on the surface of the mat. The stresses were collected along all the paths comprising the area encompassed by the red rectangle and plotted on Matlab.
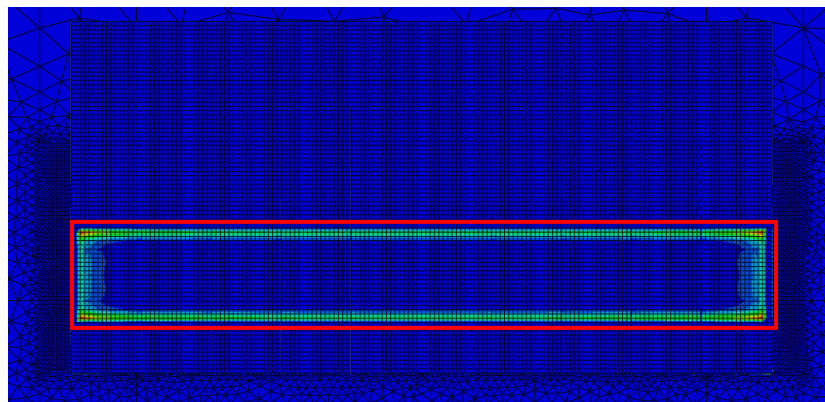
Fig. 4-10: Normal stress contour plot between the mat and the crawler, with the area of interest circled in red
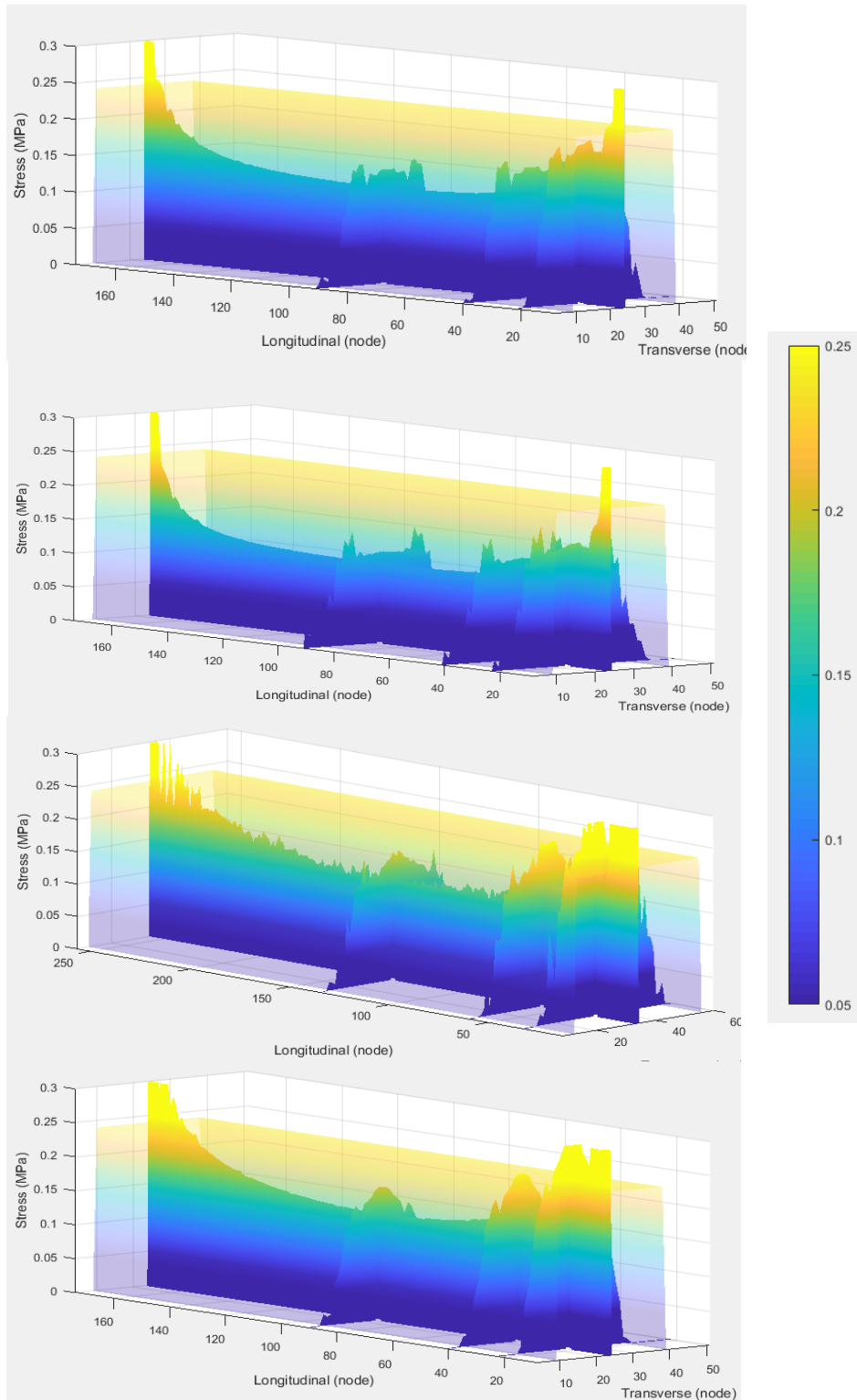
Fig. 4-11: Superimposition of a uniform stress of 0.24 MPa and the stress distributions generated by Liebherr's crawler on (from top to bottom): Sand Fill, Native Sand, Clay Till and Sand & Gravel
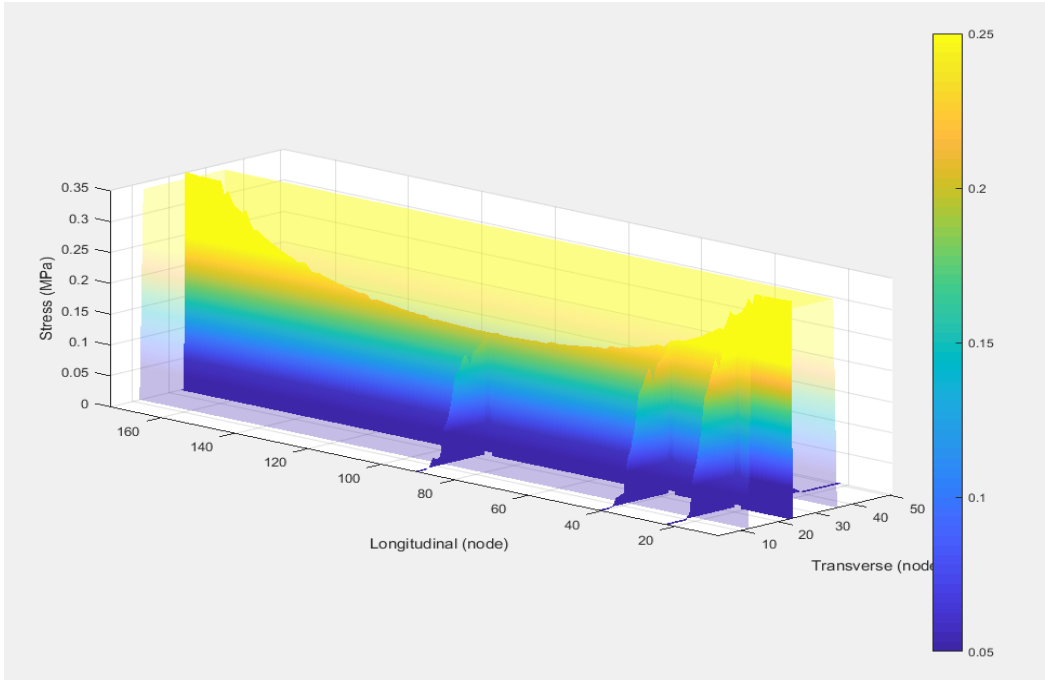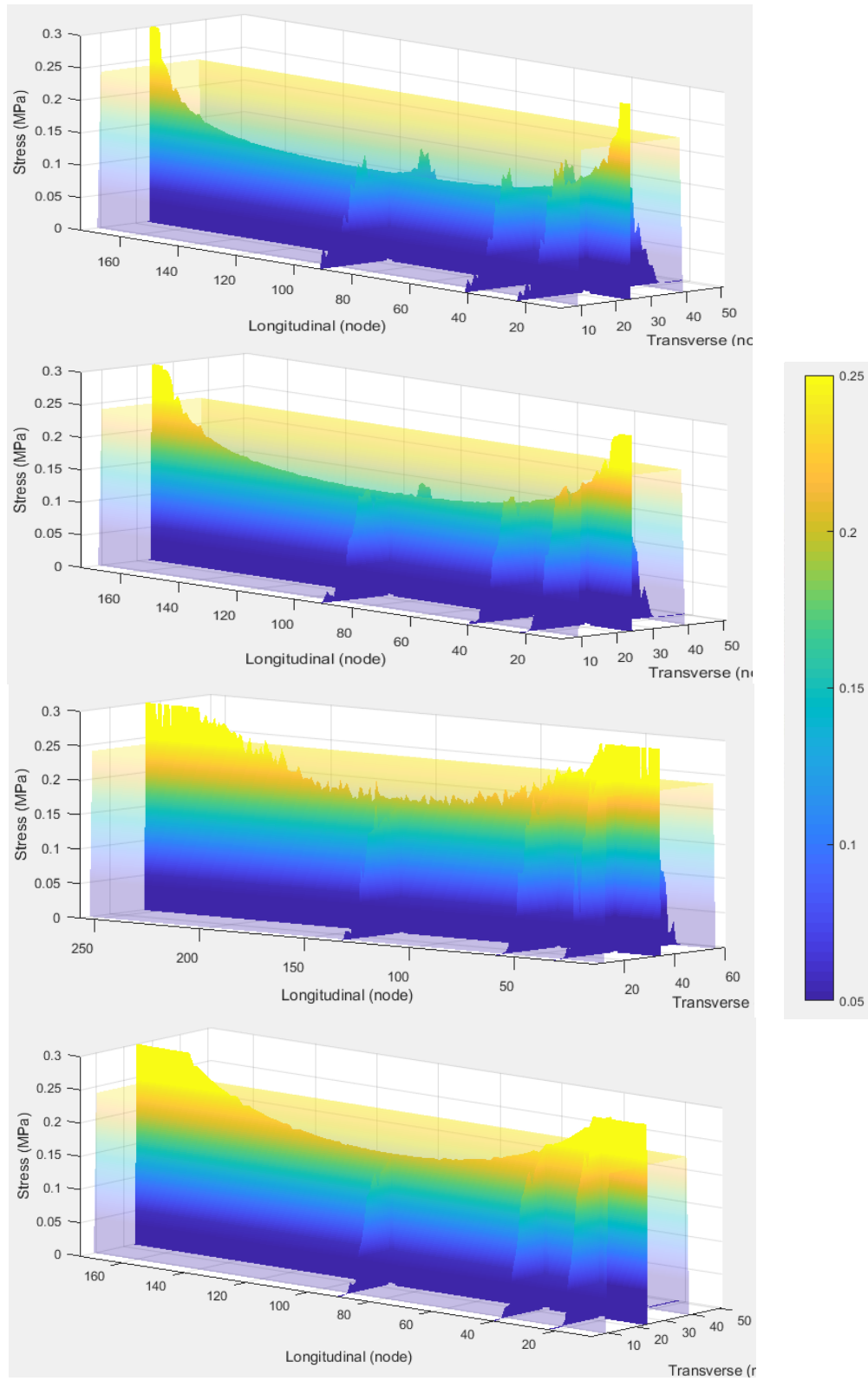
Fig. 4-12: Superimposition of a uniform stress of 0.24 MPa and the stress distributions generated by a 0.1 m thick shell beam on (from top to bottom): Sand Fill, Native Sand, Clay Till and Sand & Gravel

66

4.2.2.2. Results and conservativeness of the assumption

Fig. 4-13 pictures the 3D stress plot between the mat and the crawler obtained with Matlab. High stress values are noticeable on the area directly beneath the crawler's ends and edges, as per the peak stress theory discussed in *3.2. Shape of the stress distribution beneath the timber mats and peak stresses*. These high values are misleading and hide the stress distribution shaping the bulk of the area beneath the crawler. Fig. 4-14 displays the hidden part of the stress distribution once these peak stresses are trimmed.
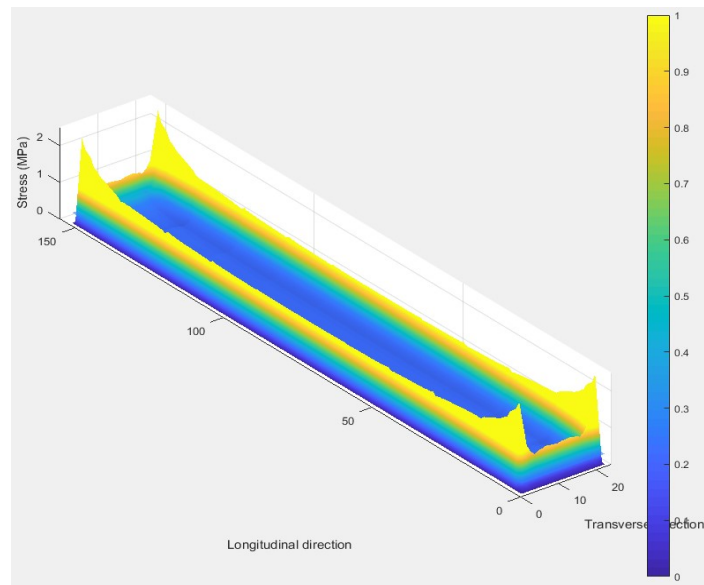
Fig. 4-13: 3D stress distribution between the mat and the crawler generated by
Liebherr crawler
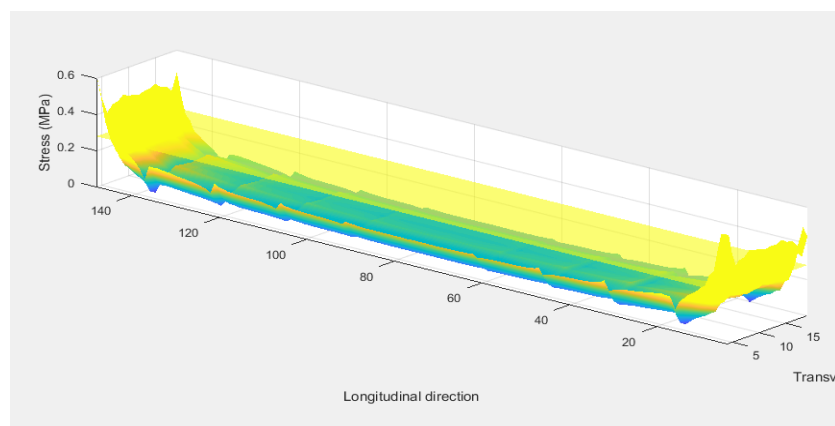
Fig. 4-14: Stress distribution between the mat and the crawler after having cut off
high stress values beneath the crawlers' ends

The transparent yellow plateau is the uniform stress distribution calculated by our industry collaborator PCL:

$$\sigma_{mats} = 0.33 \; MPa$$

Fig. 4-14 brings out the much higher position of the uniform stress with respect to the stress distribution in the inner area, which is akin to a plateau, and therefore puts the design on the conservative side. The peak stresses on the mat's edges, nevertheless, are three times as high as the analytical stress, as shown in Fig. 3-13. The peak stresses at the corner of the mat are up to four times as high as the calculated stress. In practice though, mats are not positioned as perfectly and uniformly as in the model, and peak stresses are therefore likely to be alleviated and not to cause major damage to the mats. If damages there are, they would anyway be very localized.
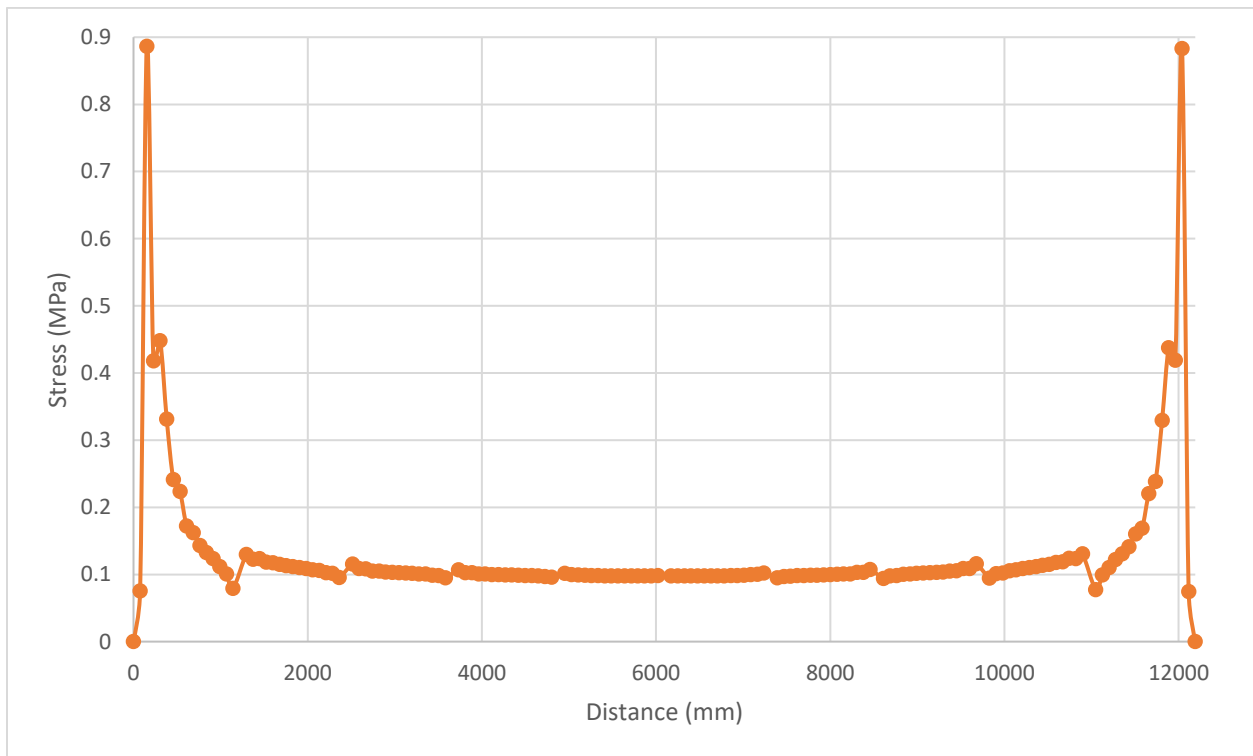
Fig. 4-15: Stress distribution on mat's main longitudinal path

5. Timber mats design methodology

5.1. Objectives

This work was done as part of an internship with PCL Industrial Management Inc. under the supervision of Rick Hermann and Travis Zubick. I carried out a research project whose topic is in the continuity of this paper. The scope of the research was to develop new equations for the load distribution beneath timber generated by a crawler crane, for various types of soil. In accordance with the current method, the load distribution is assumed to be uniform under a calculated effective bearing area. Based on the work which has been done in this thesis, this assumption is not an accurate representation of the actual loading. For the calculation methodology to be more representative of the actual loading conditions, equations had to be derived following the results of the finite element analysis for multiple soil types.

The objective was to use finite element analysis to calculate the shape and magnitude of the shear and bending moment diagrams in the mats, as well as the pressure distribution beneath the timber mats. These stresses would determine a more accurate effective bearing area than current methods which assume a uniformly distributed load being applied to the mat.

Soil bearing failure was also investigated, for multiple soil types, with failure defined as differential settlement of more than 0.5% along the crawler's track as this may occur before the structure of the timber mat fails.

5.2. Model description

4.2.1. Model and meshing

The model used in Abaqus was like that of *1. Model description,* however honed and optimized. Conversely to the model used in *3.Development of a Finite Element Model with ABAQUS* and *4.Comparison of numerical results with analytical predictions*, only half the system is modeled. The cranes investigated are the LR1600 and LR1400, both manufactured by Liebherr. These cranes are similar to the LR1750 presented at the beginning of this paper but are designed to carry a lighter maximum load. Six models were tested in the case of LR1600, on five different soil types, when one model was tested for LR1400, on five soil types. These models are illustrated in Fig. 5-1, wherein part of the soil has been cut for layout purposes; the soil types' mechanical parameters are displayed in Table 5-2. The models tested correspond to solutions that are typically chosen by engineers at PCL to lower the soil's bearing pressure and the mats' stresses in shear and

bending when one layer of mat does not suffice to ensure the system's safety. These solutions are as follows:

Fig. 5-1-a: basic configuration already studied in this thesis;

Fig. 5-1-b: a second layer of mats is inserted between under the first layer, parallel to the first layer

Fig. 5-1-c: a 6 inches (15 cm) layer of gravel is inserted between the mats and the soil;

Fig. 5-1-d: an 18 inches (45 cm) layer of gravel is inserted between the mats and the soil;

Fig. 5-1-e: a 6 inches layer of gravel is inserted between the second layer of mats and the soil;

Fig. 4-1-f: 12 inches of gravel are added to the 6 inches, which makes 18 inches of gravel
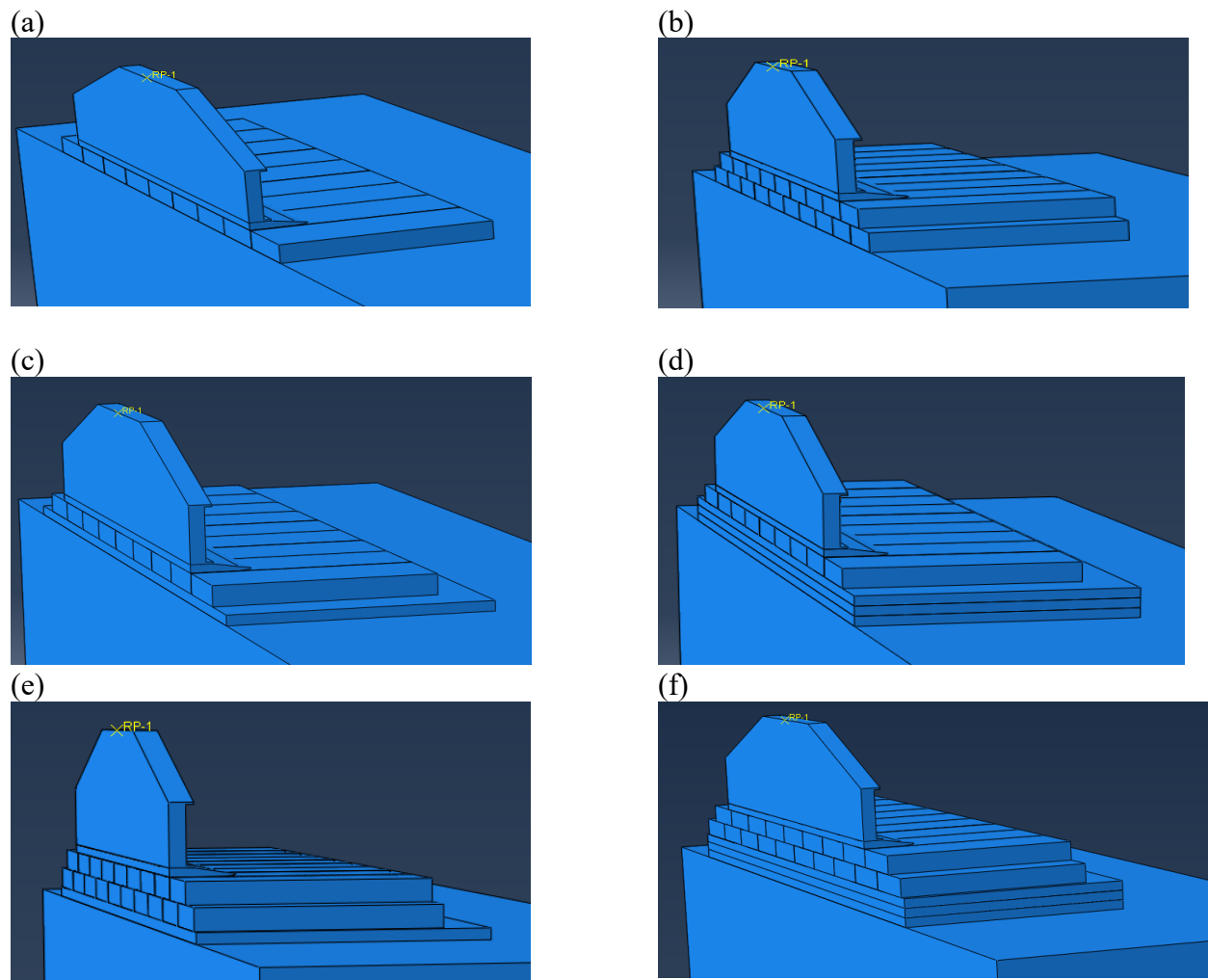
Fig. 5-1: Configurations of solutions proposed by PCL to reduce the soil bearing pressure and the stresses in the mats

It is worth mentioning that the track is positioned right off one mat's edges, at the exact same point for all cases. Indeed, *3.Development of a Finite Element Model with ABAQUS* showed

that stress peaks occur beneath objects' ends. As such, placing the track nearly on a mat's edge would lead to the least favourable configuration of such a mat, as well as for the soil below.

The boundary conditions are kept unchanged; as a recall, the soil's bottom is fixed along the three directions, and its sides cannot move sideways. A symmetry, however, was added in the X direction. The areas concerned by that symmetry are highlighted in red in Fig. 5-2. The I-beam used in the previous parts was replaced by a beam-crawler ensemble. The LR1600 beam-crawler's dimensions are as follows: L=8.7m, W=0.67m, w = 0.35, h_1=0.98m at the ends and h_2=1.6m in the middle; the LR1400 beam-crawler's dimensions are: L=7.8m, w=1.04m, h_1=0.98m at the ends and h_2=1.6m in the middle. They were both modeled as rigid bodies.

Gravity was included in the model. Six crane load scenarios were tested for both cranes on all the soil types and all the models. The load cases on the beam consist of percentages of the crane's maximum capacity that were converted into two linearly distributed values of pressure P'1 and P'2 at either end of the track (Fig. 5-4), extracted from Liccon, the software provided by Liebherr and used by PCL engineers, under specific cranes configurations that are customarily met in practice. These configurations are functions of the radius of the boom, the load's weight, the counterweight, and the angle made by the superstructure with the carbody. A technical difficulty appeared when it was realized that the P1 and P2 provided by Liccon are located *beneath* the crane's track, as shown in Fig. 5-5, when the model used in Abaqus has pressure input on *top* of the beam, that lays on the track.
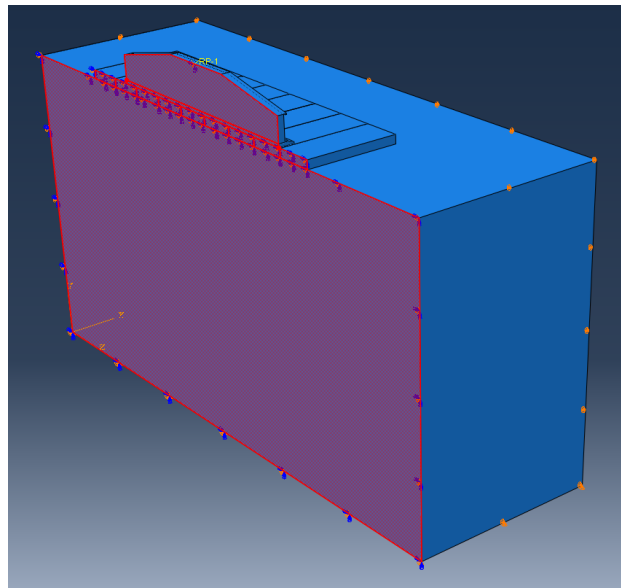
Fig. 5-2: Areas affected by the planar symmetry
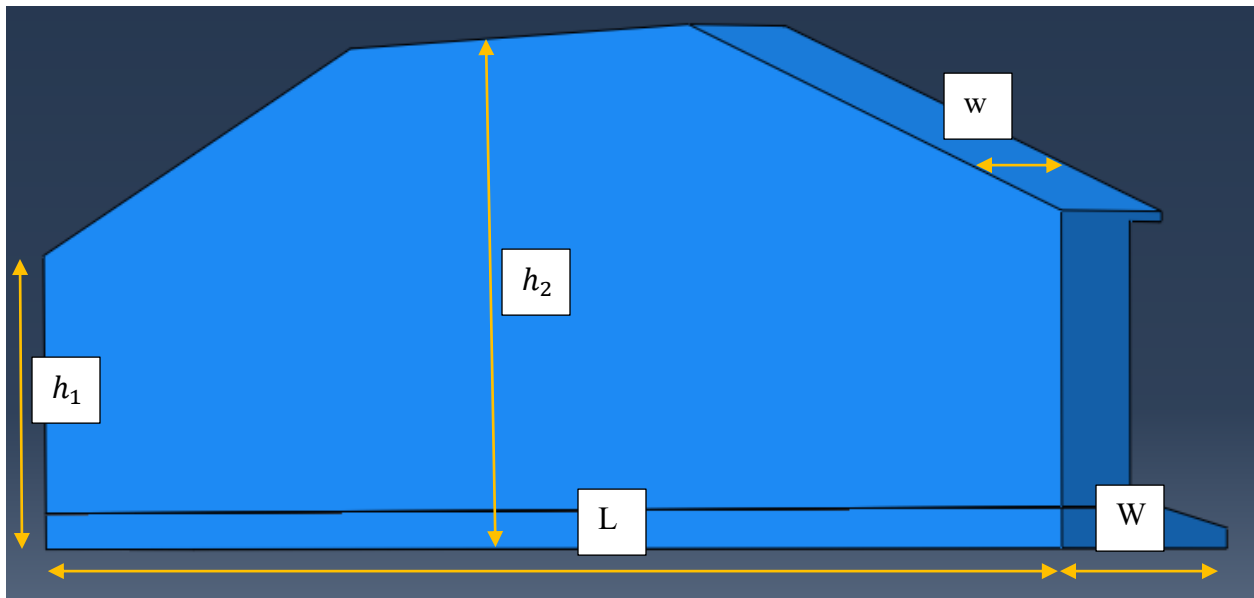
Fig. 5-3: Notation for the crawler and beam's dimensions
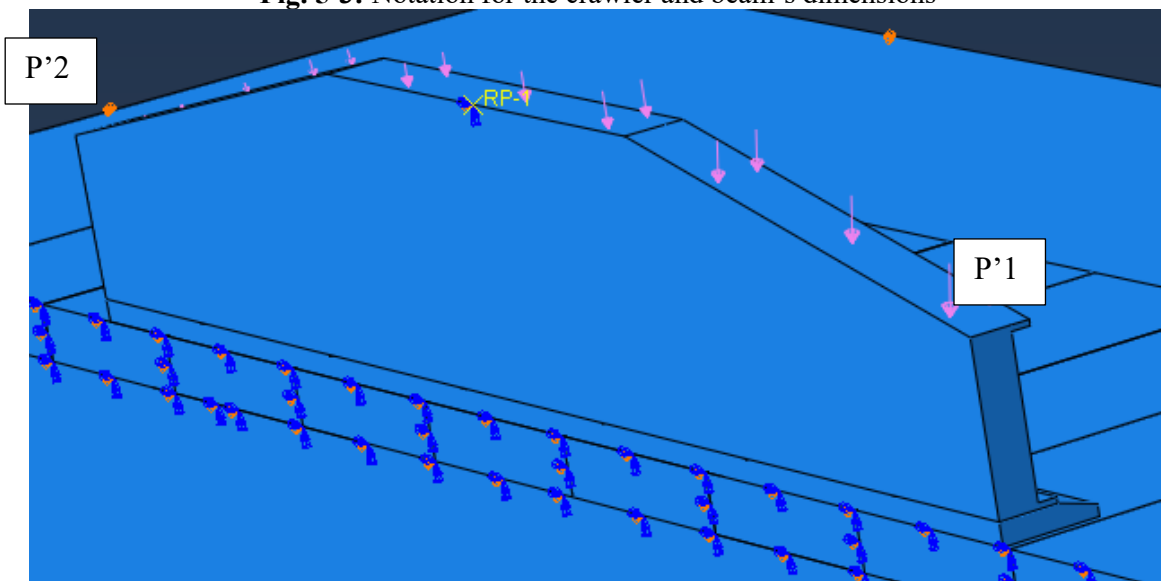
Fig. 5-4: Distributed pressure on the beam, from P2 to P1

These configurations are functions of the radius of the boom, the load's weight, the counterweight, and the angle made by the superstructure with the carbody. A technical difficulty appeared when it was realized that the P1 and P2 provided by Liccon are located *beneath* the crane's track, as shown in Fig. 5-5, when the model used in Abaqus has pressure input on *top* of the beam, that lays on the track.
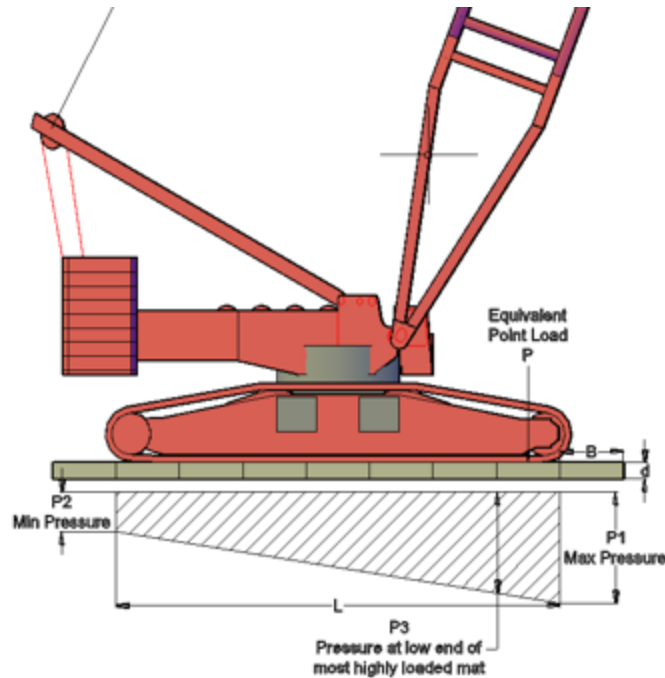
Fig. 5-5: Notation given for the pressure under the track

Pressure is linearly distributed between P1 and P2. A conversion needed to be carried out to keep consistent results, as shown by the equation that follows:

$$P_{top\ beam} = P_{beneath\ track} * \frac{Track's\ width}{Beam's\ width} * Conversion_{psi \to kPa} - Weight_{track+beam}$$

Besides P1 and P2, a pressure P3 was defined, as introduced in Fig. 5-5, as well as a pressure P, defined as the average of P1 and P3. On top of the beam, P'3 was defined as the value of pressure located at a mat's width away from P'1, and the average of P'1 and P'3 was called P'. Table 5-1 and Table 5-2 summarize the load cases and soil types tested for both cranes. Table 5-1 and Table 5-2 display the track's width W and the effective track's length activated during loading, the later varying for LR1400, for not equipped with a counterweight, and thereby tilting forward when P1 reaches higher values. This phenomenon is entirely controlled by engineers. Furthermore, two configurations show a negative P2, which is balanced out to zero when the crawler's weight is considered during simulations. The range 90-100% of the crane's maximum capacity is never used in practice. The mesh in the mat was designed much finer than that of *1.Model description*, as shown in Fig. 5-6: (a) mat, (b) soil, (c) gravel layer since one of the objectives was to determine the bending moment and shear force inside the mats. The mesh in the soil was also modified. The

73

gravel layer, as thick as 15 cm, was composed, like the mat and the soil, of C3D8R elements. The beam-crawler being modeled as rigid bodies, the quality of its mesh was of little importance.

Table 5-1: Values of pressures associated to every load case, both for LR1600 and LR1400

	Pressure from Liccon			Pressure after conversion					
LR1600	P1 (psi)	P2 (psi)	P3 (psi)	P'1 (kPa)	P'2 (kPa)	P'3 (kPa)	P'=(P'1+P'3)/2	L (m)	W (m)
9%	35	34	35	445	430	443	444	8.7	1.34
30%	66	20	60	900	225	805	853	8.7	1.34
45%	76	22	68	1046	254	935	990	8.7	1.34
60%	86	23	77	1193	269	1063	1128	8.7	1.34
75%	95	26	85	1325	313	1183	1254	8.7	1.34
90%	109	23	97	1530	269	1353	1442	8.7	1.34

	Pressure from Liccon			Pressure after conversion					
LR1400	P1 (psi)	P2 (psi)	P3 (psi)	P'1 (kPa)	P'2 (kPa)	P'3 (kPa)	P'=(P'1+P'3)/2	L (m)	W (m)
21%	33	32	33	320	308	318	319	7.8	1.04
30%	42	26	40	423	241	397	410	7.8	1.04
45%	57	15	51	593	115	526	559	7.8	1.04
60%	72	5	63	764	1.6	657	710	7.8	1.04
75%	92	0	79	992	-55	845	919	5.8	1.04
90%	120	0	103	1310	-55	1118	1214	4.9	1.04

Table 5-2: Values of the physical quantities for every soil type

	LR1600/LR1400					LR1600 only	LR1400 only
Soil type and condition	Compact Sand	Loose Gravel	Compact Gravel	Surmont Clay	Very stiff Clay	Aspen	Stiff Clay
E (Mpa)	40	55	90	40	75	94	50
v	0.3	0.3	0.3	0.48	0.48	0.35	0.48
Average Ground Bearing Pressure (MPa)	200	100	400	150	375	80	200
Density (kg/m^3)	1850	1850	2000	1650	1800	1835	1650
Ngamma factor	57	25	90	0	0	3	0
Phi (degree)	38	34	40	0	0	21	0

(a)

(b)

(c)
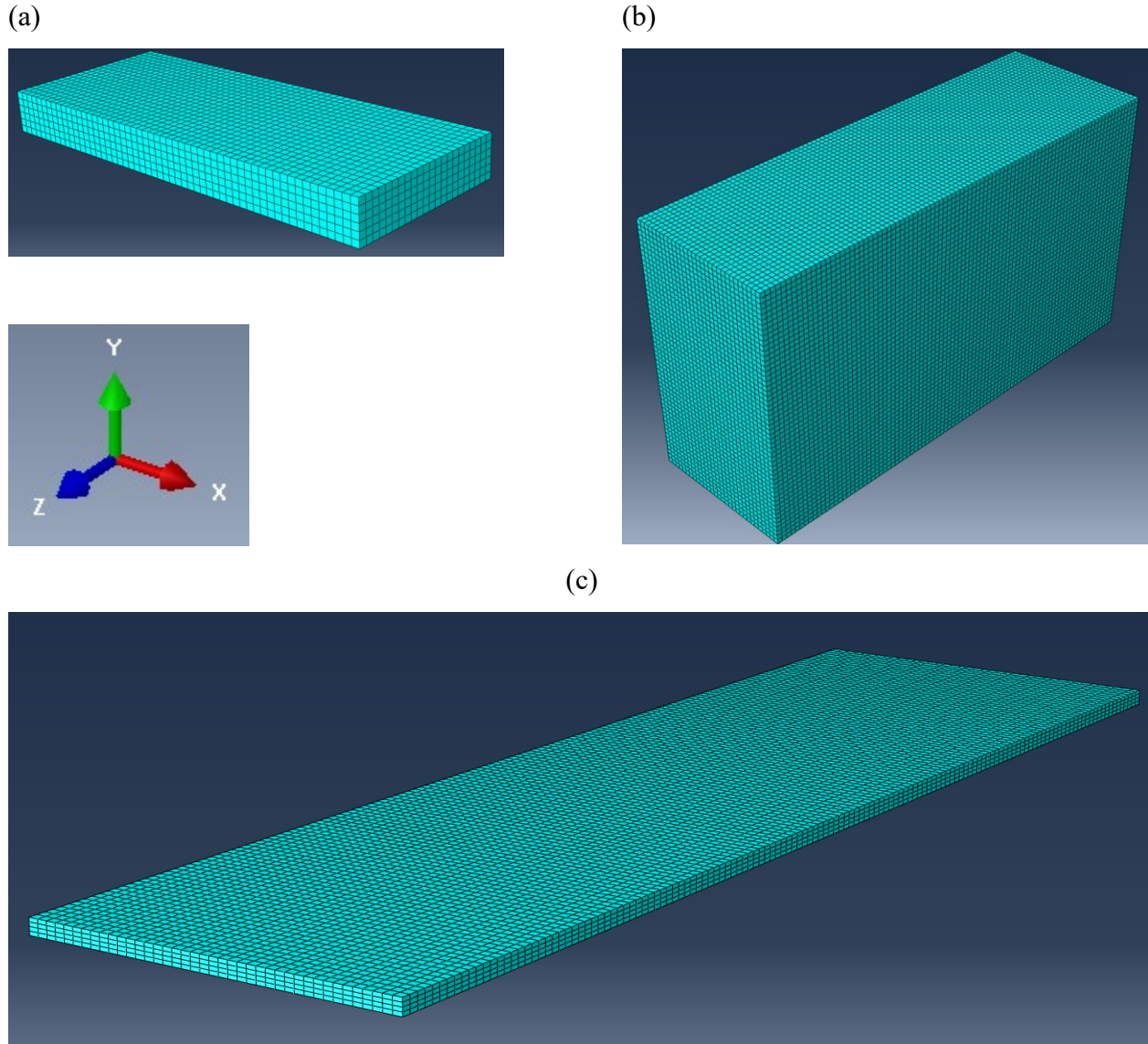
Fig. 5-6: (a) mat, (b) soil, (c) gravel layer

4.2.2. Method of data collection in the mat

Before getting into how data were collected, needs to be shown the spreadsheet PCL uses in its daily routine (Fig. 5-7):

PCL	Ground Bearing Pressure	
Project Name		
Project #		
Crane Model		
Load Name		
Timber Mats - First Layer		
Timber Mat Length	20	ft
Timber Mat Width (B)	4	ft
Timber Mat Depth (d)	1	ft
Timber Mat Weight (50lbs/ft³)	4,000	lbs
Crawler Track Width (w)	4.40	ft	Use short contact surface
Allowable Soil Bearing Capacity (q$_a$)	5,000	psf
P1 - Loading Under Crawler - Max	15,696	psf
P2 - Loading Under Crawler - Min	3,312	psf
Soil Loaded Length (L)	28.6	ft
P3 - Loading at Low End of Critical Mat	13,964	psf
P - Equivalent Point Load	261,008	lbs
Min. Mat Cantilever Distance (a$_{min}$)	4.43	ft
Allowable Mat Bending Stress (F$_b$)	196,800	psf	1200 psi per Duerr, D Fir Larch
Allowable Mat Shear Stress (F$_v$)	21,400	psf	170 psi per Duerr, D Fir Larch
Max. Mat Cantilever Distance - Bending (a$_b$)	3.34	ft
Max. Mat Cantilever Distance - Shear (a$_v$)		ft
Max. Mat Cantilever Distance - Deflection (a$_d$)		ft
Governing Mat Cantilever Distance	3.34	ft	Bending Governs
Effective Timber Mat Length "c"	11.07	ft
Applied Pressure to mat (q)	5,893	psf
Actual Bending Stress (f$_b$)	196,800	psf	Bending OK
Actual Shear Stress (f$_v$)	20,653	psf	Shear OK
Actual Deflection (Δ)	0.08	in
Actual Soil Loading Under Mat	5,983	psf	SOIL CAPACITY EXCEEDED
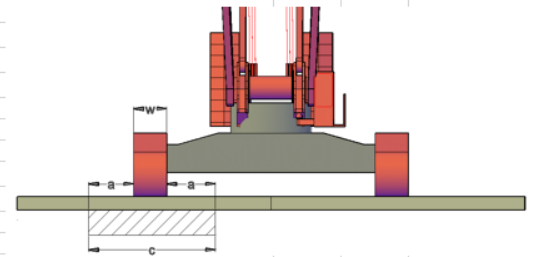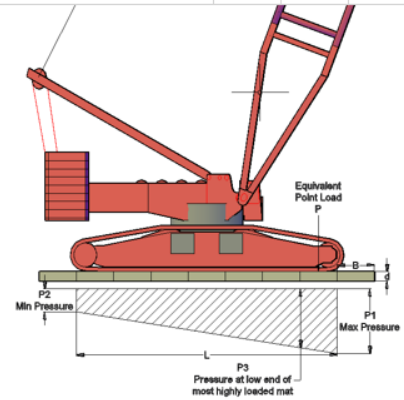
Fig. 5-7: Spreadsheet used by PCL in their daily routine

When the dimensions of the crane are chosen, P1 and P2 are to be input. Out of these are computed six important values: the effective timber mat length, the bending and shear stresses in the mat, the deflection, differential settlement and total load beneath the mat. The effective timber mat length "c" is the length of mat that is effectively activated during the loading. As the bending of the mat increases with the pressure exerted by the track, the length of contact between the mat and the soil is expected to decrease, which is equivalent to say that the length of mat activated decreases. As a result, "c" is expected to be a decreasing function of the loading. It would imply that the bigger the length of mat activated, the smaller the loading on the soil. This must be understood, as the solutions proposed by PCL aim at increasing "c" to diminish the loads carried by the soil.

$$Soil\ bearing\ pressure = \frac{Applied\ pressure\ to\ mat}{mat's\ width * c}$$

The physical quantities that are to be computed in the present work are the same as those sought by PCL, except that since the simulations on Abaqus are carried out in three dimensions,

the differential settlement between either end of the track is to be collected and used as a soil failure criterion.

Given that pressure on the beam is unevenly distributed, only the mat beneath the beam-crawler's end where pressure is maximum, i.e. the mat undertaking the highest loads, was investigated. To dress the diagrams of the mat's internal forces along its length, that are the bending moment and shear force diagrams, the normal stresses and shear stresses were collected at the nodes. In Abaqus, these physical quantities are named S11 and S12 (classically called σ_{xx} or σ_{11} and τ_{xy}, σ_{xy} or σ_{12} in the literature). Fig. 5-8 shows the path of collection.
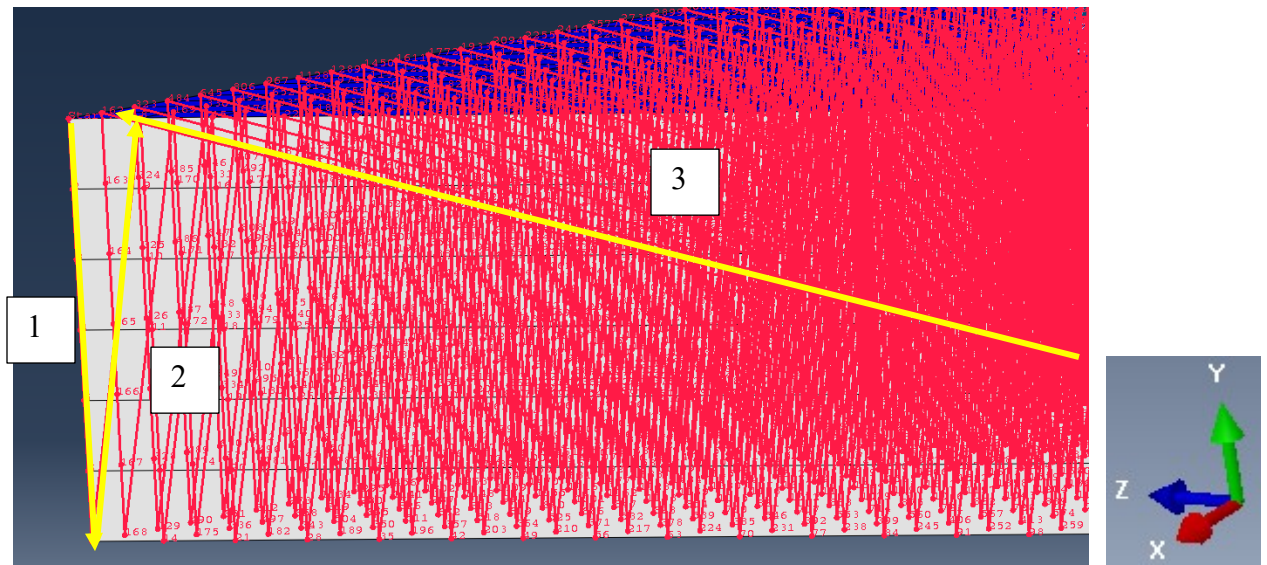
Fig. 5-8: Path of collection, all the mat's nodes are passed by methodically

The path starts at the mat's corner, crawls down its thickness ({1} in Fig. 5-8), comes back up the second column of nodes {2}, crawls down likewise, and so on and so forth until all the nodes of the first plane have all been collected. Once they have, the path rewinds back to the mat's corner {3} but shifted by one node in the mat's length direction (north east direction in Fig. 5-8). Amassing the nodes this way ensures to pass by them all in a methodological way that will allow easy integrations about every thickness of every plane. Indeed, the following expressions were to be used:

$$V = \iint -\tau_{xy}dX_y dX_z \qquad M = \iint -\sigma_{xx}X_y dX_y dX_z$$

Where V is the shear force, M is the bending moment along the mat's length; σ_{xx} and τ_{xy} have been defined above. To plot the shear diagram, the method was as follows: a) integrate the

shear stress values along the mat's thickness (in the Y direction, {1} in Fig. 5-8), b) sum these values to obtain a number homogeneous to a line force which corresponds to that very thickness, c) keep doing this for each thickness path ({2} in Fig. 5-8). This will give as many line forces as the number of discrete elements along the mat's width (in the Z direction); then d) integrate these numbers along the mat's width. This will provide one value of shear force. Reiterated ({3}) on every plane along the mat's length (in the X direction in Fig. 5-8), the shear force diagram can be plotted.

The process to plot the bending moment diagram is identical, except that every value of normal stress needs to be multiplied by the moment arm X_y with respect to the mat's thickness' center line in the Y direction, with the right sign, before being integrated.

4.2.3. Method of data collection on the soil

In a second phase had to be devised the soil bearing pressure beneath the mat that undergoes the highest loads. For that respect, the path shown in Fig. 5-9 was plotted on the soil and contact pressures CPress were collected at the nodes.
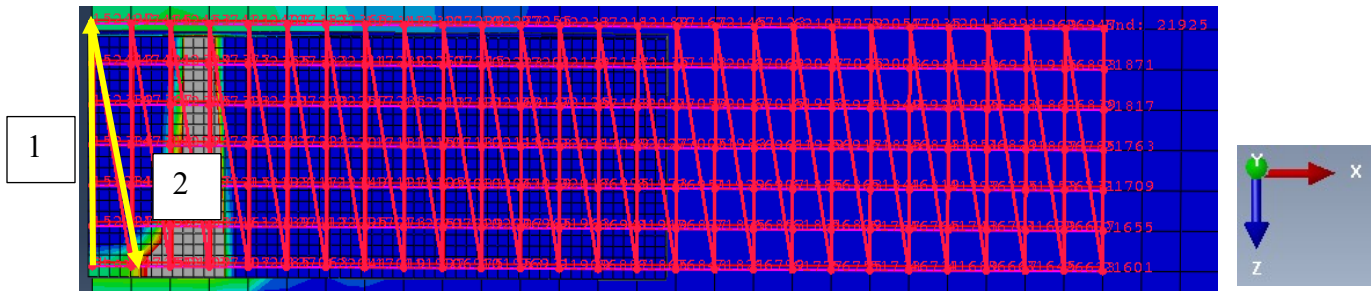
Fig. 5-9: Path of collection on the soil

Like the shear and bending moment, the path was traced to facilitate the integration of points along the mat's width, in accordance with the equation that follows:

$$Contact\ pressure = \frac{1}{mat's\ width} \int \sigma_{22} dX_3$$

The method consists of a) collecting contact pressure points starting from the bottom left corner of Fig. 5-9, up along the mat's width ({1} in Fig. 5-9), b) integrating these points along the mat's width, then c) running back to the node just on the initial node's right hand ({2} in Fig. 5-9), and so on and so forth. This would result in as many contact pressure points, homogeneous to a line force, as the number of discrete elements along the X direction, which would turn into contact

pressures homogeneous to a stress after averaging by the mat's width. Fig. 5-10 shows the path on the soil with a view in perspective.

(a)
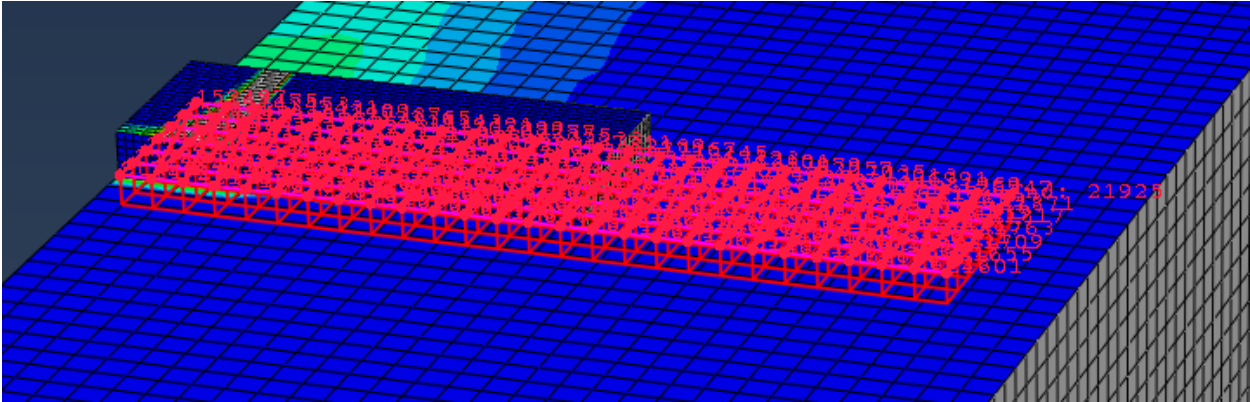
(b)
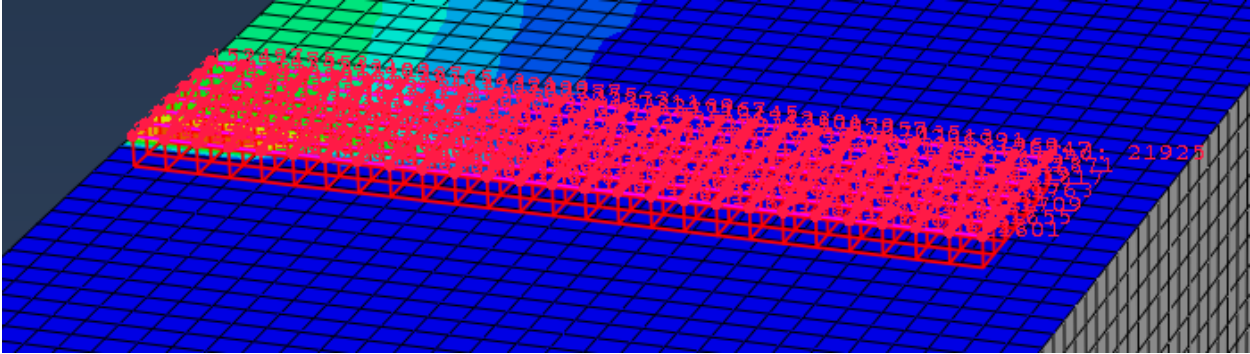
Fig. 5-10: Perspective of the path of collection on the soil, (a) with the mat, (b) without the mat

4.2.4. Coding in Python

These integrations represented a substantial amount of work to perform by hand; thus, the programming language Python was used to automate the calculations. Fig. 5-11 to Fig. 5-13 show the code used to integrate the shear stresses, bending stresses and contact pressures. These codes output a list of the values of shear force, bending moment and contact pressure along the mat's length, which were transferred to Microsoft Excel for the data treatment.

Finally, Fig. 5-14 illustrates the path used to determine the deflection and differential settlement beneath the track.

```
5    thickness=[]
6    width=[]
7    storage_thickness=[]
8    storage_width=[]
9    step_thickness=0.0508003    # distance between two nodes within the mat's thickness
10   step_width=0.0554180        # distance between two nodes within the mat's width
11
12   for j in range(len(pos)-1):     # pos is a list comprised of the distances
13                                   # seperating two nodes following each other
14       if (pos[j+1]-pos[j])<0.3:  # from one node to the next within the mat's thickness
15           storage_thickness.append((shear[j+1]+shear[j])/2*step_thickness)
16           # 'shear' is a list containing the values of shear stress at the nodes extracted
17           # from Abaqus. The results of the integration between two points are stored in the list
18           # 'storage_thickness', for each point within the mat's thickness in consideration
19           if j==9014:    # these 5 lines of code are meant to treat last element of path
20               thickness.append(sum(storage_thickness))
21               for i in range(len(thickness)-1):
22                   storage_width.append((thickness[i+1]+thickness[i])/2*step_width)
23               width.append(sum(storage_width))
24       elif (pos[j+1]-pos[j])<1 and (pos[j+1]-pos[j])>0.3:   # when all the nodes within a
25                                                            # thickness of the mat have ben browsed
26           thickness.append(sum(storage_thickness))         # in the list 'thickness' is appended
27                                                            # the elements of 'storage_thickness'
28           storage_thickness=[]
29       else:                                       # when all the nodes of a plane have been browsed
30           for i in range(len(thickness)-1):
31               storage_width.append((thickness[i+1]+thickness[i])/2*step_width)
32               # the results of the integration between two elements of the list
33               # 'thickness' are stored in the list 'storage_width'
34           width.append(sum(storage_width))    # then in the list 'width' is appended all the
35                                               # elements of the storage list 'storage_width'
36           storage_width=[]
37           thickness=[]
```

Fig. 5-11: Python code used to integrate the shear stress points collected in the mat

```
 7    levarm1=-0.0508003          # moment arm for the nodes around the neutral axis
 8    levarm2=-0.0508003*2
 9    levarm3=-0.0508003*3
10    N=7                         # number of nodes along the mat's thickness
11
12    S11_momented=[]             # this list is to store the collected values of normal stress,
13                                # multiplied by the adequate moment arm
14    for i in range(0,1288):    # 1288 = 9016 / N, 9016 being the number of nodes in the mat
15        j=N*i
16        # the mat's thickness contains 7 nodes. Therefore, the 4th node from either brim (or
17        # in the 'middle') is located on the neutral axis. The 6 nodes placed at either side
18        # of it thus need to be multiplied by the distance with that node. These distances are
19        # defined by levarm1, levarm2 and levarm3
20        S11_momented.append(S11[j]*levarm3)    # 'S11' is the list that contains the normal stress
21        S11_momented.append(S11[j+1]*levarm2) # values extracted from Abaqus
22        S11_momented.append(S11[j+2]*levarm1)
23        S11_momented.append(0)
24        S11_momented.append(-S11[j+4]*levarm1)
25        S11_momented.append(-S11[j+5]*levarm2)
26        S11_momented.append(-S11[j+6]*levarm3)
27
28    thickness=[]
29    width=[]
30    storage_thickness=[]
31    storage_width=[]
32    step_width=0.0554180
33    step_thickness=0.0508003
34
35    # what follows is identical to the shear stress code
36    for j in range(len(pos)-1):
37        if (pos[j+1]-pos[j])<0.3:
38            storage_thickness.append((S11_momented[j+1]+S11_momented[j])/2*step_thickness)
39            if j==9014:
40                thickness.append(sum(storage_thickness))
41                for i in range(len(thickness)-1):
42                    storage_width.append((thickness[i+1]+thickness[i])/2*step_width)
43                width.append(sum(storage_width))
44        elif (pos[j+1]-pos[j])>0.3 and (pos[j+1]-pos[j])<1:
45            thickness.append(sum(storage_thickness))
46            storage_thickness=[]
47        else:
48            for i in range(len(thickness)-1):
49                storage_width.append((thickness[i+1]+thickness[i])/2*step_width)
50            width.append(sum(storage_width))
51            storage_width=[]
52            thickness=[]
```

Fig. 5-12: Python code used to integrate the bending stress points collected in the mat

```
 6    length=[]
 7    width=[]
 8    storage_length=[]
 9    storage_width=[]
10    step_z=0.206522              # distance between two nodes along the mat's width
11    step_x=0.206667              # distance between two nodes along the mat's length
12    mat_width=step_z*6
13
14    for j in range(len(pos)-1):
15        if (pos[j+1]-pos[j])<1:  # from one node to the next along the mat's width
16            storage_length.append((cpress[j+1]+cpress[j])/2*step_z)
17            # the results of the integration between two points
18            # are stored in the list 'storage_length'
19
20        else:    # when one row along the mat's width has been browsed
21            length.append(sum(storage_length))
22            # the results of the integration between two points comprised in the
23            # list 'storage_length' are stored in the list 'length', which will
24            # contain all the values of contact pressure along the mat's length
25            storage_length=[]
26
```

Fig. 5-13: Python code used to integrate the values of contact pressure collected on the soil
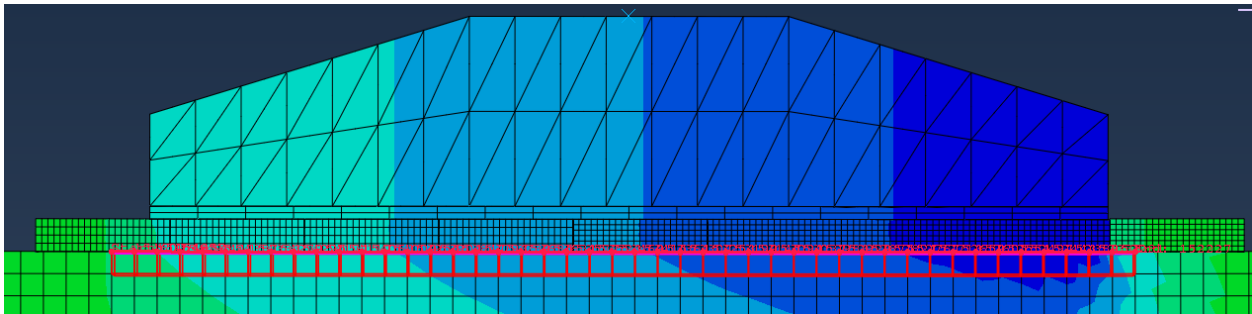
Fig. 5-14: Side view of the beam-crawler and layer of mat. In red is displayed the path from which will be collected the values of vertical displacement

The value of vertical displacement collected on the far left end of the path is defined as the deflection, and the value of vertical displacement collected on the far right of it, when subtracted by the first value, is the differential settlement. As the position of maximum vertical displacement may vary with the soil type and the load case, the value of displacement on the right will always be taken so that the worst case scenario is considered.

4.3.   Results

Exactly five physical quantities were extracted from the results in Abaqus, for every load case of every soil type of every solution used by PCL to attempt to reduce the soil bearing pressure:

the maximum shear stress in the mat, the maximum bending stress in the mat, the total load beneath the mat, the soil's deflection and the differential settlement. Each sub-part of the present part *4.3.*

Results corresponds to one solution, wherein will be displayed the values mentioned above and their comparison to the values obtained for the first solution proposed by PCL, which is to use one layer of mat.

4.3.1. Model with one layer of mat

Placing one layer of mat between the track and the soil is the most commonly used solution. Fig. 5-15 shows the contact pressure on the compact sand type of soil beneath the mat, and the shear force and bending moment in the mat along its length, perpendicular to the track's length, when the crane is loaded to 90% of its capacity.

(a)
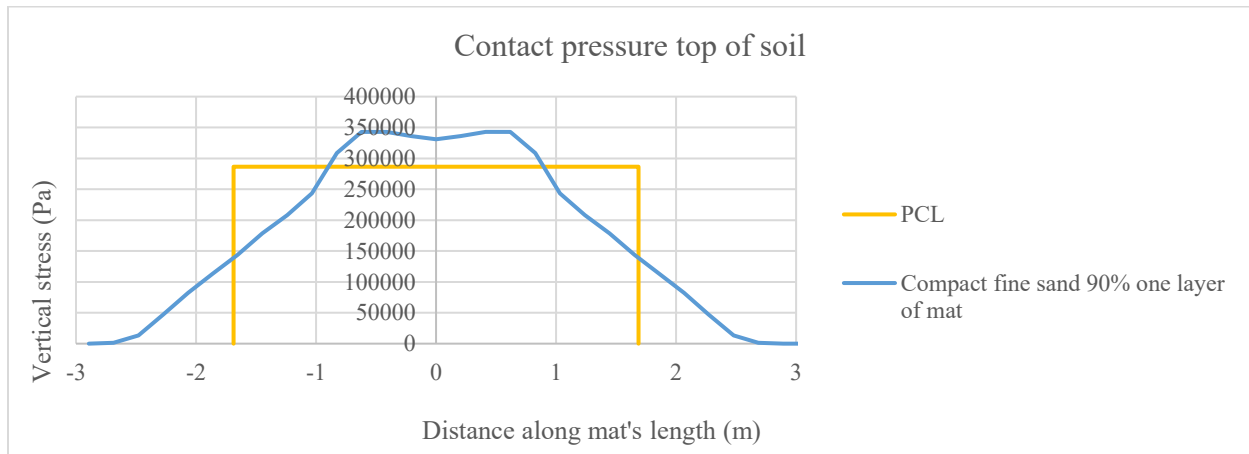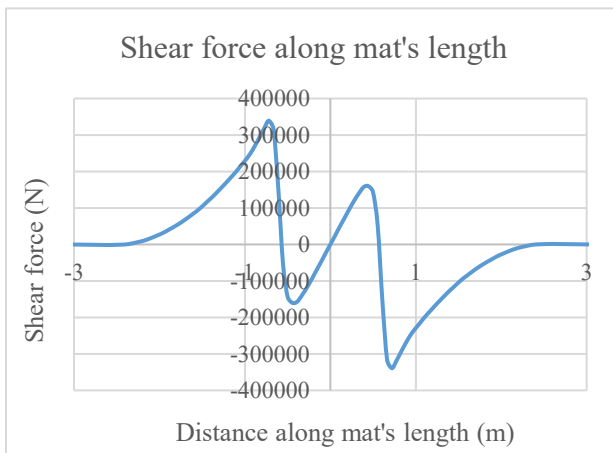
(b)   (c)
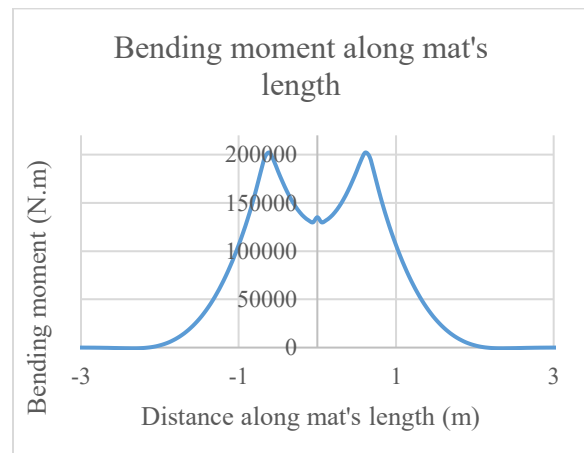
Fig. 5-15: For the soil made of compact fine sand: (a) contact pressure beneath the mat, (b) shear and (c) bending moment diagram in the mat

83

The three plots' X-axis range from -3m to 3m, which matches the mat's actual length (6.096m) and thereby eases the visualization.

The contact pressure plot also displays the stress distribution predicted by the method currently used by PCL, in yellow. The former will always show the same relative position with respect to the curve associated to the finite element analysis. The biggest pressure predicted by Abaqus is higher than that assumed by PCL, within a span of about 1.6m that goes beyond the 1.34m of the track's width. In this area, the FEA curve exhibits a grove that reaches a minimum in the middle of the graph. The modeling of the crawler as a rigid body explains that, as the crawler loses contact with the mat around its longitudinal axis as the mat bends under the loads. FEA also predicts that the stress distribution decreases after these 1.6m and that the curve's span is longer than that of the yellow curve, meaning that according to the FEA, the soil's length carrying the loads is higher, thereby increasing the effective mat's length.

The shear diagram shows that the track's edges act as simple supports to the mat. Fig. 5-16 is shown as a recall of the shear and bending moment diagrams for a beam overhanging one support with a uniformly distributed load, for the analogy.

The maximum shear values are found beneath the track's edge. In accordance with clause 6.5.5.1.1 of the Canadian Foundation Engineering Manual, the maximum shear can be taken at a distance equal to the mat's depth. For instance, in Fig. 5-15-b, the peak in shear is located at 0.72m from the y-axis, therefore the max in shear can be taken at a distance of 0.72+0.3048 = 1.0248m from the y-axis, which lowers the maximum value from 340000 N to 230000 N. The maximum shear stress is then calculated in accordance with the equation that follows:

$$\tau_{max} = \frac{V_{max}Q}{Ib}$$

with Q the mat's cross-section's first moment of area, I the mat's cross-section's second moment of area, b the mat's width and V_{max} the value discussed above. Except for V_{max}, these parameters will keep a constant value all along this study, displayed in As per the contact pressure's curve, on the bending moment diagram is seen a grove beneath the track which indicates the loss of contact between the track and the mat, because of the crawler's rigid property. Again, the maximum values of bending are found beneath the track's edges, from which is calculated the maximum bending stress in the mat, according to the equation that follows:

$$\sigma_{max} = \frac{M_{max}t}{2I}$$

with t the mat's thickness, M_{max} the maximum value of bending moment along the mat, and I defined earlier. The soil bearing pressure is calculated according to the equation that follows:

$$\sigma_{soil} = \frac{Total\ load\ beneath\ mat}{bc}$$

with c taken as the mat's bearing length.

Table 5-3: Geometric quantities associated to a mat

mat's width b (m)	mat's thickness t (m)	A (m^2)	Q (m^3)	I (m^4)
1.2192	0.3048	0.371612	0.0141584	0.002877
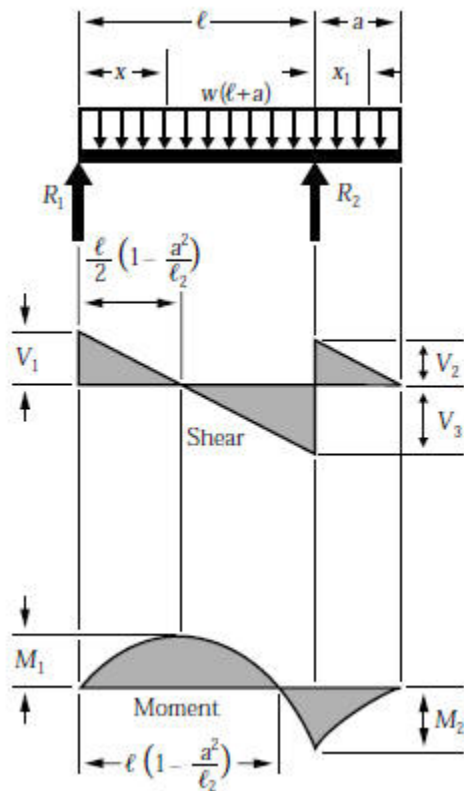
Fig. 5-16: shear and bending moment diagrams for a beam overhanging one support with a uniformly distributed load

As per the contact pressure's curve, on the bending moment diagram is seen a grove beneath the track which indicates the loss of contact between the track and the mat, because of the crawler's rigid property. Again, the maximum values of bending are found beneath the track's edges, from which is calculated the maximum bending stress in the mat, according to the equation that follows:

$$\sigma_{max} = \frac{M_{max}t}{2I}$$

with t the mat's thickness, M_{max} the maximum value of bending moment along the mat, and I defined earlier. The soil bearing pressure is calculated according to the equation that follows:

$$\sigma_{soil} = \frac{Total\ load\ beneath\ mat}{bc}$$

with c taken as the mat's bearing length.

The same curves are plotted for every load case, as shown in Fig. 5-17. A significant observation needs to be made. Conversely to what was thought and expected, the bearing length of the mat does not vary with the intensity of the load. This is very important, for the soil bearing pressure is inversely proportional to the bearing length. Therefore, for a given soil, the only parameter that can be played with in the expression of the soil bearing pressure is the total load, thereby the pressure applied on the track. In this study, an effective length was defined as the distance over which a quantity is less than one percent of the maximum it reaches over the total length of the mat. The effective length of mat activated by shear and bending are different from the effective length activated by contact pressure from the soil. In general, the soil bearing pressure will be the governing parameter in the design (as opposed to shear or bending); therefore, in general, the effective bearing length of the mat, that is the effective length activated by reaction from the soil, will be the retained value for the calculation of the soil bearing pressure. If the bending or shear were to govern, the associated effective mat's length would be chosen.

(a)

Contact pressure top of soil

(b)

86

Shear force along mat's length

(c)

Bending moment along mat's length
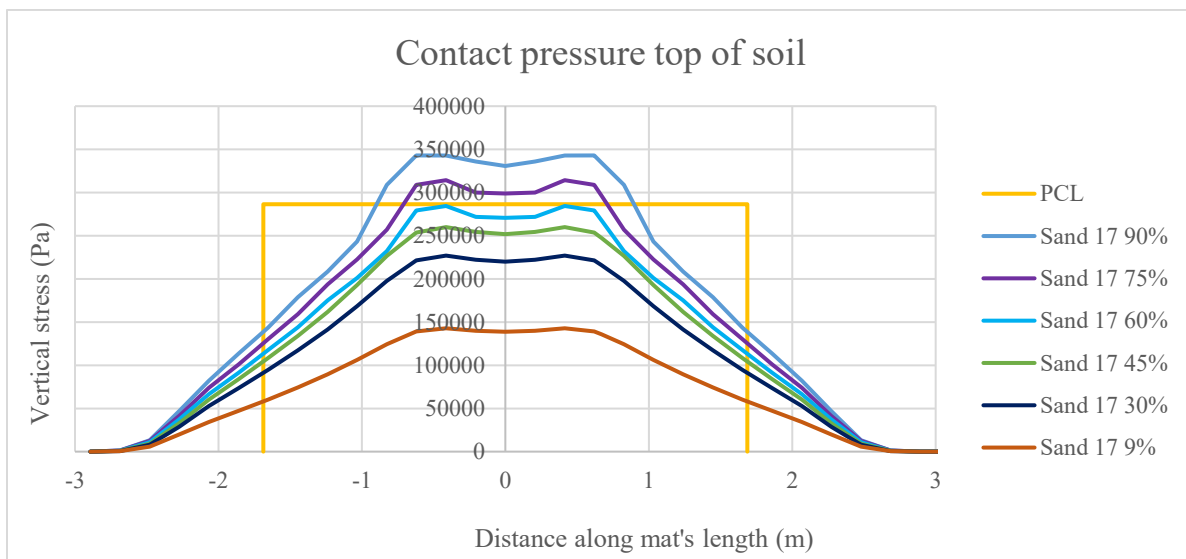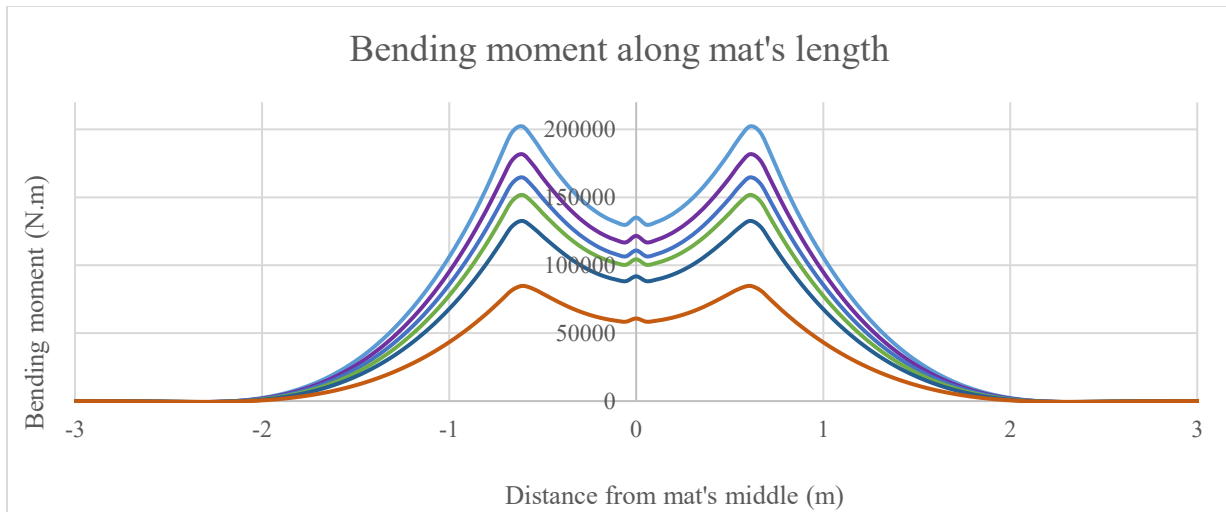
Fig. 5-17: For the soil made of compact fine sand: (a) contact pressure on the soil, (b) shear force and (c) bending moment diagrams, for all load cases

Table 5-4 summarizes all the quantities sought for in the simulations, for the five soils tested and the six load cases. From Table 5-4 are plotted thirty curves, one for each of the five physical quantities collected in Abaqus, as a function of the crane loading, for each of the five soils. On those curves were fitted polynomials such that the value of any of the six physical quantities could be found by interpolation, if the load were known. It is observed that the maximum shear stress, maximum bending stress and the resultant under the mat, are linear functions of the

87

Table 5-4: Values of the physical quantities collected in Abaqus, for all load cases and soil types, 1 mat

		Max bending stress (psf)	Max shear stress (psf)	Resultant under the mat (N)	Deflection (in)	Differential settlement (in)
Compact fine sand	0.9	223706	18800	647249	1.30	0.28
	0.75	201051	17283	580103	1.18	0.40
	0.6	182171	15765	524479	1.13	0.31
	0.45	167897	14248	487823	1.10	0.32
	0.3	146707	12730	426287	1.13	0.31
	0.09	93787	10606	269863	1.10	0.06
Surmont clay	0.9	216173	18378	647135	0.30	0.39
	0.75	195798	16945	581277	0.31	0.32
	0.6	181290	15512	544516	0.28	0.34
	0.45	161300	14079	484499	0.27	0.29
	0.3	140631	12646	423422	0.26	0.25
	0.09	88917	10640	267662	0.31	0.04
Loose gravel	0.9	194661	18800	656520	0.87	0.33
	0.75	177181	17093	603139	0.87	0.09
	0.6	160416	15386	545432	0.83	0.28
	0.45	142829	13678	485442	0.81	0.24
	0.3	124916	11971	424176	0.79	0.20
	0.09	79763	9581	267861	0.81	0.04
Very stiff clay	0.9	168798	15596	676090	0.63	0.28
	0.75	150135	14353	599969	0.62	0.24
	0.6	135926	13109	542788	0.63	0.28
	0.45	121145	11866	483019	0.60	0.17
	0.3	106050	10622	421964	0.57	0.16
	0.09	67514	8881	265766	0.59	0.02
Compact gravel	0.9	152720	15933	673965	0.56	0.24
	0.75	135822	14395	598134	0.56	0.20
	0.6	123039	12856	541119	0.55	0.17
	0.45	109688	11318	481447	0.53	0.16
	0.3	96004	9779	420565	0.52	0.13
	0.09	60966	7625	264507	0.53	0.03

loading. That realization was further expanded to all the configurations that were to be studied (two layers of mats, 6" layer of gravels…). It is not exactly true for the deflection and differential

settlement. The magnitudes of the former and later, however, are way under allowable values; as a matter of fact, they never come close to jeopardize the system. Therefore, to gain substantial amounts of time, only two load cases for each configuration and each soil, instead of six, and linear interpolation was used to determine the response of the system to any loads that was not tested.

As shown in Table 5-1, any loading of the crane can be associated to one value of P1 and P2, from which P' can be derived. As a recall, P is defined in Fig. 5-5; P' is the pressure applied on the beam, as opposed to under the track for P, located along the vertical of the later. Table 5-5 is a chart that shows the interpolated values of all the quantities of interest in this study when the crane is loaded at 80% of its capacity. The spreadsheet changes dynamically with the input values P'1 and P'2, the values derived from P1 and P2 provided by Liccon. The boxes turn green or red, depending upon whether their values are below or above the corresponding allowable design values, summarized in Table 5-6.

Table 5-5: Example of interpolated values of the physical quantities of interest, when the crane is loaded to 80% of its capacity

	Max bending stress (psf)	Max shear stress (psf)	Differential settlement (in)	Deflection (in)
One layer of mat				
Sand 17	217,312	18,296	0.28	1.29
Clay 22	209,899	17,902	0.38	0.30
Gravel 19	188,868	18,233	0.32	0.86
Clay 5	163,587	15,183	0.27	0.62
Gravel 20	148,010	15,422	0.23	0.56

	Total load beneath mat (N)	Max cantilever distance (bending) (ft)	Max cantilever distance (shear) (ft)	Max cantilever distance (soil) (ft)	Soil bearing pressure (psf)
One layer of mat					
Sand 17	628,898	6.73	7.81	8.66	5,284
Clay 22	628,555	6.36	7.12	8.10	5,581
Gravel 19	637,224	6.17	7.09	8.07	4,462
Clay 5	654,984	5.58	6.46	7.45	4,970
Gravel 20	652,920	5.28	6.23	7.32	5,043

(a)

Sand 17

● Max shear stress (psf)

⋯⋯⋯ Poly. (Max shear stress (psf))

$y = -5.96046E\text{-}08x^4 + 6.17504E\text{-}07x^3 - 4.61853E\text{-}07x^2 + 10116.66667x + 9695$
$R^2 = 1$

(b)

Sand 17

● Max bending stress (psf)

⋯⋯⋯ Poly. (Max bending stress (psf))

$y = -1753714.22x^5 + 4245038.634x^4 - 3413452.873x^3 + 888130.4336x^2 + 190488.5543x + 71669.03671$
$R^2 = 0.999999996$

(c)

Sand 17

● Resultant under the mat (N)

⋯⋯⋯ Poly. (Resultant under the mat (N))

$y = -7881229.542x^5 + 19421770.85x^4 - 16454380.83x^3 + 5206835.658x^2 + 120572.9161x + 227603.1783$
$R^2 = 0.999999999$

(d)

Sand 17

● Deflection (in)   ⋯⋯⋯ Poly. (Deflection (in))

$Y = 23.56668903x^5 - 62.27519426x^4 + 62.16355336x^3 - 28.12362812x^2 + 5.452084756x + 0.79810545$
$R^2 = 0.999999975$

(e)

Sand 17

● Differential settlement (in)

⋯⋯⋯ Poly. (Differential settlement (in))

$y = -41.19021077x^5 + 89.87114105x^4 - 67.43816443x^3 + 19.09586267x^2 - 0.755183008x + 0.011917294$
$R^2 = 1.000000001$

Fig. 5-18: For the soil made of compact fine sand, fitted polynomials for further interpolations for (a) maximum shear stress, (b) maximum bending stress, (c) resultant under mat, (d) deflection and (e) differential settlement

90

The allowable soil bearing capacities were calculated after Eq. (10.1) given in the Canadian Foundation Engineering Manual and reminded in the equation that follows:

$$q_u = cN_cS_c + q_sN_qS_q + \frac{1}{2}\gamma BN_\gamma S_\gamma$$

where:

q_u	= ultimate bearing capacity,
N_c, N_q, N_γ	= dimensionless bearing capacity factors,
S_c, S_q, S_γ	= dimensionless modification factors for foundation shape, inclination, depth and tilt and ground slope,
q_s	= vertical stress acting at the elevation of the base of foundation (taken as

zero in the study, since the mat is placed on the ground, at depth equal to zero),

B	= width of foundation or least plan dimension of the foundation,
c	= soil cohesion,
γ	= soil unit weight.

Table 5-6: Allowable design values used in this thesis

Allowable bending stress	196800	psf	Allowable soil bearing capacity	Sand 17	11048	psf
	9422	kPa			529	kPa
	177882	N.m		Clay 22	3091	psf
					148	kPa
Allowable shear stress	21400	psf		Gravel 19	4260	psf
	1025	kPa			204	kPa
	253844	N		Clay 5	9189	psf
					440	kPa
Allowable differential settlement	1.71	in		Gravel 20	12155	psf
	44	mm			582	kPa

The ultimate bearing capacities were calculated with data provided by PCL and the provisions given in Chapter 10 of the CFEM. In the case where two layers of mats were used, the width of the strip footing named B, was doubled in the equation of the ultimate bearing capacity.

It was taken as 8 ft instead of 4 ft. This is because of two reasons: the differential settlement between the mat that is neighbouring the mat studied is extremely small, and the weight of the track above prevents any rotation of the neighbouring mat. Therefore, these two mats can be considered solidary of one another. Table X gives the allowable bearing capacities when the footing's width is doubled. The allowable bearing capacities were calculated with a factor of safety of 2.

Table 5-7: Allowable bearing capacities when the width of the strip footing is taken as twice the width of that of a single mat

Allowable soil bearing capacity - 2 mats		
Sand 17	11063	psf
	530	kPa
Clay 22	3015	psf
	144	kPa
Gravel 19	4852	psf
	232	kPa
Clay 5	9046	psf
	433	kPa
Gravel 20	18885	psf
	904	kPa
Aspen	684	psf
	33	kPa

4.3.2. Model with two layers of mats

When any of the physical quantities studied exceed the allowable values detailed in Table 5-6, a second layer of mats can be introduced between the first layer and the soil, as shown in Fig. 5-19.
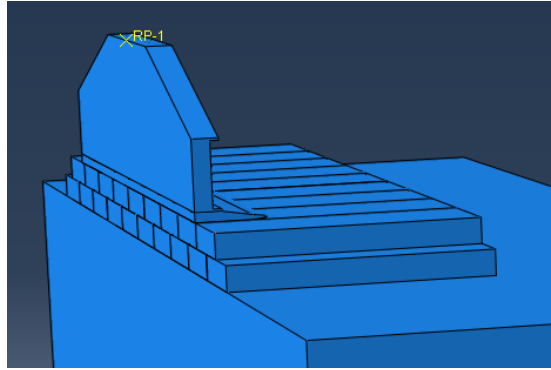
Fig. 5-19: Configuration showing two layers of mats beneath the track and the soil

The idea behind that solution is to increase the thickness of the medium between the track and soil, so that the area of soil affected by the loading expands, the stresses locally decrease and the mat's effective bearing length increases. The same paths than before were used. The shear and bending diagrams were plotted for both the mat right beneath the track's end and the mat directly placed underneath the later, as shown in Fig. 5-20. As mentioned earlier, the evolution of the maximum shear stress, maximum bending stress and total load under the mat are linear functions of the loading. It was also assumed, with less reliability, that the deflection and differential settlement also evolved linearly with the loading. Fig. 5-21 shows, for the two load cases tested, the curves of (a) the contact pressure on the soil at the same location as in the case of one layer of mat, (b) the shear and bending diagrams of the upper mat, and (c) the shear and bending diagrams of the lower mat, for the compact sand type of soil.
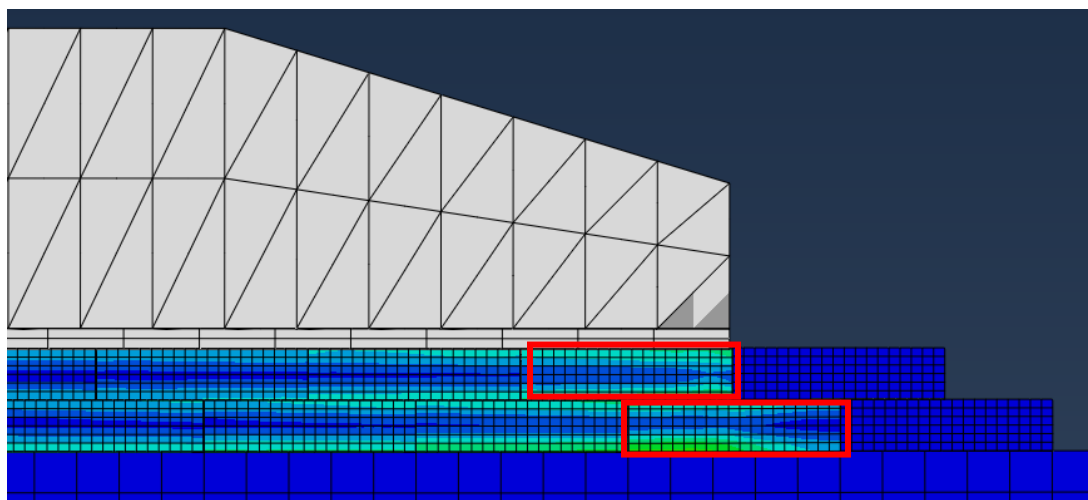
Fig. 5-20: Upper and lower mats analyzed

(a)

93

Contact pressure top of soil

(b)

Shear force along upper mat's length

94

(c)

Bending moment along upper mat's length

(d)

Shear force along bottom mat's length

Compact fine sand 90% Bottom mat   Compact fine sand 30% Bottom mat

Bending moment along bottom mat's length
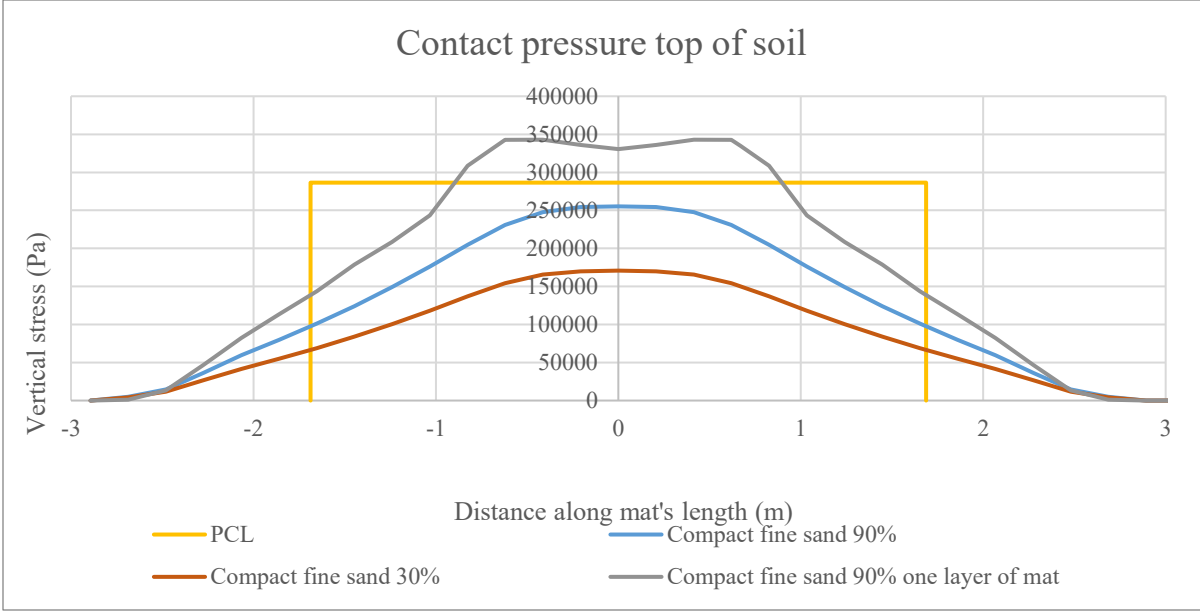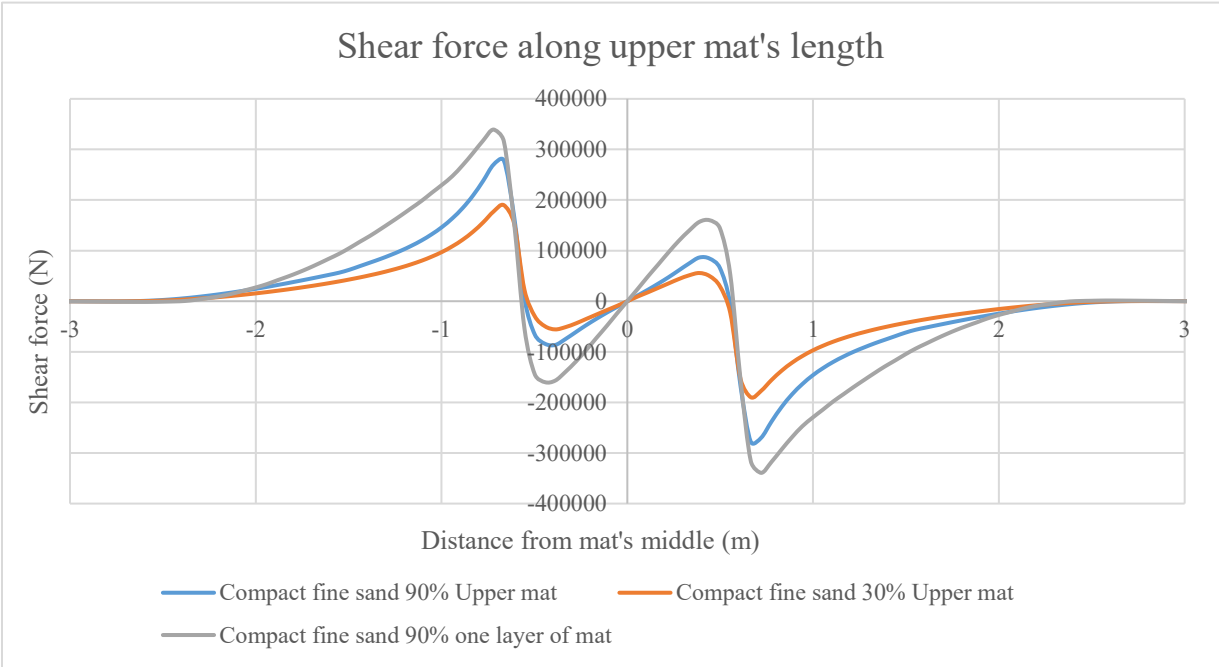
Fig. 5-21: For the soil made of compact fine sand, graphs of (a) contact pressure on the soil, (b) shear force and (c) bending diagrams in the upper mat, (d) shear force and (e) bending moment diagrams in the lower mat

Fig. 5-21-a allows to conclude that the prime objective in using a second layer of mat is successfully reached, the contact pressure curve is lower than that observed for one layer of mat; the maximum pressure dropped by almost 100 kPa, close to 30%. The values of maximum shear and bending stresses of the upper mat have also decreased; those of the lower mat are smaller than the upper mat's: the lower mat will always be safe if the upper mat's allowable shear and bending stresses are not reached. The deflection and differential settlement decrease too, but at different rates. Indeed, the change in loading is characterized by a variation of both P'1 and P'2 at the same time, with different rates of change. Therefore, even though it is undeniable that the deflection and differential settlement decrease at lower loads, they do it at different speeds.

Similarly to what was observed in the case of a single layer of mat, the effective bearing length and the effective lengths activated in shear and bending do not change with the intensity of the loading. In Fig. 5-21, although the values of effective lengths seem to be unchanged between the use of one or two layers of mat, given the definition of an effective length provided earlier, that is, the length over which a quantity is less than one percent of the maximum it reaches over the total length of the mat, the effective lengths will be greater when two layers of mat are used.

Table 5-8 displays the values of the five quantities collected in Abaqus for the two load cases tested.

Table 5-8: Values of the physical quantities collected in Abaqus, for all load cases and all soil types

		Max shear stress (psf)	Max bending stress (psf)	Resultant under the mat (N)	Deflection (in)	Differential settlement (in)
Compact fine sand	0.9	11802	150452	469360	1.07	0.38
	0.3	8768	101220	369337	1.01	0.24
Surmont clay	0.9	12814	145199	457944	0.20	0.38
	0.3	9358	108613	344593	0.20	0.26
Loose gravel	0.9	11718	130660	553786	0.79	0.30
	0.3	8009	87521	383946	0.74	0.19
Very stiff clay	0.9	11381	115183	469360	0.12	0.24
	0.3	7081	71747	377919	0.11	0.14
Compact gravel	0.9	11044	110690	449249	0.52	0.22
	0.3	6829	69372	377355	0.48	0.13

The same process of plotting curves and fitting equations to them was carried out. The results of the interpolations will not be presented for each of the six mat configurations individually anymore. Fig. 5-25 summarizes them at once.

4.3.3. Model with one layer of mat and 6" or 18" of compact gravel

In some cases, an alternative solution to the solution demanding two layers of mat is chosen. That solution consists of using a layer of compact gravel whose mechanical properties are given Table 5-2, of either 6 or 18 inches (15 or 45 cm). This solution is sometimes preferred as it presents an economical advantage compared to using two layers of mats. The idea, however, is similar: to increase the distance between the track and the soil to expand the area of the cone of propagationof loads.

Likewise, two simulations for each soil type were carried out, when the crane is loaded at 90% and 30% of its capacity. Fig. 5-22 shows, for the two load cases tested, the curves of (a) the contact pressure on the soil at the same location as in the case of one and two layers of mat, and (b) the shear and bending moment diagrams of the mat beneath the track's end.

(a)

97

Figure (b): Vertical stress top of soil - Compact fine sand / Shear force along mat's length - Compact fine sand
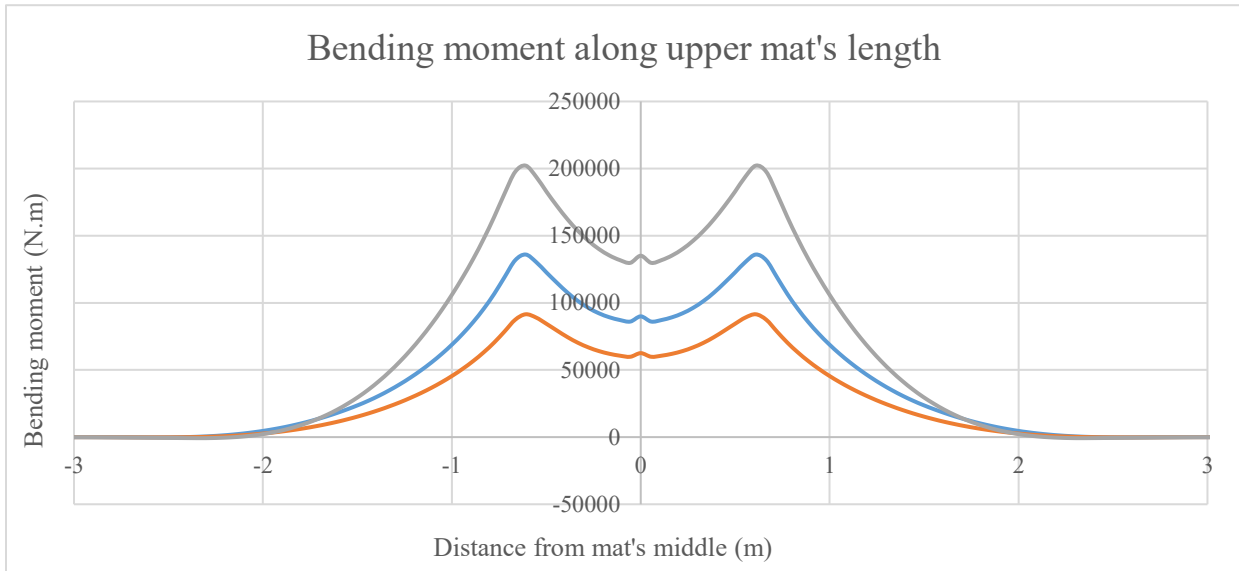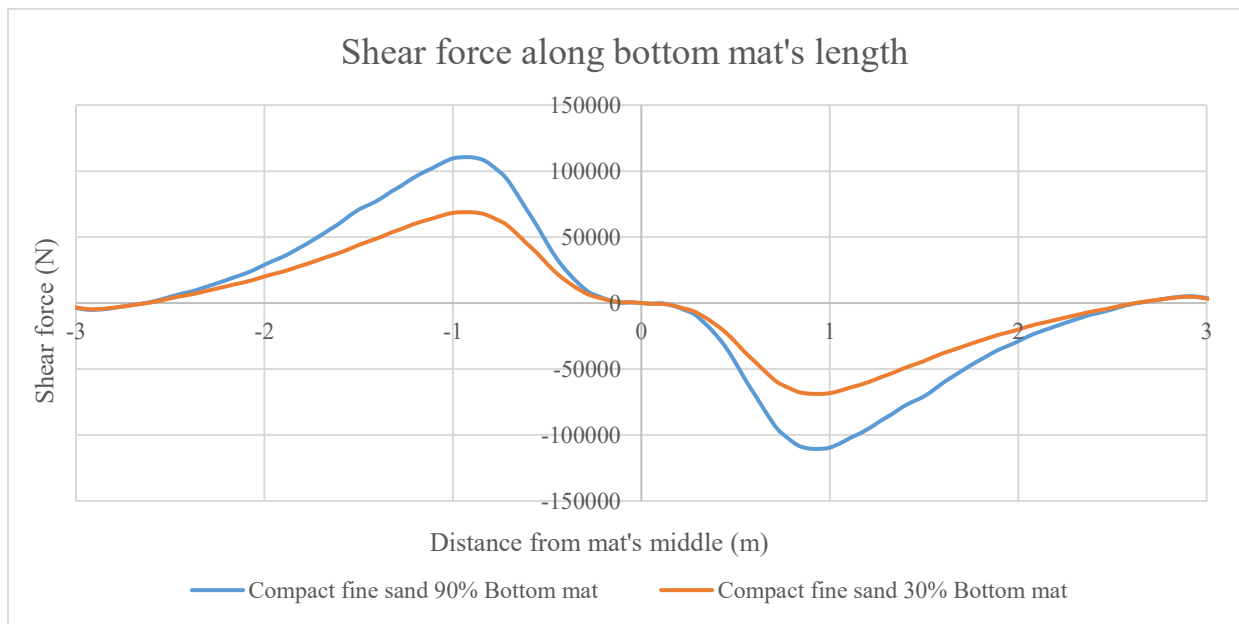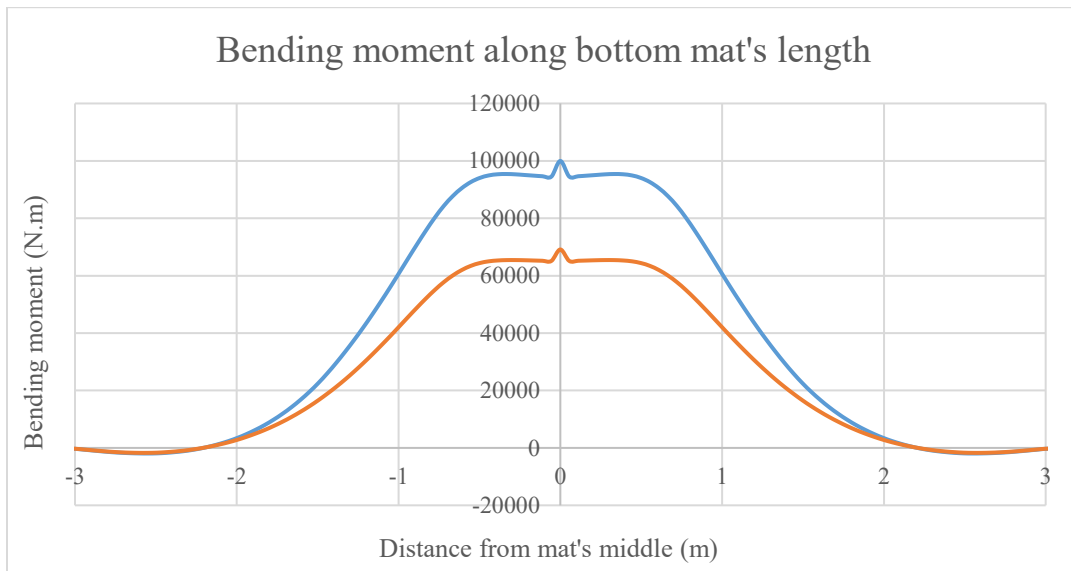
(b)

98
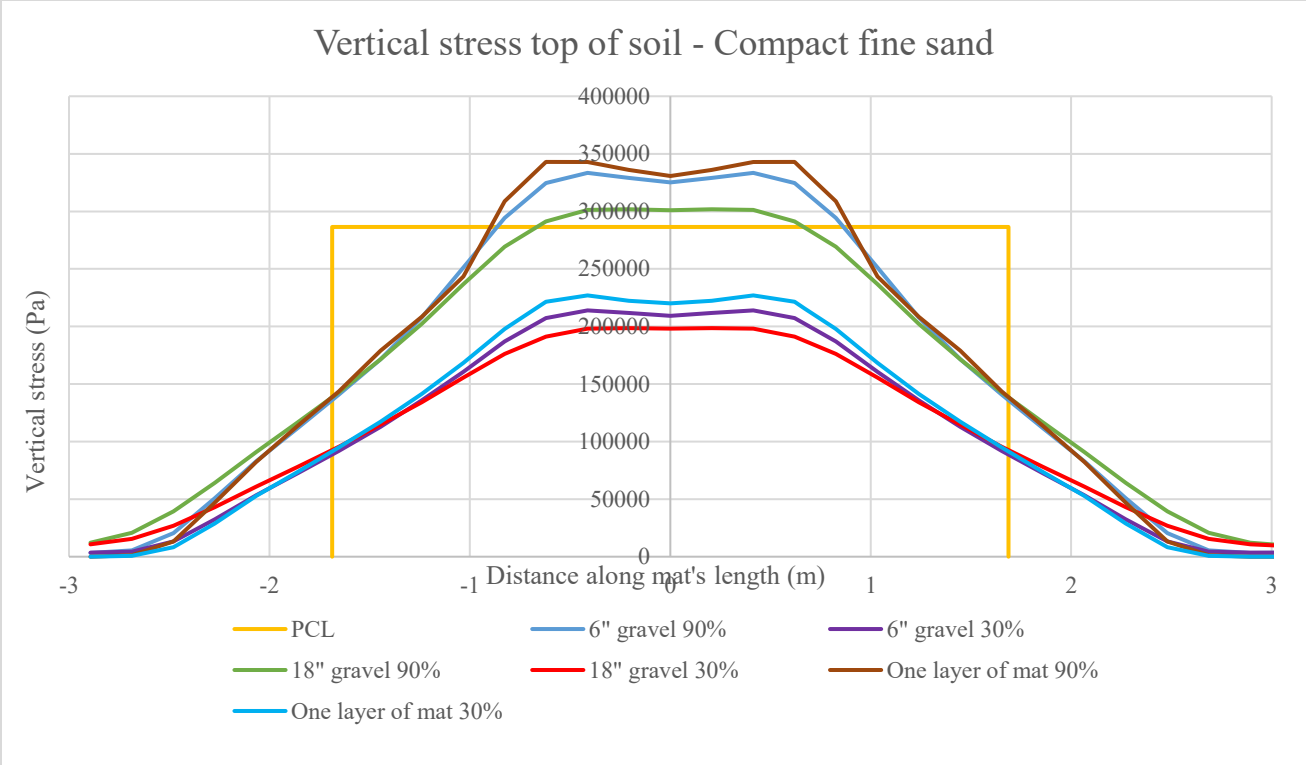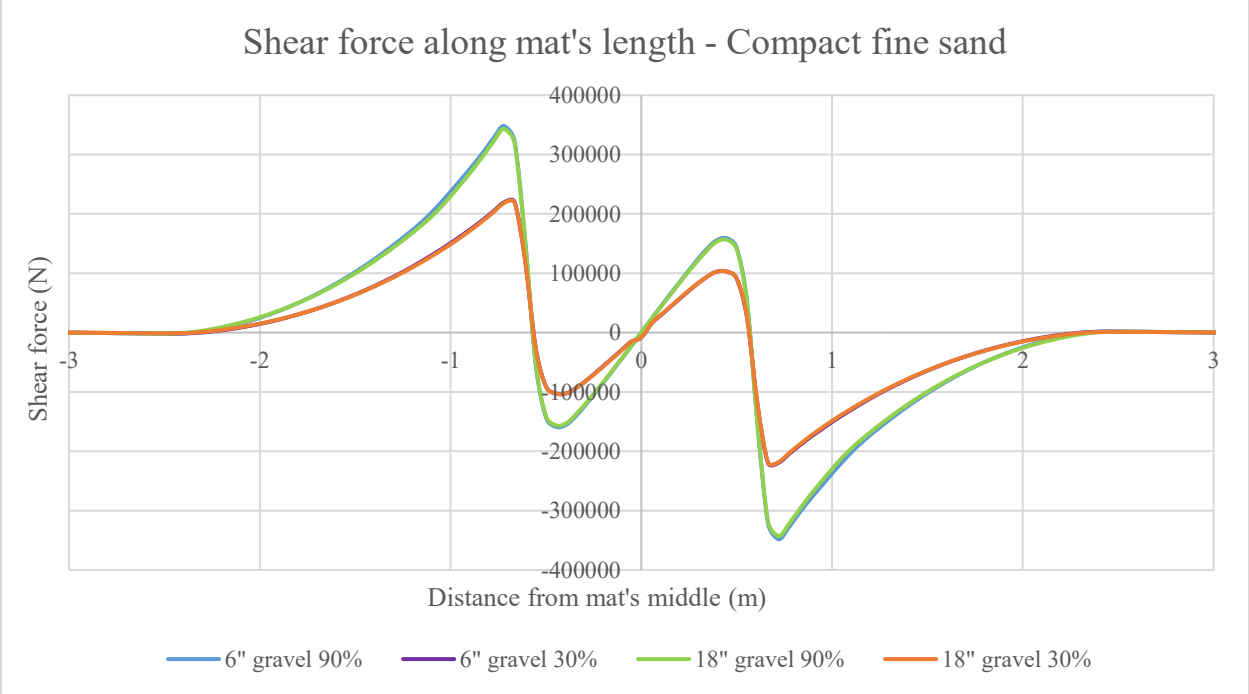
Fig. 5-22: For the soil made of compact fine sand: (a) contact pressure on the soil, (b) shear force and (c) bending moment diagrams, for the two load cases

Fig. 5-22-b and -c show that the shear and bending moment in the mat are independent of the gravel's layer's depth. Fig. 5-22-a shows that there is a decrease in the pressure that is undergone by the soil when a thicker layer is used, but that gain may not be substantial, compared with the amount of preparation that is needed on the field to set 18" of gravel instead of 6". What is likely to happen, is that although more gravel leads to a better redistribution of the loads to the soil, the addition of weigh balances out that positive effect. Consequently, interposing gravel between the mats and the soil might not be an interesting solution whatsoever; therefore, the use of gravels or of two layers of mat will have to be discussed against the economic costs of these solutions.

Fig. 5-25 displays the interpolated values of the five quantities sought for in this study, for the solutions 6" and 18" of gravel.

4.3.4. Model with two layers of mat and 6" or 18" of compact gravel

Another solution that is used to reduce the loads on the soil is a combination of two solutions that precede: to spread 6" or 18" of compact gravel under two layers of mats. Fig. 5-23

shows the curves of (a) the contact pressure on the soil at the same location as in the four preceding solutions, and (b) the shear and bending diagrams of the upper mat, beneath the track's end.

(a)

(b)

Bending moment along upper mat's length
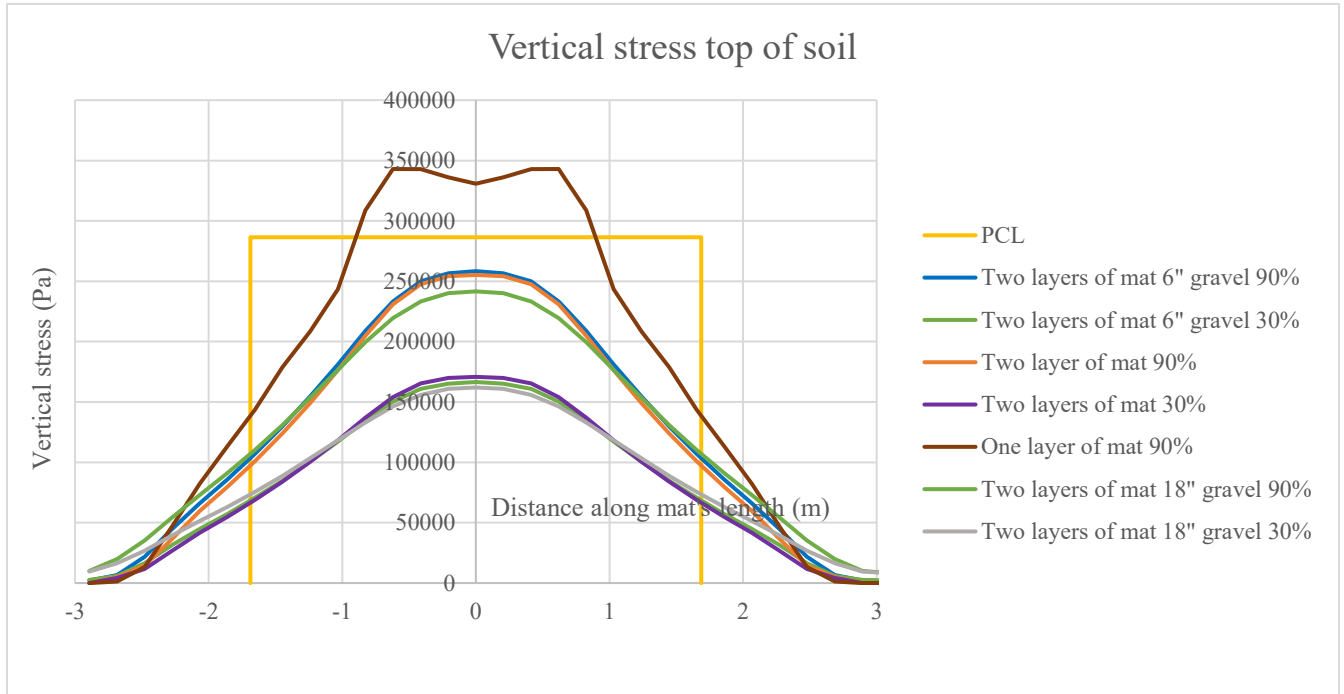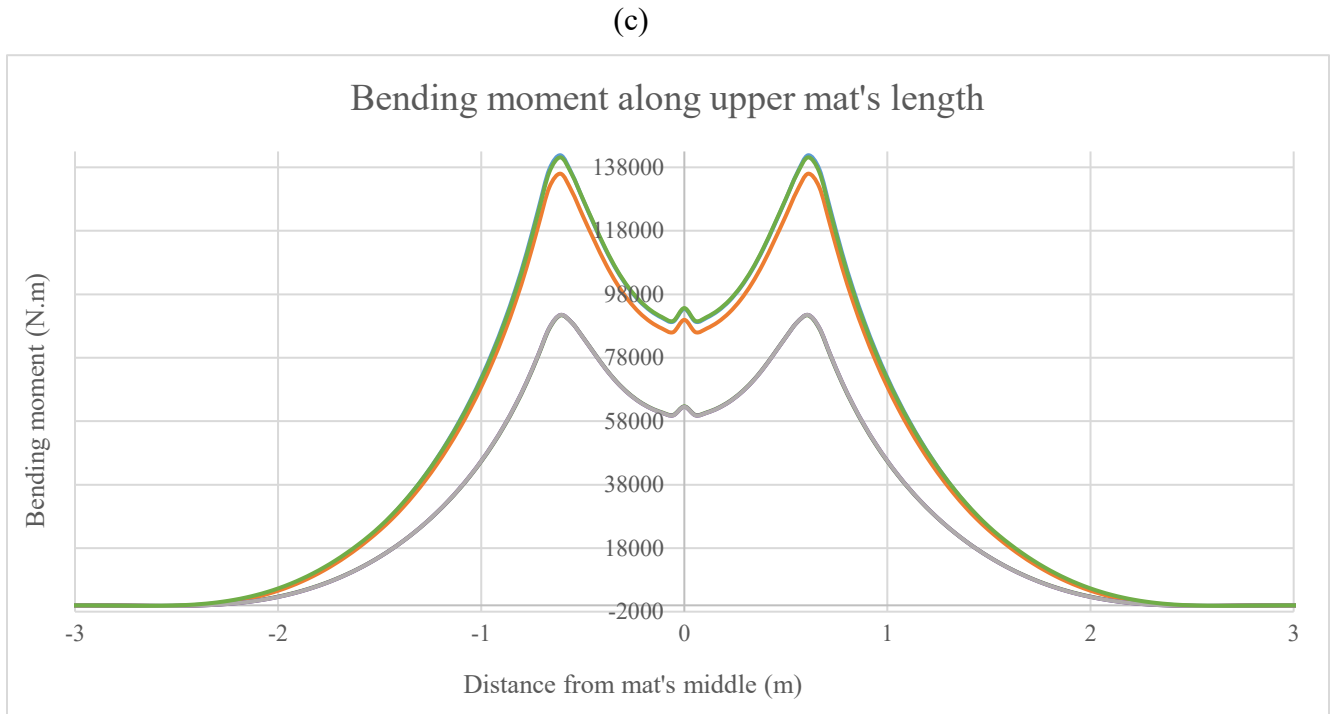
Fig. 5-23: For the soil made of compact fine sand: (a) contact pressure on the soil, (b) shear force and (c) bending moment diagrams, for all load cases

Fig. 5-23 shows there is very little improvement in using a 6" thick layer of gravels under two layers of mat, as was the case with one layer of mat. Using 18" of gravel, however, reduce the stresses on the soil, especially for high loads. Even though the bending and shear in the mat do not improve, this configuration could be used as a last resort if the soil bearing stresses were to be slightly above the allowable soil bearing capacity.

Fig. 5-25 displays the interpolated values of the five quantities sought for in this study, for the solution two layers of mats on top of 6" of compact gravel.

4.3.5. Model with three layers of mat

Finally, one last configuration was tested, only for the soil made of compact fine sand and loose gravel. It consists of interposing a third layer of mats, placed between and perpendicular to the two layers of mats discussed above. Fig. X shows the curves of (a) the contact pressure on the soil at the same location as in the case of one, two and three layers of mat, and (b) the shear and bending moment diagrams of the mat beneath the track's end.

Vertical stress top of soil

Shear force along upper mat's length
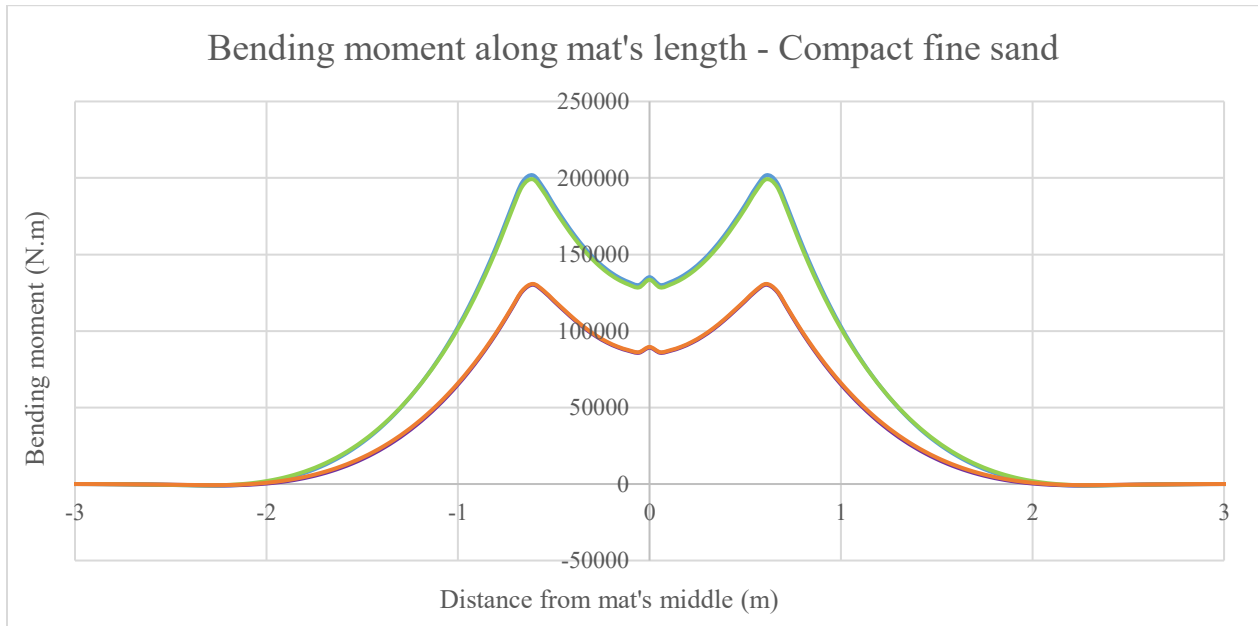
Bending moment along upper mat's length
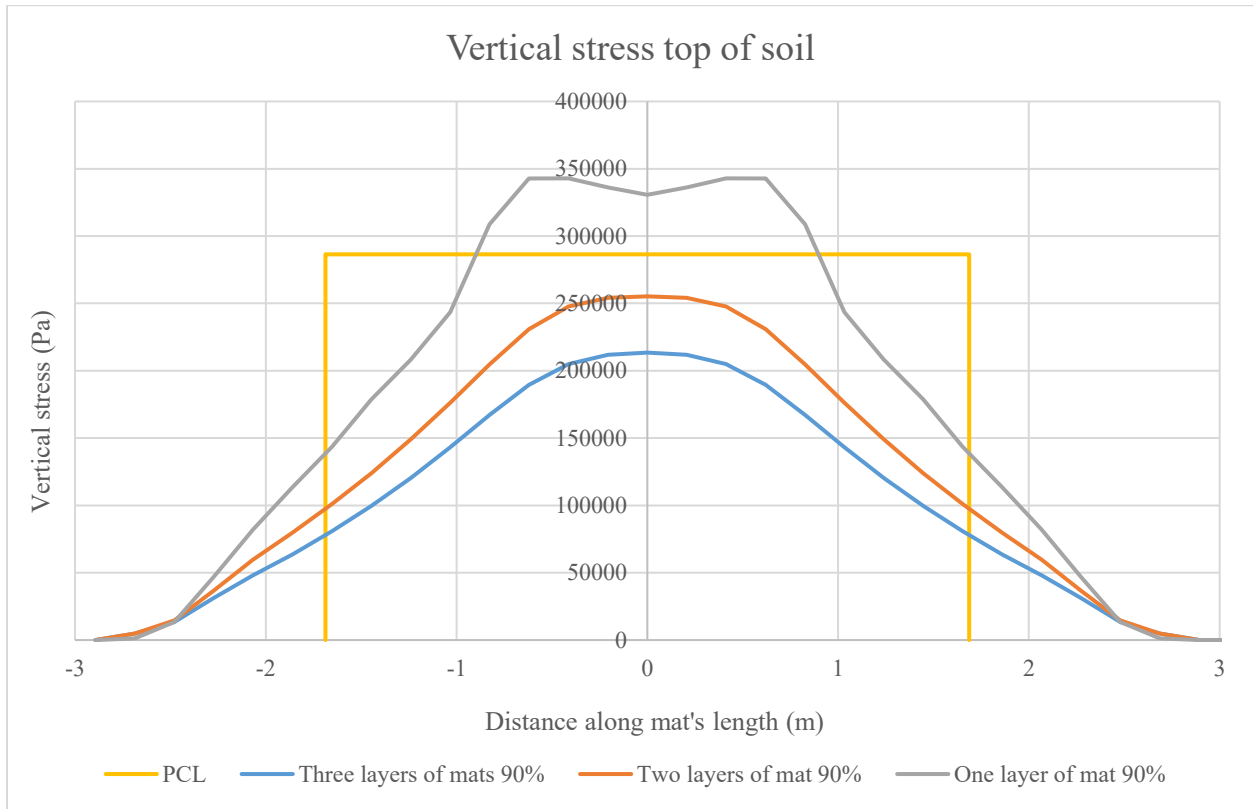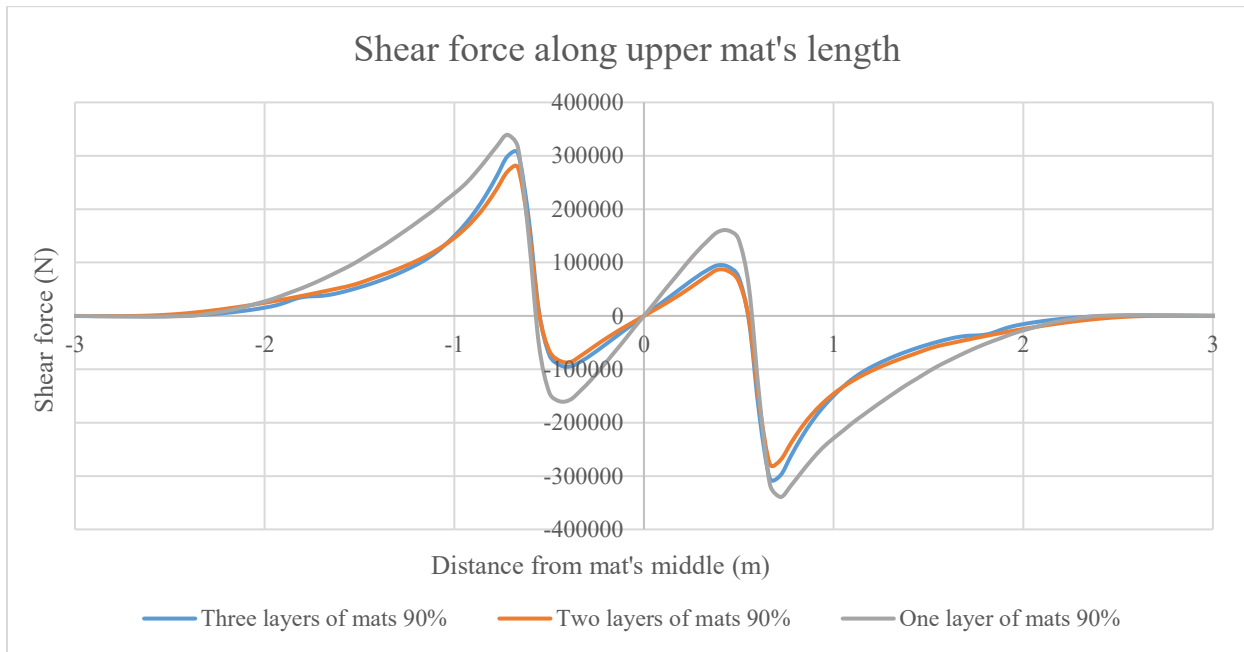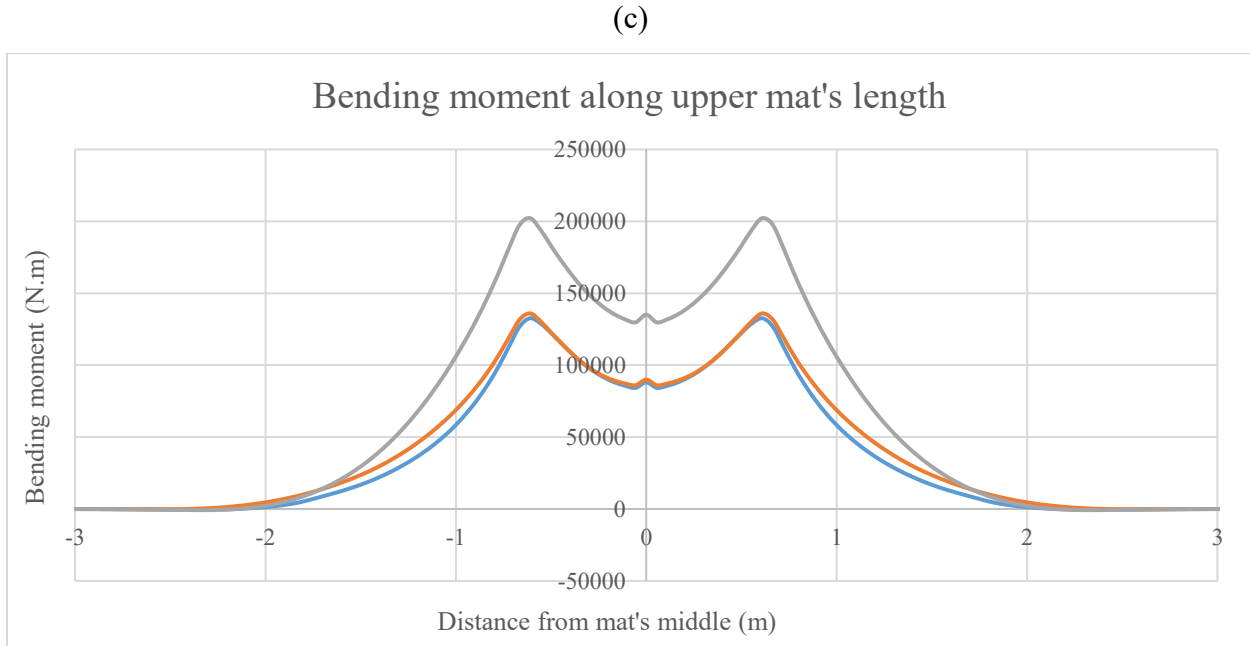
Fig. 5-24: For the soil made of compact fine sand: (a) contact pressure on the soil, (b) shear force and (c) bending moment diagrams, for all load cases

Fig. 5-23 shows that using three layers of mats primarily affects the soil bearing pressure, with a reduction of about 15% of the maximum pressure. The extra layer allows the stresses to travel further sideways and therefore reduce their intensity on the area directly at the vertical of the track's end. Setting up a third layer of mats implies substantial financial costs, though some soils, like that made of loose gravels, are so fragile that it can be a conceivable solution.

4.4. Summary of results and calculations spreadsheet

Part 4. of the present thesis was aimed to render the work during my internship at PCL, which originally had for objective to deliver a spreadsheet that would compute physical quantities of interest with more reliability than the methods that are currently used by the construction industry: the maximum shear and bending stresses in the mat that undergoes the highest pressure, the soil bearing pressure under that mat, the deflection of the field under the track and the differential settlement between the track's ends.

In part 4.3., the methods utilized by PCL to reduce the soil bearing pressure were presented and the effects they have on the quantities looked for, according to the model in Abaqus, were displayed. Fig. 5-25 is a screenshot of the final spreadsheet that will be used by PCL for the crane

model LR1600. Fig. 5-26 is a screenshot of the final spreadsheet that will be used by PCL for the crane model LR1400.

Input parameters:

Parameter	Value	Unit
Timber Mat Length	20	ft
Timber Mat Width (B)	4	ft
Timber Mat Depth (d)	1	ft
Timber Mat Weight (50lbs/ft³)	4000	lbs
Crawler Track Width (w)	4.4	ft
Crawler Track Weight	83776	lbs
Crawler track actual length	28.5	ft
P1 - Loading Under Crawler - Max	15,696	psf
P2 - Loading Under Crawler - Min	3,312	psf
Soil Loaded Length (L)	28.5	ft
P'1 - Loading on Beam - Max	31990	psf
P'2 - Loading on Beam - Min	5628	psf
P'3 - Loading at Low End of Critical Mat	28290	psf
P' - Equivalent Point Load	30140	psf
	1,443	kPa
P' ∈ [444;1422]		
P' ∈ [9%;90%]		
Allowable bending stress	196800	psf
	9423	kPa
	177882	N.m
Allowable shear stress	21400	psf
	1025	kPa
	253844	N
Allowable differential settlement	1.71	in
	44	mm

Allowable soil bearing capacity - 1 mat

Soil	Value	Unit
Sand 17	6057	psf
	290	kPa
Clay 22	3044	psf
	146	kPa
Gravel 19	2652	psf
	127	kPa
Clay 5	9127	psf
	437	kPa
Gravel 20	10338	psf
	495	kPa

Results:

	Max bending stress (psf)	Max shear stress (psf)	Differential settlement (in)	Deflection (in)	Total load beneath mat (N)	Effective length (bending) (ft)	Effective length (shear) (ft)	Effective length (soil) (ft)	Soil bearing pressure (psf)
Compact fine sand									
One layer of mats	223,853	18,811	0.28	1.30	647669	13.45	15.62	17.32	5442
Two layers of mats	150,546	11,808	0.38	1.07	536477	15.29	17.45	18.31	3312
Two layer of mats 6" gravel	156,983	13,751	0.37	1.12	568099	14.54	16.34	18.90	3398
Two layers of mats 18" gravel	156,253	14,257	0.34	1.15	568099	14.63	16.60	20.00	3210
6" gravel layer	223,361	19,399	0.48	1.11	640941	12.86	14.90	20.00	5633
18" gravel layer	220,460	18,557	0.30	0.11	627344	13.12	15.03	20.00	5403
Three layers of mats	146,855	14,509	0.37	1.13	568099	14.44	16.40	18.37	3495
Surmont clay									
One layer of mats	216,316	18,389	0.39	0.30	647560	12.73	14.24	16.21	5749
Two layers of mats	145,290	12,823	0.38	0.20	533834	14.11	15.94	17.13	3523
Two layer of mats 6" gravel	152,803	13,498	0.37	0.22	571760	14.17	16.01	18.70	3456
Two layers of mats 18" gravel	153,017	14,088	0.34	0.24	568315	14.44	16.01	20.00	3212
6" gravel layer	217,178	18,811	0.30	0.35	641860	12.40	14.24	17.52	5850
18" gravel layer	215,315	18,727	0.41	0.24	627598	12.73	14.54	20.00	5572
Loose gravel									
One layer of mats	194,793	18,813	0.33	0.87	656962	12.34	14.17	16.14	4600
Two layers of mats	130,742	11,725	0.30	0.79	532929	12.66	14.90	16.17	3725
Two layer of mats 6" gravel	137,316	11,134	0.30	0.82	576183	13.12	15.09	18.70	3482
Two layers of mats 18" gravel	138,813	13,160	0.27	0.84	572372	13.58	15.29	20.00	3235
6" gravel layer	196,093	19,235	0.37	0.81	654230	11.88	13.78	20.00	3697
18" gravel layer	197,952	19,066	0.33	0.84	640331	12.14	14.04	20.00	5962
Three layers of mats	128,688	13,412	0.24	0.83	516042	11.94	13.78	18.96	3076
Very stiff clay									
One layer of mats	168,918	15,606	0.28	0.63	676573	11.15	12.93	14.90	5134
Two layers of mats	115,266	11,389	0.24	0.12	548258	11.61	13.45	14.83	4179
Two layer of mats 6" gravel	116,637	11,489	0.23	0.13	584839	11.75	13.65	18.18	3637
Two layers of mats 18" gravel	119,923	11,641	0.21	0.13	577685	12.34	14.17	20.00	3265
6" gravel layer	163,993	16,366	0.27	0.13	648111	10.89	12.47	20.00	3663
18" gravel layer	170,875	15,268	0.25	0.13	634546	11.29	12.86	20.00	3586
Compact gravel									
One layer of mats	152,828	15,945	0.24	0.56	674447	10.56	12.47	14.63	5209
Two layers of mats	110,768	11,052	0.22	0.52	547347	11.29	13.12	14.83	4172
Two layer of mats 6" gravel	112,864	11,221	0.20	0.53	590215	11.42	13.39	17.91	3724
Two layers of mats 18" gravel	115,894	11,726	0.19	0.54	578999	12.01	13.85	20.00	3272
6" gravel layer	155,014	16,111	0.24	0.53	650747	10.70	12.47	15.62	4710
18" gravel layer	163,263	16,366	0.22	0.54	635694	11.09	12.86	20.00	3592

Fig. 5-25: Final spreadsheet, when the load is equal to 90% of the crane model LR1600's capacity

				Max bending stress (psf)	Max shear stress (psf)	Differential settlement (in)	Deflection (in)	Total load beneath mat (N)	Max cantilever distance (bending) (ft)	Max cantilever distance (shear) (ft)	Max cantilever distance (soil) (ft)	Soil bearing pressure (psf)
Timber Mat Length	20	ft	One layer of mat									
Timber Mat Width (B)	4	ft	Compact fine sand	154,671	19,681	0.49	0.84	407,680	6.00	7.09	8.10	2843
Timber Mat Depth (d)	1	ft	Surmont clay	148,017	19,191	0.44	0.09	408,447	5.84	6.79	7.94	2907
Timber Mat Weight (50lbs/ft³)	4000	lbs	Loose gravel	132,036	18,665	0.37	0.61	410,919	5.51	6.53	7.64	3038
Crawler Track Width (w)	3.4	ft	Stiff clay	131,221	18,400	0.36	0.03	407,680	5.45	6.33	7.40	3114
Crawler Track Weight	61078.5	lbs	Compact gravel	102,364	16,971	0.25	0.40	409,053	4.76	5.77	6.76	3420
Crawler track actual length	25.5	ft										
P1 – Loading Under Crawler – Max	17,280	psf										
P2 – Loading Under Crawler – Min	-	psf										
Soil Loaded Length (L)	14.7	ft										
P'1 – Loading on Beam – Max	27,266	psf										
P'2 – Loading on Beam – Min	(1,159)	psf										
P'3 – Loading at Low End of Critical Mat	19,531	psf										
P' – Equivalent Point Load	23,398	psf										
	1,120	kPa										

Fig. 5-26: Final spreadsheet, when the load is equal to 90% of the crane model LR1400's capacity

6. Summary, conclusion and further work suggestions

This thesis has investigated the distributions of stresses beneath crawler crane timber mats.

6.1. Peak stresses under objects' ends

The phenomenon of peak stresses was observed on stress distributions, leading to unexpected high stresses on the areas beneath solids' ends. In practice, however, peak stresses on the soil are likely to be dimmed by the system's defaults and the imperfection of mats' positioning.

6.2. Numerical simulations on ten crawlers and four soils: refutation of the rigid body assumption

This study has tried to challenge the assumption broadly made in the construction industry of uniformly distributed stresses in the soil. Ten distinct crawlers were tested on four different soils. It was figured that the assumption of uniform stresses was not true. Also, the crawler used by our industry collaborator led to stress distributions that were on average 10 to 20% higher than what would be observed with a rigid crawler, depending on the soil type.

6.3. Challenging beam theory: prevalence of flanges over the web

It was also found that the beam theory's hypothesis whereby stress distributions' uniformity is a function of the sole beam's stiffness, was true with a relative error of less than 10%, when beams' dimensions were realistic. It was also shown that flanges' thickness was a predominant parameter over the web's in the efficiency to redistribute loads. This study, however, does not allow to conclude which of the stiffness or flanges prevails over the other, for beams with extreme dimensions.

6.4. Comparison of numerical solutions with analytical distributions

Stress distributions obtained with Abaqus were then compared with analytical uniform stress distributions. It was determined that considering the mat as rigid or flexible both led to unrealistic stress distributions on the soil; but the reasonable assumption that stresses make their way through the mat with an angle of 45° conducted to a conservative uniform stress distribution that matched the numerical stress distributions, and by means of consequence, credited them.

Numerical stress distribution between the mat and the crawler were observed also to be much smaller than that derived analytical by assuming a rigid crawler. It was concluded that the mat was not likely to threaten the system's integrity.

6.5. Timber mats design methodology: development of a spreadsheet to be used in the construction industry

My work as an intern at PCL has given birth to equations that predict the values of five important quantities as a function of the crane's loading, for five types of soil - two cohesive and three granular -, six mats configurations - one layer of mats, two layers of mats, one layer of mats and a layer of compact gravel of a thickness of 6" or 18", and two layers of mats and a layer of compact gravel of a thickness of 6" or 18" as well - and 2 cranes - LR1600 and LR1400 -: the maximum shear stress, the maximum bending stress, the soil bearing pressure, the soil's deflection and the differential settlement. These equations were written in a spreadsheet that will be used by PCL in their future projects.

Further work would be required to refine the results. In particular, a better characterization of the influence of the soil's elasto-plastic parameters needs to be derived, so do the I-beam's stiffness, and flanges' and web's thickness in the redistribution of loads.

References

Abramov et al. (1968). *Stress distribution in soils under static loading.*

Boeing 747. (2018, January 22). In *Wikipedia: The free encyclopedia*. Retrieved from
https://en.wikipedia.org/wiki/Boeing_747/

Bestech. (2018, March). *Young Modulus for some Common Materials,* Retrieved from
http://www.bestech.com.au/modulus-of-elasticity/

Canadian Foundation Engineering Manual (2006)

Corey and Han. (2011). *Numerical Analysis of Soil Stress Distribution Under Restrained and
Eccentrically Loaded Footings Considering Soil Strength*

Cui and Zhou. (2009). *A new processing method for modelling the vertical stress distribution at
the soil surface.*

Duerr, D. Effective bearing length of crane mats. *Crane & Rigging Conference at Houston,
Texas, 7.*

Duong and al. (2018). *Investigating the stress distribution underneath a crane mat in one plane
of loading*

Forest Products Laboratory. (2010). *Wood handbook: Wood as an engineering material*
(Centennial ed.) United States Department of Agriculture Forest Service.

J.V. Perumpral et al. (1971). *A numerical method for predicting the stress distribution and soil
deformation under a tractor wheel.*

K. Hammel. (1994). *Soil stress distribution under lugged tires.*

Liu, X. (2005). *Soil bearing capacity for crawler cranes*

Lin et al. (2017). *An investigation of the distribution of mobile crane loads for construction
projects*

Shapiro, H. I., Shapiro, J. P., & Shapiro, L. K. (1999). *Cranes and Derricks*, 3rd ed., McGraw-
Hill, New York

W-equipment. (2018, March). *Liebherr LR 1750,* Retrieved from https://www.w-equipment.com/ads/cranes-hoists-and-winches/cranes/crawler-cranes/liebherr-lr-1750-363427.html